

WIND TUNNEL SIMULATION OF THE
ATMOSPHERIC BOUNDARY LAYER

A Thesis
Presented to
the Faculty of the Department
of Chemical Engineering
University of Houston

In Partial Fulfillment
of the Requirements for the Degree
Master of Science in Chemical Engineering

by
Javier Huitron
August 1977

ACKNOWLEDGEMENTS

I want to express my gratitude to my advisor, Dr. Frank L. Worley, for his guidance and to the Department of Chemical Engineering for financial support during the course of this work. I am also indebted to my friends, Miss Christine Nicknish for her comments on the first draft of this Thesis and to Mr. Arturo Gallegos for drawing the Figures of Chapter VI.

WIND TUNNEL SIMULATION OF THE
ATMOSPHERIC BOUNDARY LAYER

An Abstract of a Thesis
Presented to
the Faculty of the Department
of Chemical Engineering
University of Houston

In Partial Fulfillment
of the Requirements for the Degree
Master of Science in Chemical Engineering

by
Javier Huitron
August 1977

ABSTRACT

The wind tunnel simulation of the Atmospheric Boundary Layer (A B L) under various stabilities was undertaken in order to study atmospheric diffusion and air pollution .

A literature review of the methods currently employed was made . A description of the A B L characteristics as a function of stability was obtained from the literature .

Turbulence producing devices such as barriers , rough floors and screens were used to simulate various atmospheric stabilities . Wind tunnel data of instantaneous velocity , turbulence intensities , energy spectrum and length scales as well as a few visualization tests were obtained .

A simulation criteria based on the matching of statistical quantities was applied to the wind tunnel data for evaluation of stability . Finally , techniques for the simulation of the neutral , neutral/slightly stable and neutral/slightly unstable A B L were developed .

TABLE OF CONTENTS

CHAPTER	PAGE
I. INTRODUCTION	1
II. ANALYTICAL ASPECTS	3
Atmospheric Fluid Mechanics	3
Basic Equations	3
Boundary Layer Equations	7
Atmospheric Stability	14
Statistical Description of Turbulence	20
Effect of Atmospheric Stability on Velocity Profile	24
Effect of Atmospheric Stability on Turbulence Intensities, Energy Spectrum and Length Scales	25
Atmospheric Diffusion	26
Gradient Transfer Theory	26
Similarity Theory Approach	27
Statistical Theory Approach	28
Effect of Correlation Coefficient Shape	29
Importance of the Low Frequency range of the Energy Spectrum	32
Relationship between Lagrangian and Eulerian Quantities	32
Effect of Shear	34
Similarity Criteria	34

CHAPTER	PAGE
III. ATMOSPHERIC BOUNDARY LAYER DESCRIPTION	40
Boundary and Surface Layers' Heights	40
Mean Velocity Profile	42
Roughness Length	43
Reynolds Stresses (\overline{uw})	43
Friction Velocity, u_*	44
Turbulence Intensities	44
Energy Spectra	48
Length Scales	54
IV. PREVIOUS WORK AND PRESENT WORK SIMULATION	
APPROACH	57
Previous Work	57
Present Work Simulation Approach	67
V. DESCRIPTION OF EXPERIMENTAL TECHNIQUE	73
Environmental Wind Tunnel Characteristics .	73
Instrumentation	79
Analysis of Data	85
VI. EXPERIMENTAL RESULTS	93
Turbulence Generating Devices Effect on Flow Field	93
Velocity Effect	98
Roughness Effect	102
Change of Surface. Transition Effects . .	109
Barrier Effect	111

CHAPTER	PAGE
Vortex Generators Effect	119
Cross-stream Horizontal Homogeneity	120
Simulation of Atmospheric Flows	127
Neutral Stability Simulation	128
Simulation of the Stable Atmosphere	137
Simulation of the Unstable Atmosphere	147
VII. SUMMARY OF RESULTS AND RECOMMENDATIONS	163
BIBLIOGRAPHY	166
APPENDIX	173
A. Pressure Transducer Calibration	173
B. Hot-wire Anemometer Calibration	175
C. Evaluation of Digitization Program	178
D. Low-Pass Filter Performance	181
E. Computer Program Input and Control Data	182
F. Reported Runs Main Parameters	184
G. Nomenclature	186

LIST OF TABLES

TABLE		PAGE
2.1	Pasquill-Gifford Stability Categories . . .	19
2.2	Estimates of the Correspondence between Pasquill's Stability Categories, R_i and L for Short Grass	19
3.1	Vertical and Lateral Turbulence Intensities as a Function of Atmospheric Stability in the Surface Layer	45
3.2	Longitudinal Turbulence Intensity for Neutral Stability in the Surface Layer	46
3.3	Dimensionless Length Scales as a Function of R_i Number	56
4.1	Review of Atmospheric Boundary Layer Simulation	58
5.1	Environmental Wind Tunnel Main Characteristics	75
5.2	Vibration Measurements on Test Section . .	79
6.1	Boundary Layer Characteristics	96
6.2	Effect of Roughness on Vertical Length Scales	108
6.3	Turbulence Intensities in the Lower Third of the Boundary Layer. Neutral Simulation .	129
6.4	Turbulence Intensities in the Lower Third of the Boundary Layer. Stable Simulation . .	140
6.5	Turbulence Intensities as a Function of the position of the 3 in. Barrier on the working section	148
6.6	Turbulence Intensities in the Lower Third of the Boundary Layer. Unstable Simulation .	152
6.7	Length Scales for the Sand Roughness and Sand Roughness + 3 in. Barrier at 3.66 m Configurations	158
6.8	Evaluation of A B L Simulation	162

LIST OF FIGURES

FIGURE		PAGE
2.1	Effect of Correlation curve shape on dispersion	31
2.2	Effect of time of travel (T) on the dispersion of particles from a continuous point source in homogeneous turbulence. .	31
3.1	Boundary layer height and Power Law index . Neutral A B L	41
3.2	Power Law index as a function of stability.	41
3.3	Generalized w spectrum	50
3.4	Generalized u spectrum	50
3.5	Generalized v spectrum	50
3.6	Unstable Energy Spectrum	52
3.7	Stable Energy Spectrum	53
5.1	Plan view of Environmental Wind Tunnel . .	74
5.2	Instrument Carriage	78
5.3	Driving mechanism for vertical and lateral motion of the probe in the instrument carriage	78
5.4	Probe holder	80
5.5	Probe holding system	81
5.6	Instrumentation schematic diagram	82
5.7	Smoke generator	92
6.1	Roughness effect on mean velocity profile .	99
6.2	Law of the Wall. Roughness and velocity effect	100
6.3	Velocity Defect. Roughness and velocity effect	101
6.4	Roughness effect on turbulence intensities.	105

FIGURE		PAGE
6.5	Roughness effect on turbulence intensities and Reynolds stresses	106
6.6	Law of the Wall. Transition rough/smooth effect	110
6.7	Barrier effect on mean velocity profile . .	112
6.8	Barrier effect on turbulence intensities .	114
6.9	Barrier effect on lateral turbulence intensities and Reynolds stresses	115
6.10	Effect of placing a 3" barrier at a distance X on turbulence intensities and Reynolds stresses	117
6.11	Barrier effect on length scales	118
6.12	Vortex generators effect on velocity profile and turbulence intensities . . .	121
6.13	Vortex generators effect on vertical turbulence intensities and Reynolds stresses (\overline{uw})	122
6.14	Mean velocity profile cross-stream horizontal homogeneity	124
6.15	Turbulence intensities. Cross-stream horizontal homogeneity	125
6.16	Reynolds stresses cross-stream horizontal homogeneity	126
6.17	Neutral atmosphere simulation. Turbulence intensities	130
6.18	Neutral atmosphere simulation. Vertical velocity energy spectrum	132
6.19	Neutral atmosphere simulation. Lateral velocity energy spectrum	133
6.20	Neutral atmosphere simulation. Vertical and lateral length scales	135
6.21	Stable atmosphere simulation. Turbulence intensities	139

FIGURE		PAGE
6.22	Stable atmosphere simulation. Vertical velocity energy spectrum	142
6.23	Stable atmosphere simulation. Lateral velocity energy spectrum	144
6.24	Stable atmosphere simulation. Vertical and lateral length scales	145
6.25	Effect of placing the 3" barrier at various X (m). Vertical velocity energy spectrum.	150
6.26	Effect of placing the 3" barrier at various X (m). Lateral velocity energy spectrum .	151
6.27	Unstable atmosphere simulation. Turbulence intensities	153
6.28	Unstable atmosphere simulation. Vertical velocity energy spectrum	155
6.29	Unstable atmosphere simulation. Lateral velocity energy spectrum	156
6.30	Unstable atmosphere simulation. Vertical and lateral length scales	157
6.31	Flow visualization tests	160

CHAPTER I

INTRODUCTION

The diffusion of contaminants in the atmospheric boundary layer is a complex phenomenon. Field programs and mathematical and physical modelling have been used to study this phenomenon. Physical modelling is very attractive. Results from physical modelling are expected to be more accurate than those obtained by mathematical modelling, specially when studying complex geometries. Field programs produce the most accurate results, but they are very expensive and require long completion times.

In the last ten years, most of the physical modelling work has been done in wind tunnels rather than in other devices, e.g. water tanks. The simulation of the neutral atmospheric boundary layer, i.e. when buoyancy effects are not present, has been achieved by various investigators. However, the simulation of various atmospheric stabilities is a very difficult problem, and success on this area has been rather limited. Various investigators, e.g. Cermak (8) , at Colorado State University, Schon, et al. (61) at the Laboratoire de Mecanique des Fluids (France), and others have, nevertheless, been able to reproduce atmospheric flows of various stabilities by imposing a temperature profile on the wind tunnel flow.

The objective of the present work was to develop wind -

tunnel techniques for the simulation of the atmosphere under various stabilities, using turbulence producing devices such as barriers, vortex generators, various floor roughnesses, and screens. Such studies were done in the University of Houston Environmental Wind Tunnel. In order to study the characteristics of the developed flows, measurements of quantities such as mean velocity, turbulence intensities, energy spectra and length scales, and a few visualization tests were made. The comparison of the wind tunnel developed flows against atmospheric flows was used to evaluate the techniques developed in this work.

CHAPTER II

ANALYTICAL ASPECTS

Atmospheric Fluid Mechanics

Basic Equations

The fluid mechanics behavior of the region of the atmosphere close to the Earth's surface is that of a turbulent boundary layer. In this section the fluid mechanics aspects of such atmospheric or planetary boundary layer will be discussed.

The basic equations for a compressible, Newtonian fluid subject to a gravitational field are

Continuity equation:

$$\frac{\partial}{\partial t} \rho + \frac{\partial}{\partial x_i} (\rho u_i) = 0 \quad (2.1)$$

Tensor notation is used throughout the present work. Definition of symbols is found in the Nomenclature Section.

Momentum equation:

$$\rho \left\{ \left(\frac{\partial u_i}{\partial t} + u_j \frac{\partial u_i}{\partial x_j} \right) + 2 \varepsilon_{ijk} u_k \Omega_j \right\} = \frac{\partial}{\partial x_k} \left[2 \mu S_{ik} - \left(P + \frac{2}{3} \mu \frac{\partial u_j}{\partial x_j} \right) \delta_{ik} \right] - \rho g \delta_{3i} \quad (2.2)$$

where the term $2 \varepsilon_{ijk} u_k \Omega_j$, called the Coriolis force, has arisen because it has been considered a coordinates system that rotates with respect to an inertial frame of reference. The mag-

nitude of this term is negligible in the surface layer (up to approx. 100 m from the Earth's surface). It will be discussed later.

S_{ik} is the rate of strain tensor defined as:

$$S_{ik} = \frac{1}{2} \left(\frac{\partial u_i}{\partial x_k} + \frac{\partial u_k}{\partial x_i} \right) \quad (2.3)$$

δ_{ij} , the "Kronecker delta", is equal to one if $i=j$, and equal to zero otherwise. ϵ_{ijk} , the "alternating tensor" is equal to one if $ijk=123,312,231$; equal to minus one if $ijk=321,213,132$, and equal to zero if anyone of ijk is repeated.

Energy equation:

$$\rho \left(\frac{\partial E}{\partial t} + u_j \frac{\partial E}{\partial x_j} \right) = k \frac{\partial^2 T}{\partial x_j \partial x_j} - P \frac{\partial u_j}{\partial x_j} + \Phi + Q \quad (2.4)$$

Where:

$$\partial E = c_v dT \quad (2.4a)$$

$$\Phi = 2 \nu S_{ij} S_{ij} \quad (2.4b)$$

and Q represents heat sources.

It is assumed that the air in the atmosphere follows the Ideal Gas Law:

$$P = \frac{\rho R T}{M_a} \quad (2.5)$$

Decomposing P , ρ and T as the sum of an equilibrium value which is the sum of the surface value plus some function of height and a correction due to motion, i.e.

$$P = P_0 + P_m(z) + \tilde{P} \quad (2.6a)$$

$$T = T_0 + T_m(z) + \tilde{T} \quad (2.6b)$$

$$\rho = \rho_0 + \rho_m(z) + \tilde{\rho} \quad (2.6c)$$

and considering a shallow layer in which the Bousinesq approximations are valid (Spiegel and Veronis(72), Seinfeld(62)), i.e.

$$a) \quad P_m(z)/P_0, T_m(z)/T_0, \rho_m(z)/\rho_0 \ll 1$$

$$b) \quad P/P_0, T/T_0, \tilde{\rho}/\rho_0 \ll 1$$

c) Deviations in density can be attributed solely to temperature deviations.

It can be shown, see for example Seinfeld(62), that the approximate equations for the atmosphere are

Continuity equation:

$$\frac{\partial u_i}{\partial x_i} = 0 \quad (2.7)$$

Momentum equation:

$$\begin{aligned} \frac{\partial u_i}{\partial t} + u_j \frac{\partial u_i}{\partial x_j} + 2 \varepsilon_{ijk} u_k \Omega_j = - \frac{1}{\rho_0} \frac{\partial \tilde{P}}{\partial x_i} + \\ \frac{\mu}{\rho_0} \frac{\partial^2 u_i}{\partial x_j \partial x_j} + g \frac{\tilde{T}}{T_0} \delta_{3i} \end{aligned} \quad (2.8)$$

Energy equation:

$$\rho c_p \left(\frac{\partial \theta}{\partial t} + u_j \frac{\partial \theta}{\partial x_j} \right) = k \frac{\partial^2 \theta}{\partial x_j \partial x_j} + Q \quad (2.9)$$

Note that here Φ has been neglected. An adiabatic reference equilibrium state has been chosen such that:

$$\theta = T - z \Gamma \quad (2.10)$$

where Γ is the adiabatic lapse rate (approx. $1^\circ\text{C}/100 \text{ m}$) and θ is called the "potential temperature" (this is discussed in more detail later in this chapter).

The instantaneous values of U_i , P and θ can be decomposed into a mean and a fluctuation, i.e.

$$u_i = \bar{u}_i + u_i \quad (2.11a)$$

$$\theta = \bar{\theta} + \theta \quad (2.11b)$$

$$p = \bar{p} + p \quad (2.11c)$$

Substituting these into equations (2.7), (2.8), and (2.9) and averaging the resultant equations in time, the equations for the mean quantities are obtained

Continuity equation:

$$\frac{\partial \bar{u}_i}{\partial x_i} = 0 \quad (2.12)$$

Momentum equation:

$$\frac{\partial \bar{u}_i}{\partial t} + \frac{\partial}{\partial x_j} (\overline{u_i u_j}) = -\frac{1}{\rho} \frac{\partial \bar{p}}{\partial x_i} + \frac{\partial}{\partial x_j} \left(\nu \frac{\partial \bar{u}_i}{\partial x_j} - \overline{u_i u_j} \right) + \frac{g}{T_0} \bar{\theta} \delta_{i3} \quad (2.13)$$

Energy equation:

$$\rho_0 c_p \left(\frac{\partial \bar{\theta}}{\partial t} + \bar{u}_j \frac{\partial \bar{\theta}}{\partial x_j} \right) = \frac{\partial}{\partial x_j} \left(k \frac{\partial \bar{\theta}}{\partial x_j} - \rho_0 c_p \overline{u_j \theta} \right) \quad (2.14)$$

Boundary Layer Equations

When the equation of motion for the mean quantities (equation 2.13) is applied to a boundary layer where the flow is steady, incompressible, two-dimensional, over a smooth surface, and buoyancy forces are not considered, there results:

$$\bar{u} \frac{\partial \bar{u}}{\partial x} + \bar{w} \frac{\partial \bar{w}}{\partial z} = -\frac{1}{\rho} \frac{\partial p}{\partial x} + \frac{\partial}{\partial z} \left(-\bar{u}\bar{w} + \nu \frac{\partial \bar{u}}{\partial z} \right) \frac{\partial}{\partial x} \left(-\bar{u}^2 + \nu \frac{\partial \bar{u}}{\partial x} \right) \quad (2.15)$$

$$\bar{u} \frac{\partial \bar{w}}{\partial x} + \bar{w} \frac{\partial \bar{w}}{\partial z} = -\frac{1}{\rho} \frac{\partial p}{\partial z} + \frac{\partial}{\partial z} \left(-\bar{w}^2 + \nu \frac{\partial \bar{w}}{\partial z} \right) + \frac{\partial}{\partial x} \left(-\bar{u}\bar{w} + \nu \frac{\partial \bar{w}}{\partial x} \right) \quad (2.16)$$

$$\frac{\partial \bar{u}}{\partial x} + \frac{\partial \bar{w}}{\partial z} = 0 \quad (2.17)$$

In this section the treatment given in Tennekes and Lumley (77) is closely followed. If an order of magnitude analysis on equation (2.15) is performed and the resulting equation cast in terms of the velocity defect ($U - U_0$), the approximate equation for a boundary layer is obtained:

$$\bar{u}_0 \frac{\partial}{\partial x} (\bar{u} - \bar{u}_0) + (\bar{u} - \bar{u}_0) \frac{d\bar{u}_0}{dx} + (\bar{u} - \bar{u}_0) \cdot \frac{\partial}{\partial x} (\bar{u} - \bar{u}_0) + \bar{w} \frac{\partial}{\partial z} (\bar{u} - \bar{u}_0) = \frac{\partial}{\partial z} \left(-\bar{u}\bar{w} + \nu \frac{\partial \bar{u}}{\partial z} \right) \quad (2.18)$$

Rearranging this equation and using the continuity equation (2.17):

$$\frac{\partial}{\partial x} [\bar{u}(\bar{u} - \bar{u}_o)] + \frac{\partial}{\partial z} [\bar{w}(\bar{u} - \bar{u}_o)] + (\bar{u} - \bar{u}_o) \frac{d\bar{u}_o}{dx} = \frac{\partial}{\partial z} (-\bar{u}\bar{w} + \nu \frac{\partial \bar{u}}{\partial z}) \quad (2.19)$$

By integration of the last equation:

$$- \frac{d}{dx} \int_0^{\infty} \bar{u}(\bar{u} - \bar{u}_o) dz - \frac{d\bar{u}_o}{dx} \int_0^{\infty} (\bar{u} - \bar{u}_o) dz = u_*^2 \quad (2.20)$$

where u_* is the friction velocity defined as:

$$u_* = \left(\frac{\tau_o}{\rho} \right)^{1/2} \quad (2.21)$$

and τ_o is the wall shear stress.

Let us define a normalized boundary layer thickness:

$$\Delta = \frac{1}{u_*} \int_0^{\infty} (\bar{u}_o - \bar{u}) dz \quad (2.22)$$

Further order of magnitude analysis on equation (2.20) under the assumptions $\bar{u} \sim \bar{u}_o$ and $u_* \ll \bar{u}_o$ yields:

$$\frac{d}{dx} (\Delta u_* \bar{u}_o) + \Delta u_* \frac{d\bar{u}_o}{dx} = u_*^2 \quad (2.23)$$

The above equation is known as the "momentum integral".

With further manipulation of equation (2.18) and assuming

$u_*/\bar{u}_o \ll 1$, the equation of motion for the outer layer becomes:

$$\bar{u}_o \frac{\partial}{\partial x} (\bar{u} - \bar{u}_o) + (\bar{u} - \bar{u}_o) \frac{d\bar{u}_o}{dx} - z \frac{d\bar{u}_o}{dx} \frac{\partial}{\partial z} \cdot (\bar{u} - \bar{u}_o) = \frac{\partial}{\partial z} \bar{u}\bar{w} \quad (2.24)$$

This equation is linear in the velocity defect ($\bar{U} - \bar{U}_0$) and is called the "linearized boundary layer equation".

The aim of this development is to find solutions of the form:

$$\frac{\bar{u} - \bar{u}_0}{u_*} = F(\eta) \quad (2.25)$$

$$- \frac{u\omega}{u_*^2} = G(\eta) \quad (2.26)$$

where $\eta = z/\Delta$, such that $F(\eta)$ is independent of the downstream distance "x", i.e. a self preserving solution. A self preserving solution should be asymptotically independent of the Reynolds number. Flows exhibiting self-preservation are called "equilibrium flows".

Substituting equations (2.25) and (2.26) into (2.18):

$$\frac{\Delta}{u_*^2} \frac{d}{dx} (\bar{u}_0 u_*) F - \frac{1}{u_*} \frac{d}{dx} (\Delta \bar{u}_0) \eta \frac{dF}{d\eta} = \frac{dG}{d\eta} \quad (2.27)$$

If the coefficients of F and $\eta dF/d\eta$ could be made independent of "x", a self preserving solution would be obtained.

In the immediate vicinity of the wall, the characteristic length is equal to ν/u_* and the characteristic velocity is u_* . An order of magnitude analysis on equation (2.15) using these characteristic length and velocity leads to the conclusion that the inertial terms and the pressure gradient are negligible

in comparison with the stress term, so:

$$\frac{\partial}{\partial z} \left(-\overline{u\omega} + \nu \frac{\partial \bar{u}}{\partial z} \right) = 0 \quad (2.28)$$

The above equation defines a layer of constant stress.

Solutions of equation (2.28) are of the form:

$$\frac{\bar{u}}{u_*} = f \left(\frac{z u_*}{\nu} \right) \quad (2.29)$$

$$-\frac{u\omega}{u_*^2} = g \left(\frac{z u_*}{\nu} \right) \quad (2.30)$$

These are known as the "law of the wall". They can also be obtained by dimensional analysis, Hinze (26) sect. 7.5.

The velocity defect law and the law of the wall represent two regions of the boundary layer dominated by different length scales. Matching of these regions is done through a logarithmic velocity profile. It can be obtained by equating the velocity gradient from both velocity defect law equation (2.25) and the law of the wall, equation (2.29):

$$z_+ \frac{d}{dz_+} f(z_+) = \eta \frac{d}{d\eta} F(\eta) = \frac{1}{k} \quad (2.31)$$

where:

$$z_+ = z u_* / \nu \quad (2.31a)$$

and k is the Von Karman constant (equal to 0.4).

Equation (2.31) is integrated to obtain:

$$\frac{\bar{u}}{u_*} = \frac{1}{k} \ln \frac{z u_*}{\nu} + A \quad (2.32)$$

where "A" is a constant depending on the pressure gradient. When the boundary is rough with a characteristic height " ϵ ", the law of the wall becomes

$$\frac{\bar{u}}{u_*} = f\left(\frac{z}{\epsilon}\right) ; \quad \epsilon > \frac{\nu}{u_*} \quad (2.33)$$

and the logarithmic velocity profile becomes

$$\frac{\bar{u}}{u_*} = \frac{1}{k} \ln \frac{z}{\epsilon} + \text{const.} \quad (2.34a)$$

or

$$\frac{\bar{u}}{u_*} = \frac{1}{k} \ln \frac{z}{z_0} \quad (2.34b)$$

where z_0 is the "roughness length". For development of equations (2.33) and (2.34 b) see Seinfeld (62) sec. 5.5.1 or Hinze (26) sec. 7.5.

Substitution of $\bar{u} = \bar{u}_0$ for $z = \Delta$ in (2.32) yields a logarithmic friction law:

$$\frac{\bar{u}_0}{u_*} = \frac{1}{k} \ln \frac{\Delta u_*}{\nu} + A \quad (2.35a)$$

A differentiated form of this, which will be referenced to shortly, is

$$\left(1 + \frac{u_*}{k \bar{u}_0}\right) \frac{d}{dx} \left(\frac{\bar{u}_0}{u_*}\right) = \frac{1}{k \Delta} \frac{d\Delta}{dx} + \frac{1}{k \bar{u}_0} \frac{d\bar{u}_0}{dx} \quad (2.35b)$$

Returning to equation (2.27) and expanding its coefficients:

$$\frac{\Delta}{u_*^2} \frac{d}{dx} (\bar{u}_o u_*) = 2 \frac{\Delta}{u_*} \frac{d\bar{u}_o}{dx} + \frac{\Delta \bar{u}_o^2}{u_*^2} \frac{d}{dx} \left(\frac{u_*}{\bar{u}_o} \right) \quad (2.36)$$

$$\frac{1}{u_*^2} \frac{d}{dx} (\Delta \bar{u}_o) = \frac{\bar{u}_o}{u_*^2} \frac{d}{dx} (\Delta u_*) - \frac{\Delta \bar{u}_o}{u_*^2} \frac{d}{dx} \left(\frac{u_*}{\bar{u}_o} \right) \quad (2.37)$$

It is not obvious that the second term of the right hand side of (2.36) and (2.37) is negligible, but it can be shown by using equation (2.35b) under the assumption $u_*/\bar{u}_o \ll 1$.

The momentum integral equation (2.23) may be rearranged to:

$$\frac{\bar{u}_o}{u_*^2} \frac{d}{dx} (\Delta u_*) = 1 - 2 \frac{\Delta}{u_*} \frac{d\bar{u}_o}{dx} \quad (2.38)$$

A convenient pressure gradient parameter $\bar{\Pi}$ can be defined as:

$$\bar{\Pi} \equiv - \frac{\Delta}{u_*} \frac{d\bar{u}_o}{dx} \quad (2.39)$$

which is a ratio of two time scales, $(d\bar{u}_o/dx)^{-1}$ and Δ/u_* .

Rewriting equations (2.27) and (2.38) in terms of $\bar{\Pi}$:

$$- 2\bar{\Pi} F - (1 + 2\bar{\Pi}) \eta \frac{dF}{d\eta} = \frac{dG}{d\eta} \quad (2.40)$$

$$\frac{\bar{u}_o}{u_*} \frac{d}{dx} (\Delta u_*) = 1 + 2\bar{\Pi} \quad (2.41)$$

Equations (2.35a), (2.40) and (2.41) are subject to a normalization condition. From equations (2.22) and (2.25) :

$$\int_0^{\infty} F d\eta = 1 \quad (2.42)$$

Equation (2.40) is subject to the boundary conditions:

$$F \rightarrow 0, G \rightarrow 0 \quad \text{for } \eta \rightarrow \infty \quad (2.43a)$$

$$G \rightarrow 1 \quad \text{for } \eta \rightarrow 0 \quad (2.43b)$$

$$\eta \frac{dF}{d\eta} \rightarrow \frac{1}{k} \quad \text{for } \eta \rightarrow 0 \quad (2.43c)$$

The system of equations (2.35a, 2.40, 2.41, 2.42, 2.43 a, b, c) is independent of "x" if $\bar{\Pi}$ is a constant. We expect self preserving solutions for this system if the pressure distribution is such that it makes $\bar{\Pi}$ independent of "x". Reynolds number independence is also obtained asymptotically as $\Delta u_* / \nu \rightarrow \infty$. For a boundary layer in zero pressure gradient, $\bar{\Pi}=0$, equations (2.35a), (2.40), (2.41) become

$$\frac{\bar{u}_o}{u_*} = \frac{1}{k} \ln \frac{\Delta u_*}{\nu} + A(0) \quad (2.44)$$

Clauser (12) found $A(0)=4.9$ experimentally.

$$-\eta \frac{dF}{d\eta} = \frac{dG}{d\eta} \quad (2.45)$$

$$\frac{\bar{u}_o}{u_*^2} \frac{d}{dx} (\Delta u_*) = 1 \quad (2.46)$$

In the development of equation (2.41), it was assumed that $(\bar{U} = \bar{U}_o)$. This is equivalent with equating the momentum thickness, θ_M , to the displacement thickness δ_* :

$$\theta_M = \frac{1}{\bar{u}_o^2} \int_0^\infty \bar{u} (\bar{u}_o - \bar{u}) dz \quad (2.47)$$

$$\delta_* = \frac{1}{\bar{u}_o} \int_0^\infty (\bar{u}_o - \bar{u}) dz \quad (2.48)$$

The shape factor ($H = \delta_*/\theta_M$) should approach the value of unity asymptotically but experiments have shown, Clauser (12), that $H=1.3$ is representative of equilibrium boundary layers under zero pressure gradient. He also found a value of approx. 6.1 for the parameter C , defined as:

$$C \equiv \int_0^{\infty} F^2 d\eta \quad (2.49)$$

Atmospheric Stability.-

During the course of a day the atmospheric boundary layer passes through different states, characterized by its stability. Atmospheric turbulence is affected by the buoyancy effects arising from the existing temperature profile (lapse rate). The reference state is the neutral or adiabatic state in which a parcel of air experiences adiabatic expansion as it moves upward or downward into regions of smaller pressure. A more detailed derivation of what follows is found in Sutton (74).

Static Stability Criteria.-

Consider an air parcel which expands adiabatically through the lower atmosphere. Its change of temperature with height may be obtained by applying the First Law of Thermodynamics

$$dE = dQ - dW = c_v dT \quad (2.50)$$

and the equation for a fluid at rest subject to a gravitational field:

$$\frac{dP}{dz} = -\rho g \quad (2.51)$$

It can be shown that:

$$\frac{dT}{dz} = -\frac{g}{c_p} = -\Gamma \quad (2.52a)$$

where Γ is the "adiabatic lapse rate" = $1^\circ\text{C}/100\text{m}$. It also can be shown, Sutton, (74); Seinfeld, (62), that:

$$\theta = T \left(\frac{p}{p_0} \right)^{-(\gamma-1)/\gamma} \quad (2.53)$$

where θ , the "potential temperature", is the temperature which a parcel of air will acquire if brought adiabatically from one elevation in the atmosphere at T, P to another at P_0 . For a parcel of air which rises adiabatically in an atmosphere having a lapse rate Λ , it is possible to obtain

$$\frac{dT}{dz} = -\Gamma \left(\frac{T_0' - \Lambda z}{T_0'} \right)^{(\Gamma - \Lambda)/\Lambda} \frac{T_0}{T_0'} \quad (2.52b)$$

where T_0' is the temperature of the surrounding air at elevation z . If the lapse rate is adiabatic, the air parcel is always at static equilibrium with the surrounding air. However because of surface heating by the sun and local weather influences, the atmosphere is seldom adiabatic for long periods of time.

The atmosphere is said to be

- a) Neutral.- The lapse rate is adiabatic ($\Lambda = \Gamma$). There is no net buoyancy force.
- b) Unstable.- The lapse rate cools faster than the adiabatic ($\Lambda > \Gamma$). The buoyancy forces enhance vertical motion.

c) Stable.- The lapse rate cools slower than the adiabatic ($\Delta < \Gamma$). The temperature profile may in fact increase with height (inversion). The buoyancy forces oppose vertical motion.

Dynamic Stability Criteria.-

A quantitative way to assess stability is obtained by looking at the equation for the mean kinetic energy of the turbulence. This equation is obtained by multiplying the momentum equation for the instantaneous velocity by U_i and subtracting the kinetic energy of the mean flow, see for example Tennekes and Lumley (77). The result after the addition of a buoyancy term is

$$\begin{aligned} \bar{u}_j \frac{\partial}{\partial x_j} \left(\frac{1}{2} \overline{u_i u_i} \right) = & - \frac{\partial}{\partial x_j} \left(\frac{1}{\rho} \overline{u_j p} + \frac{1}{2} \overline{u_i u_i u_j} - 2\nu \overline{u_i s_{ij}} - \right. \\ & \left. \overline{u_i u_j} S_{ij} - 2\nu \overline{s_{ij} s_{ij}} + \frac{g}{T_e} \overline{u_3 \theta} \right) \quad (2.54) \end{aligned}$$

It can be shown that for steady shear flow, homogeneous in the xy plane, for $Re \rightarrow \infty$

$$\begin{aligned} 0 = & - \overline{u w} \frac{\partial \bar{u}}{\partial z} + \frac{g}{T_e} \overline{\theta w} - \frac{\partial}{\partial z} \left(\frac{1}{2} \overline{u_i u_i w} + \right. \\ & \left. \frac{1}{\rho} \overline{p w} \right) - \nu \overline{\frac{\partial u_i}{\partial x_j} \frac{\partial u_i}{\partial x_j}} \quad (2.55) \end{aligned}$$

In this equation u_1 and u_3 have been replaced by u and w respectively. The important terms pertaining to this discussion are: the first, production of kinetic energy by shear stress and ,

the second, production of kinetic energy by buoyancy. The flux Richardson Number Rf is defined as the ratio of production of kinetic energy by buoyancy to that by shear stress.

$$Rf \equiv \frac{(g/T_e) \overline{\theta w}}{\overline{uw} (\partial \bar{u} / \partial z)} \quad (2.56)$$

The sign of $\overline{\theta w}$ defines the sign of Rf and so indicates whether the kinetic energy is produced or destroyed by buoyancy. In the surface layer of the atmosphere the shear stress and the heat flux q are considered constant so:

$$-\rho \overline{uw} = \rho u_*^2 \quad (2.57)$$

$$\bar{q}_3 = \rho c_p \overline{\theta w} = \text{const.} \quad (2.58)$$

and the velocity profile is logarithmic (near neutral conditions), i.e.,

$$\frac{d\bar{u}}{dz} = \frac{u_*}{kz} \quad (2.59)$$

substituting these into the Rf definition:

$$Rf = - \frac{kgz \bar{q}_3}{\rho c_p T_0 u_*^3} \quad (2.60)$$

Rf can be written as a dimensionless length

$$Rf = \frac{z}{L} \quad (2.61)$$

where

$$L = - \frac{\rho c_p T_0 u_*^3}{k g \bar{q}_3} \quad (2.62)$$

L is known as the Monin-Obuknov length. Stability, expressed

as a function of L , becomes

$$L > 0 \quad \text{stable} \quad \bar{q}_3 < 0$$

$$L < 0 \quad \text{unstable} \quad \bar{q}_3 > 0$$

$$L = \infty \quad \text{neutral} \quad \bar{q}_3 = 0$$

A more practical form of the Richardson Number may be obtained by substitution of the gradient transport relations for the Reynolds stresses and heat flux, i.e.,

$$\rho \overline{uw} = -\rho K_M \frac{d\bar{u}}{dz} \quad (2.63)$$

$$\rho c_p \overline{\theta w} = \rho c_p K_T \frac{d\bar{\theta}}{dz} \quad (2.64)$$

into equation (2.56), so:

$$Rf = \frac{K_T}{K_M} \frac{g}{T_0} \frac{d\bar{\theta}/dz}{(d\bar{u}/dz)^2} \quad (2.65)$$

in order to isolate K_t/k_m , define:

$$Ri = \frac{g}{T_0} \frac{d\bar{\theta}/dz}{(d\bar{u}/dz)^2} \quad (2.66)$$

such that:

$$Rf = \frac{K_T}{K_M} Ri \quad (2.67)$$

A practical but somewhat qualitative way to determine atmospheric stability by observation of the insolation, cloudiness and wind velocity is given by the Pasquill-Gifford stability categories. See Table 2.1. This table is based on experimen-

TABLE 2.1

PASQUILL-GIFFORD STABILITY CATEGORIES

Surface wind speed (m/s)	Daytime insolation			Nighttime conditions	
	Strong	Moderate	Slight	Thin overcast or $\frac{1}{2}$ cloudiness [‡]	$\frac{3}{8}$ cloudiness
2	A	A-B	B		
2	A-B	B	C	E	F
4	B	B-C	C	D	E
6	C	C-D	D	D	D
6	C	D	D	D	D

A: Extremely unstable

D: Neutral conditions*

B: Moderately unstable

E: Slightly stable

C: Slightly unstable

F: Moderately stable

* Applicable to heavy overcast day or night

‡ The degree of cloudiness is defined as that fraction of the sky above the local apparent horizon which is covered by clouds.

TABLE 2.2

ESTIMATES OF THE CORRESPONDENCE BETWEEN PASQUILL'S STABILITY CATEGORIES , Ri AND L FOR SHORT GRASS

Stability category	Ri(at z=2m)	L(m)
A	-1. to -0.7	-2. to -3.
B	-0.5to -0.4	-4. to -5.
C	-.17to -.13	-12 to -15
D	0	∞
E	.03 to .05	35 to 75
F	.05 to .11	8 to 35

tal observation of the dispersion of real plumes. Pasquill and Smith (57) estimated the correspondence between L , Ri and the Pasquill-Gifford stability categories (for short grass ground). See Table 2.2 .

Statistical Description of Turbulence.-

The instantaneous velocity, U_i , in a turbulent field is a random function of time. In order to describe the properties of random velocities a statistical approach is used. Some concepts and definitions are given briefly for further reference. For a detailed treatment, refer to Tennekes and Lumley (77) or Hinze (26) .

A Lagrangian description is one which follows the motion of a marked particle in a flow field. An Eulerian description studies the motion of particles passing through a fixed point in a coordinates frame moving with the mean velocity of the flow field. Eulerian velocities will be indicated by U_i and Lagrangian velocities by V_i .

Turbulence is stationary if all statistical properties (mean value, variance, etc.) are independent of time; homogeneous if all statistical properties are independent of location in the field; isotropic if all statistical properties are independent of the orientation of the coordinates axes.

The mean of a random function like $U_i(x,t)$ should be computed in theory by an ensemble average, i.e. averaging over

an infinite number of repeated experiments. When $U_i(x,t)$ is a stationary function, by the ergodic hypothesis, one can equate ensemble averages to time averages. A time average is obtained by doing one experiment and averaging over a long period of time, i.e.:

$$\bar{u}_i(\underline{x}) = \lim_{T \rightarrow \infty} \frac{1}{T} \int_{t_0}^{t_0+T} u_i(\underline{x}, t) dt \quad (2.68)$$

In what follows, only Eulerian quantities will be actually defined; however, note that Eulerian and Lagrangian definitions are identical except that the velocity $U_i(x,t)$ for Eulerian definitions, should be replaced by $V_i(a,t)$ for Lagrangian ones.

The Correlation Coefficient is defined as:

$$R_{u_i u_j}(\underline{r}) = \frac{\overline{u_i(\underline{x}, t) u_j(\underline{x} + \underline{r}, t)}}{u_i' u_j'} \quad (2.69)$$

$$R_{u_i u_j}(\tau) = \frac{\overline{u_i(t) u_j(t + \tau)}}{u_i' u_j'} \quad (2.70)$$

An overbar indicates a time average and u_i' and u_j' are root mean square values of the fluctuating velocities. $R_{u_i u_j}(\underline{r})$ is a space correlation and is a measure of the correlation existing between velocities separated by a distance \underline{r} at the same time. $R_{u_i u_j}(\tau)$ is a time correlation, it is a measure of the correlation existing between velocities at different time " τ " at the same point in space.

If $u_i = u_j$, it is an autocorrelation. The most commonly used are the autocorrelations in the direction of the mean

flow (r_1). Integration of the autocorrelation coefficient curve leads to a length or time scale:

$$L_{u_i, r_1} = \int_0^{\infty} R_{u_i u_i}(r_1) dr_1 \quad (2.71)$$

$$T_{u_i, r_1} = \int_0^{\infty} R_{u_i u_i}(\tau) d\tau \quad (2.72)$$

where L_{u_i, r_1} is the integral length scale corresponding to $R_{u_i u_i}(r_1)$ in the direction of the mean flow. T_{u_i, r_1} is the time scale corresponding to $R_{u_i u_i}(\tau)$ again in the direction of the mean flow. They are a measure of eddy size.

In the field has a uniform velocity \bar{u} and $u \ll \bar{u}$, there is a simple relationship between spatial and time correlations known as Taylor Hypothesis. This hypothesis postulates a frozen turbulence field. Since $r_1 = \bar{u}t$:

$$L_{u_i, r_1} = \bar{u} T_{u_i, r_1} \quad (2.73)$$

see for example, Teunissen (80).

The correlation coefficient and energy spectrum are Fourier transform pairs. In what follows, the time energy spectrum and correlation coefficient are defined in terms of the frequency n , as is customarily used in atmospheric meteorology.

$$S_{u_i u_j}(n) \equiv 2 \int_{-\infty}^{\infty} \exp(-i 2 \pi n \tau) R_{u_i u_j}(\tau) d\tau \quad (2.74)$$

$$R_{u_i u_j}(\tau) \equiv \frac{1}{2} \int_{-\infty}^{\infty} \exp(i 2 \pi n \tau) S_{u_i u_j}(n) dn \quad (2.75)$$

The energy spectrum is a representation of the fraction of kinetic energy existing at a particular frequency for the spectrum of frequency. By using the fact that $S_{u_i u_i}(n)$ and $R_{u_i u_i}(\tau)$ are symmetric functions:

$$S_{u_i u_i}(n) = 4 \int_0^{\infty} \cos(2\pi n\tau) R_{u_i u_i}(\tau) d\tau \quad (2.76)$$

$$R_{u_i u_i}(\tau) = \int_0^{\infty} \cos(2\pi n\tau) S_{u_i u_i}(n) dn \quad (2.77)$$

Note that:

$$R_{u_i u_i}(0) = \int_0^{\infty} S_{u_i u_i}(n) dn = \overline{u_i'^2} \quad (2.78)$$

where $\overline{u_i'^2}$ is known as the variance. The turbulence intensity is defined as the ratio of the root mean square velocity, u_i' , to the mean velocity U .

A convenient way to represent the energy spectrum in dimensionless form is obtained by dimensional and similarity considerations. According to this: see e.g. Pasquill (56), "The basic hypothesis is that the variance and energy spectrum should be expressible in terms of the characteristic velocity and length scales, u_* and L , the height z (in the surface layer), the frequency n and by Taylor's Hypothesis, of the mean wind speed U ".

That is:

$$\frac{n S(n)}{(u_i')^2} = G\left(\frac{n z}{U}, \frac{z}{L}\right) \quad (2.79)$$

$$\frac{u_i'}{u_*} = F\left(\frac{z}{L}\right) \quad (2.80)$$

G and F reduce to $G(nz/\bar{U})$ and a constant respectively for neutral conditions.

It is customary to divide the energy spectrum into three frequency regions, according to the function that is performed in each region. These regions are: Energy-containing eddies range, Inertial subrange and range of Viscous dissipation. See Figure 2.2 . Energy is extracted from the mean flow by the large eddies, transferred through the inertial subrange and eventually dissipated in the viscous dissipation range.

Effect of Atmospheric Stability on Velocity Profile .

By dimensional analysis when the atmosphere is near neutral, Seinfeld (62) Sec.5.5.3 :

$$\frac{\partial \bar{u}}{\partial z} = \frac{u_*}{k L} g\left(\frac{z}{L}\right) \quad (2.81a)$$

which can be written as :

$$\frac{\partial \bar{u}}{\partial z} = \frac{u_*}{k z} \phi\left(\frac{z}{L}\right) \quad (2.81b)$$

the function $\phi(z/L)$ has to be such that $\lim(z/L) \rightarrow 0$, $\phi(z/L)=1$. Expanding $\phi(z/L)$ in a power series, truncating, substituting into (2.81b) and integrating:

$$\bar{u}(z) = \frac{u_*}{k} \left(\ln \frac{z}{z_0} + \beta \frac{z-z_0}{L} \right) \quad (2.82)$$

Experimental values of β are given by Plate (58) as :

unstable	$\beta = 3 - 6$
stable	$\beta = 5 - 7$

For stable conditions \bar{U} increases more rapidly with z than the neutral case, the opposite occurs under unstable conditions.

Note that equation (2.82) holds for small values of z/L .

For large z/L , another formula has to be used. Monin and Yaglom (47) Sec. 7.4 suggest :

Unstable :

$$\phi(z/L) = \left(1 - \beta' \frac{z}{L}\right)^{-1/4} \quad (2.83)$$

where $\beta' = 15$, Plate (58).

Stable :

$$\phi(z/L) = 4.2 \left(\frac{z}{L}\right)^{0.3}; \quad 0.1 \leq \frac{z}{L} \leq 0.2 \quad (2.84a)$$

or alternately :

$$\phi(z/L) = 1 + 4.7 \left(\frac{z}{L}\right) \quad (2.84b)$$

Effect of Atmospheric Stability on Turbulence Intensities, Energy Spectrum and Length Scales

The energy spectrum is a representation of the distribution of energy in a turbulent flow composed of a spectrum of frequencies. As it was discussed before, the effect of buoyancy forces is to increase or decrease the turbulent energy according to the stability. This results in that for an unstable atmosphere, the turbulent energy increases (particularly at low frequencies) with respect to the neutral case, e.g. Lumley and Panofsky (40) or Kaimal, et al. (35). The increased turbulent energy is reflected in the magnitude of the turbulence intensities, too. The length scale is also observed to increase

For the stable case the effect is the opposite.

The fact that the effect of instability on the energy spectrum is observed in the low frequency range is consistent with the fact that large eddies are the most effective in the transport of a contaminant, heat in this case. An extensive discussion of this will be given in the chapter on atmospheric boundary layer description.

Atmospheric Diffusion

Atmospheric diffusion has been studied by three theories: Gradient Transfer Theory, Similarity Theory and Statistical Approach.

Gradient Transfer Theory

This theory provides a relationship for the mass flux. Such relationship may be introduced in the equation of conservation of suspended material in an incompressible fluid without chemical reactions:

$$\frac{\partial \chi}{\partial t} = \frac{\partial}{\partial x_i} (u_i \chi) \quad (2.85)$$

which can be developed by substituting the total instantaneous quantities by the sum of a mean and a fluctuating quantity :

$$\frac{\partial \bar{\chi}}{\partial t} + \bar{u}_i \frac{\partial \bar{\chi}}{\partial x_i} = - \frac{\partial}{\partial x_i} (\overline{u_i \chi}) \quad (2.86)$$

Note that lower case letters denote fluctuating quantities. All characters have been defined in the "Nomenclature".

The relationship for the flux is

$$\overline{u_i x} = -K \frac{\partial \bar{x}}{\partial x_i} \quad (2.87)$$

$$K \cong \overline{u_i l} \quad (2.88)$$

For a detailed discussion of this, see for example, Pasquill (56). Substituting equation (2.87) into equation (2.86) and expanding :

$$\frac{d\bar{x}}{dt} = \frac{\partial}{\partial x} \left(K_x \frac{\partial \bar{x}}{\partial x} \right) + \frac{\partial}{\partial y} \left(K_y \frac{\partial \bar{x}}{\partial y} \right) + \frac{\partial}{\partial z} \left(K_z \frac{\partial \bar{x}}{\partial z} \right) \quad (2.89)$$

This theory is strictly applied when the length scale of the turbulence is much smaller than the characteristic length of the concentration field. This requirement is met when the pollution source is near a boundary, e.g. a ground level source.

Similarity Theory Approach

This approach was first introduced by Monin (46). A good discussion of this theory is found in Pasquill (56). The basic hypothesis of Lagrangian similarity is that the statistical properties of velocities of particles in the surface stress layer (the layer of constant momentum flux) are determined by just those parameters that determine the Eulerian properties, i.e. by u_* alone for neutral stability and, in addition, by the heat flux in stratified flow.

Dimensional analysis leads to :

$$\frac{d\bar{z}}{dt} = b u_* \phi \left(\frac{\bar{z}}{L} \right) \quad (2.90)$$

for passive particles injected singly at a point at $\bar{z}=0$.

\bar{z} is the vertical displacement, b is a constant and $\phi(z/L)$ a universal function to be specified. For neutral flow $\phi(z/L)=1$.

L is the Monin-Obukhov length defined as :

$$L = - \frac{\rho c_p T u_*^3}{k g \bar{q}_3} \quad (2.91)$$

It is further assumed that the rate of increase of the longitudinal average displacement \bar{X} is

$$\frac{d\bar{X}}{dt} = \bar{u} (c \bar{z}) \quad (2.92)$$

where c is another constant to be specified.

The final equations result from the substitution of the wind profile and the function $\phi(z/L)$. $\phi(z/L)$ is obtainable by dimensional considerations. This theory is valid in the surface layer for a ground level source or an elevated source only a few meters from the ground. See Pasquill (56) for further discussion of this point.

Statistical Theory Approach

This approach is based on the statistics of particle motion in a turbulent flow field. The particles are said to be small enough that they follow the streamlines totally. This theory is mainly due to G.I. Taylor (75) , who considered the displacement X of a marked particle in a homogeneous and stationary turbulence field. Taylor's formula is given in reference (75) . The resulting equation is

$$\overline{X_i^2} = 2 \int_0^T \int_0^t \overline{v_i(t) v_i(t+\tau)} d\tau dt \quad (2.93)$$

By substitution of the autocorrelation coefficient $R_{u_i u_i}(\tau)$ already defined :

$$\overline{X_i^2} = 2 \overline{v_i^2} \int_0^T \int_0^t R_{u_i u_i}(\tau) d\tau dt \quad (2.94)$$

$\overline{X_i^2}$ is the mean square displacement in the direction "i" of an ensemble of particles which started their motion from the same initial position.

Kampe de Feriet (36) offered an equivalent expression:

$$\overline{X_i^2} = 2 \overline{v_i^2} \int_0^T (T-t) R_{u_i u_i}(\tau) d\tau \quad (2.95)$$

which can be obtained by integrating by parts equation (2.94).

Observe that as $T \rightarrow 0$, since $R_{u_i u_i}(\tau) \cong 1$,

$$\overline{X_i^2} = \overline{v_i^2} T^2 ; T \rightarrow 0 \quad (2.96a)$$

or: $(\overline{X_i^2})^{1/2} = (\overline{v_i^2})^{1/2} T \quad (2.96b)$

When T is larger than the Lagrangian integral time scale t_L :

$$\overline{X_i^2} = 2 \overline{v_i^2} t_L T ; T > t_L \quad (2.97a)$$

or: $(\overline{X_i^2})^{1/2} = (2 \overline{v_i^2} t_L)^{1/2} T^{1/2} \quad (2.97b)$

Stating simply that the root mean square displacement is linear with respect to T for short times of travel from the original source. For values of $T > t_L$ the root mean square displacement is proportional to \sqrt{T} .

Effect of Correlation Coefficient shape

Let us consider the dispersion in the lateral direction

(turbulence is homogeneous and stationary) and assume two very different correlation coefficient shapes . A square such that:

$$\begin{aligned} R(\tau) &= 1 & ; & \tau \leq t_L & (2.98) \\ R(\tau) &= 0 & ; & \tau > t_L \end{aligned}$$

and an exponential curve ,

$$R(\tau) = \exp(-\tau/t_L) \quad (2.99)$$

Defining :

$$D^2 = \frac{\overline{X^2}}{t_L^2 v^2} \quad (2.100a)$$

and :

$$T' = T/t_L \quad (2.100b)$$

which limiting cases are

$$D = T' \quad ; \quad T \rightarrow 0 \quad (2.101a)$$

$$D = \sqrt{2T'} \quad ; \quad T \rightarrow \infty \quad (2.101b)$$

The effect of correlation shape on D as a function of T' is plotted in Figure 2.1 , as well as the two limiting cases, equations (2.101a) and (2.101b) .It is observed that the form of the D vs. T' curve is insensitive to wide variations of the shape of the Lagrangian correlation coefficient.It is also observed that a good approximation is provided even by the limiting expressions (2.100a) and (2.100b) alone.It is concluded that in the linear range (short T') the important parameter is $\sqrt{v^2}$ alone. In the parabolic range (long T') the t_L arises in addition to $\sqrt{v^2}$.According to this,a good first approximation can be obtained by having accurate values of v^2 and approximate values of t_L .

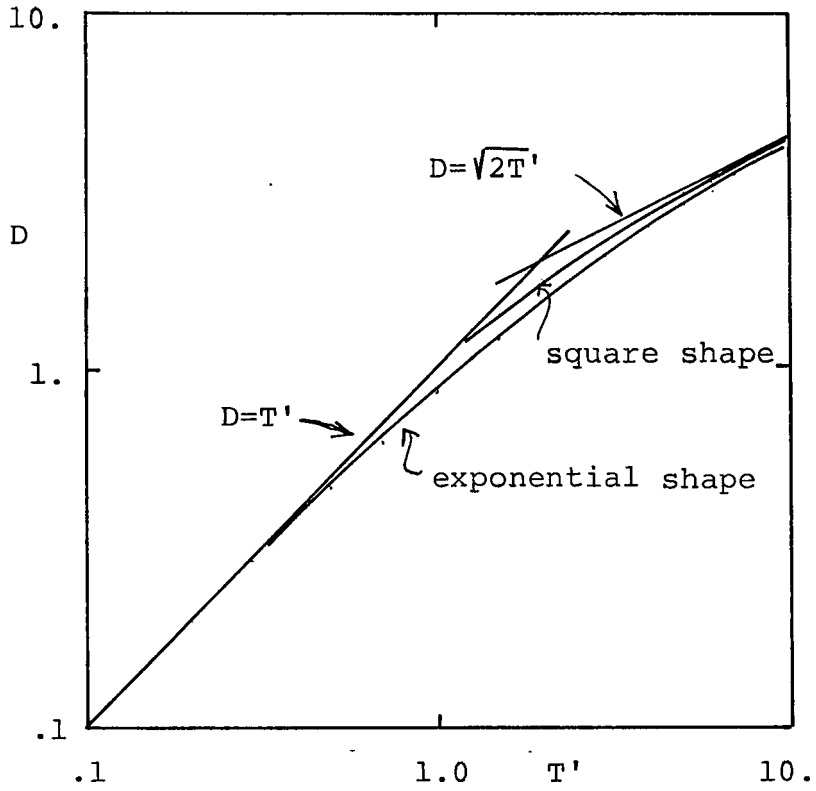


Figure 2.1.-Effect of Correlation curve shape on dispersion

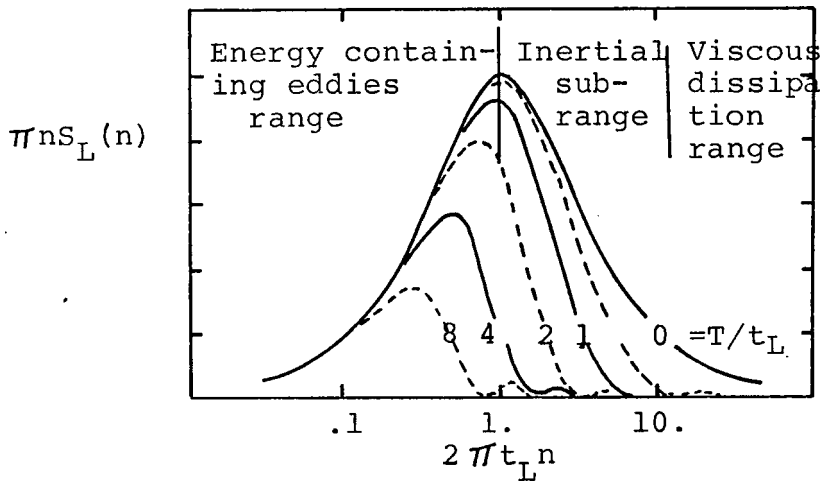


Figure 2.2.-Effect of time of travel (T) on the dispersion of particles from a continuous point source in homogeneous turbulence.

Importance of the Low Frequency Range of the Energy Spectrum

Substitution of the expressions for $R_{u_i u_i}(\tau)$, equation (2.77) into equation (2.95) yields:

$$\overline{X^2} = \overline{v^2} \int_0^{\infty} S_L(n) \left(\frac{1 - \cos 2\pi n T}{2(\pi n)^2} \right) dn \quad (2.102a)$$

and with further transformation :

$$\overline{X^2} = \overline{v^2} T^2 \int_0^{\infty} S_L(n) \frac{\sin^2 \pi n T}{(\pi n T)^2} dn \quad (2.102b)$$

Similar expressions may be obtained for other components. Assuming $S_L(n)$ to have the shape equivalent to an exponential correlation coefficient, the above equation is plotted as a function of T/t_L in Figure 2.2. The area under each curve for a particular value of $T'=T/t_L$ is a measure of the contribution of the energy spectrum to the mean square displacement. Observe how the contribution of the high frequency range is effectively cut off and how for large values of T' the only contribution is from the low frequency end of the spectrum.

Relationship between Lagrangian and Eulerian quantities

All of the above discussion pertains to Lagrangian quantities. Unfortunately they are very difficult to measure. It is very important to find relationships between these and Eulerian quantities which can be measured without much difficulty.

Mickelsen (45) found from wind tunnel experiments:

$$\int_0^{x_2} \int_0^{x_1} R_{u_i u_i}(x) dx dx_1 = \overline{v^2} \int_0^{\xi_2} \int_0^{\xi_1} R_{u_i u_i}(\xi) d\xi d\xi_1 \quad (2.103)$$

where :

$$\xi = \frac{x}{B (\bar{v}^2)^{1/2}} \quad (2.104)$$

The implied relation is

$$R_{u_i u_i}(x) = \frac{1}{B^2} R_{u_i u_i}(\xi) \quad (2.105)$$

where $B \approx 0.65$. It is observed that the $R_{u_i u_i}(\xi)$ approaches zero much more slowly than the corresponding $R_{u_i u_i}(x)$.

The following hypothesis was adopted by Hay and Pasquill (25) from the results of lateral spread experiments in the atmosphere:

$$R(\xi) = R(t) \quad (2.106)$$

where $\xi = \beta t$. A value of $\beta = 4$ was proposed. It can be shown that :

$$n S_L(n) = \beta n S_E(\beta n) \quad (2.107)$$

substituting this in equation (2.101b) :

$$\bar{X}^2 = \bar{v}^2 T^2 \int_0^{\infty} \beta S_E(\beta n) \left[\frac{\sin \pi n T}{\pi n T} \right]^2 dn \quad (2.108a)$$

$$\bar{X}^2 = \bar{v}^2 T^2 \int_0^{\infty} S_E(n) \left[\frac{\sin \pi n T / \beta}{\pi n T / \beta} \right]^2 dn \quad (2.108b)$$

Concerning the variance of the turbulent velocity fluctuation, Tennekes and Lumley (77) analyzed the correspondence between the Lagrangian and Eulerian variances. They concluded that for homogeneous turbulence in incompressible flow: $v_i^2 = u_i^2$.

It is concluded that there is a relationship between the Lagrangian and Eulerian key parameters discussed above, i.e.

correlation coefficient, energy spectrum and variance of the turbulent velocity. The discussion about the Lagrangian quantities also applies to the Eulerian quantities, providing the factor β is taken into consideration.

Effect of Shear

The above discussion applies to homogeneous and stationary turbulence. However, near the ground, there is a region in which the effect of shear has to be considered. Lee and Dukler (39) simulated the effect of shear in turbulent diffusion in a hybrid computer and concluded that the effect of shear is not important at short and long times, but it is important at intermediate times. The atmospheric diffusion of contaminants for intermediate times of travel is of practical interest.

The additional parameter which arises is the cross correlation coefficient defined as :

$$R_{v_1 v_2}(t_1, t_2) = \frac{\overline{v_1(t_1) v_2(t_2)}}{\overline{v_1' v_2'}} \quad (2.109)$$

Lee and Dukler (39) observed that the effect of shear is to inhibit the longitudinal diffusion without affecting the vertical spread.

Similarity Criteria

In the physical simulation of the atmosphere it is very important to study the requirements that have to be fulfilled in order to reproduce atmospheric flows in a wind tunnel.

Several authors have discussed the problem, e.g. Cermak (9) and Snyder (70). The discussion by Snyder is very complete and is closely followed in this section.

Two flows are similar if they satisfy identical non-dimensional differential equations and non-dimensional boundary conditions. The basic approximate equations describing the atmospheric flow field have already been derived, i.e. equations (2.7), (2.8) and (2.9). Dimensionless variables can be defined by using the reference quantities: L_R , length; U_R , velocity; ρ_R , density; θ_R , temperature; and Ω_R , angular velocity. The dimensionless variables, denoted by a prime are:

$$\begin{aligned} \chi_i' &= x_i/L_R, \quad u_i' = U_i/U_R, \quad t' = U_R t/L_R, \quad \rho' = \rho/\rho_R \\ \tilde{P}' &= \tilde{P}/\rho_R U_R^2, \quad \theta' = \theta/\theta_R, \quad \Omega_j' = \Omega_j/\Omega \end{aligned}$$

Substitution of these quantities into equations (2.7), (2.8) and (2.9) yields the non-dimensional governing equations:

$$\begin{aligned} \frac{\partial u_i'}{\partial t'} + u_j' \frac{\partial u_i'}{\partial x_j'} + \frac{2}{Ro} \varepsilon_{ijk} u_k' \Omega_j' &= -\frac{1}{\rho'} \frac{\partial \tilde{P}'}{\partial x_i'} + \\ &\frac{1}{Fr^2} \theta' \delta_{3i} + \frac{1}{Re} \frac{\partial^2 u_i'}{\partial x_j' \partial x_j'} \end{aligned} \quad (2.110)$$

$$\frac{\partial u_i'}{\partial x_i'} = 0 \quad (2.111)$$

$$\frac{\partial \theta'}{\partial t'} + u_i' \frac{\partial \theta'}{\partial x_i'} = \frac{1}{Pe} \frac{\partial^2 \theta'}{\partial x_i' \partial x_i'} \quad (2.112)$$

Where :

$Ro = U_R / L_R \Omega_R$; Rossby Number
$Fr = U_R / (g L_R \theta_R / T_0)^{1/2}$; Froude Number

$$\begin{aligned} Re &= U_R L_R / \nu && ; \text{Reynolds Number} \\ Pe &= U_R L_R / \alpha && ; \text{Peclet Number} \\ \alpha &= k / \rho C_p && ; \text{Thermal diffusivity} \end{aligned}$$

Solutions of this set of equations will be identical if and only if the coefficients: $Ro, Fr, Re,$ and Pe and the non-dimensional boundary conditions are identical.

In the study of diffusion problems, an additional parameter arises from the nondimensionalization of the equation for molecular diffusion:

$$\frac{\partial C}{\partial t} + u_i \frac{\partial C}{\partial x_i} = D \frac{\partial^2 C}{\partial x_i \partial x_i} \quad (2.113)$$

Where C is the instantaneous concentration and D is the molecular mass diffusivity. Using as before a reference quantity to get a dimensionless variable. i.e. $C' = C/C_R$, the non-dimensional equation of molecular diffusion is obtained :

$$\frac{\partial C'}{\partial t'} + u_i' \frac{\partial C'}{\partial x_i'} = \frac{1}{Re Sc} \frac{\partial^2 C'}{\partial x_i' \partial x_i'} \quad (2.114)$$

where: $Sc = \nu / D$; Schmidt Number

In what follows, these dimensionless parameters are studied in more detail.

The Rossby number is a ratio of advective or local accelerations to Coriolis accelerations. Since Ω_R is constant, the important quantity which determines the value of Ro is L_R . When $Ro \gg 1$ Coriolis acceleration is neglected; however, for large values of L_R it becomes important. Pasquill (53) concludes

that when it is desired to simulate diffusion in a prototype whose length scale L_R is greater than around 5 km in relatively flat terrain, the Ro number criterion should be considered.

The Reynolds number is the ratio of the inertial to the viscous forces. Reynolds number equality is impossible to meet in practice because of the scale reduction. In this situation, the concept of Re number independence proves to be very useful. According to Townsend (81), "geometrically similar flows are similar at sufficiently high Re number". Golden (21) found that for a model composed of cubes, a sufficiently high Re was 11000. Smith (66) found that it was $2 \times 10^4 - 2 \times 10^5$ for sharp edged buildings. This minimum value is expected to increase as the model is more streamlined.

The effect of not matching the Re number results in a wind tunnel energy spectrum having a narrower range of frequencies than the actual one. However, the frequency range cut-off is in the high frequency range as shown by experiments and as was demonstrated earlier this range is not as important as the low frequency range.

The Peclet number can be written :

$$Pe = U_R L_R / \alpha = (U_R L_R / \nu) (\nu / \alpha) = Re \cdot Pr$$

where: $Pr = \nu / \alpha$: Prandtl number

The Reynolds-Schmidt product may be written analogously:

$$U_R L_R / D = (U_R L_R / \nu) (\nu / D) = Re \cdot Sc$$

Observe that these parameters are of the same form. When air

is used for modelling the atmosphere, the Pe and Re-Sc product may be neglected as modelling criteria if the flow exhibits Re number independence.

The Froude number represents the ratio of inertial to buoyancy forces. Batchelor (4) showed how this parameter is related to the Richardson number (Ri). The Fr number can be written :

$$Fr^2 = \frac{T_0}{g} \frac{U_R^2}{L_R^2} \frac{L_R}{\theta_R}$$

In the absence of a clearly defined reference length in the atmosphere it is possible to substitute:

$$\frac{U_R^2}{L^2} = \left(\frac{\partial \bar{u}}{\partial z} \right)_R^2 ; \frac{\theta_R}{L_R} = \left(\frac{\partial \theta}{\partial z} \right)_R$$

so:

$$Fr^2 = \frac{T_0}{g} \frac{\left(\frac{\partial \bar{u}}{\partial z} \right)_R^2}{\left(\frac{\partial \theta}{\partial z} \right)_R} = \frac{1}{Ri} \quad (2.115)$$

In principle, neither the Fr or the Ri numbers are difficult to duplicate. This is the most important criterion to be matched when simulating atmospheric diffusion.

Boundary Conditions.-Snyder (70) concludes that this item is no well determined. However, he states that it is adequate to reproduce properties characteristic of the ensemble of realizations of boundary conditions, i.e. specification of all statistical properties (all of the moments of the velocity, temperature, pressure and density fields) both initially everywhere and on the boundaries at all times. One important boundary is

that between the region studied and the approach flow coming from upstream. In practice, only the first few moments are supplied at the present time, at least the mean and the variance; however it is plausible from physical experience that such specification is sufficient. Armit and Counihan (2) submitted, giving qualitative arguments, that in addition to the mean and the variance, it is also necessary to reproduce the energy spectrum in the approach flow. The specification that the velocity must be zero at solid boundaries require geometric similarity between model and prototype. However, details smaller than z_0 need not be reproduced, Jensen (32) .

The no slip condition at solid boundaries is a viscous constraint. The flow field very close to a boundary is not Re number independent. On the other hand, flows over aerodynamically rough surfaces are Re number independent. An aerodynamically rough surface is one in which the roughness height is greater than the viscous sublayer height. According to Sutton (73), the criterion that ensures the flow to be aerodynamically rough is

$$u_* z_0 / \nu \geq 2.5 \quad (2.116)$$

It is known from experiments that the atmospheric flow is aerodynamically rough. Over-roughening of the model surfaces may be necessary to meet the above criteria.

Specification of boundary conditions on concentration distribution depends on the type of problem studied, e.g. for a single source, $C'=0$ at $t'=0$ and $C'=\text{const.}$ for all times.

The model scale must be in accordance to the ratio of atmospheric and wind tunnel boundary layers' height.

CHAPTER III

ATMOSPHERIC BOUNDARY LAYER DESCRIPTION

In this chapter the experimental data on the behavior of the atmospheric boundary layer are reviewed. In the atmospheric boundary layer (ABL) the wind changes direction and magnitude frequently. Due to the large length scale, its typical Reynolds number is very large and it assumes a new equilibrium quickly after a change in direction happens. These phenomena, wind direction and magnitude change, make difficult ABL experimental measurements, which are usually done on periods in which stationarity may be assumed.

Several review papers on the "neutral atmosphere" characteristics are available in the literature, e.g. Counihan (17) and Teunissen (78). Since the aim of the present work is to simulate various stabilities, a review of the available literature on various key parameters, e.g. turbulence intensities, energy spectrum, length scales, etc., as a function of stability is given in this section.

Boundary and Surface Layers' Heights

The height of the boundary layer " δ " is a function of the type of terrain. It is assumed, in this work, that the values given by Davenport (19) and reproduced in the Figure 3.1 are applicable, i.e. :

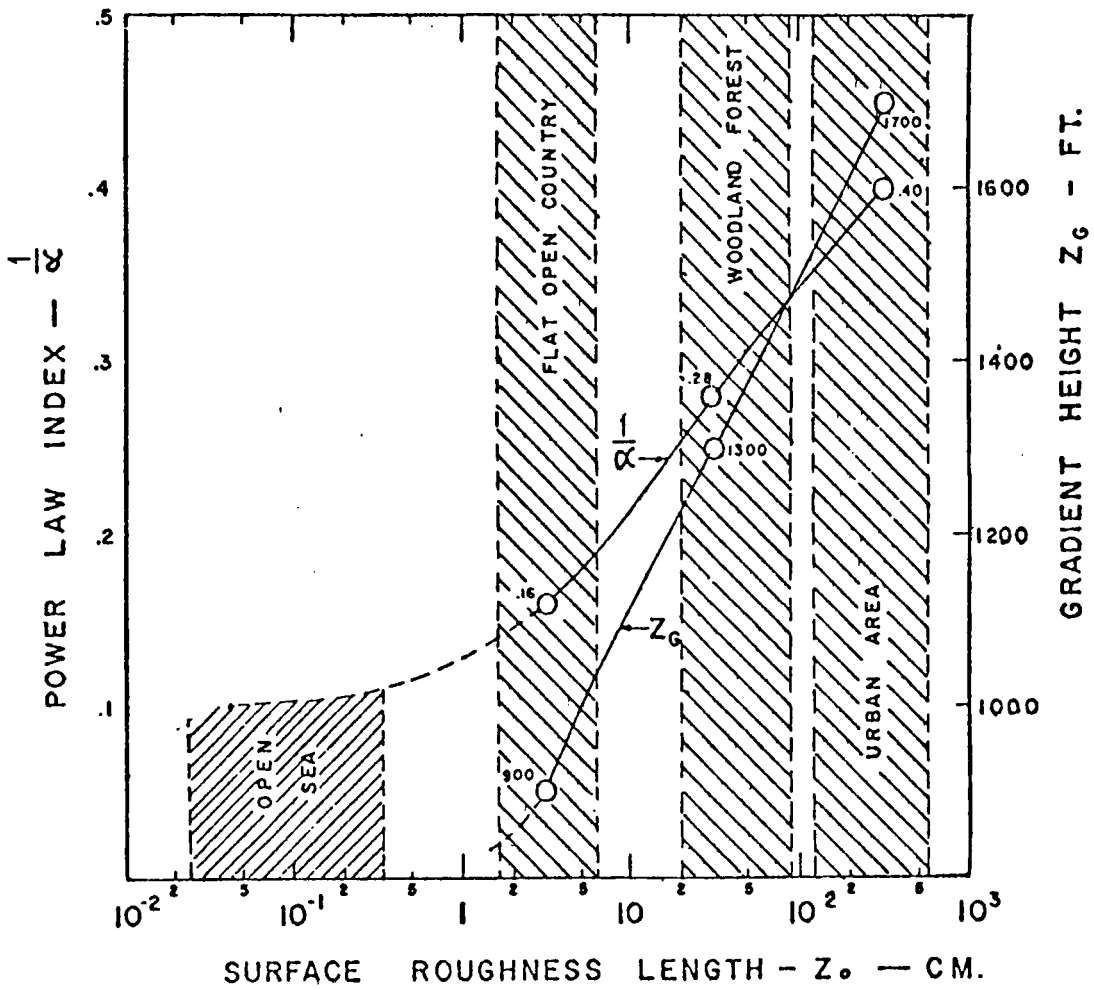


Figure 3.1.-Boundary layer height and Power Law Index . Neutral A B L .

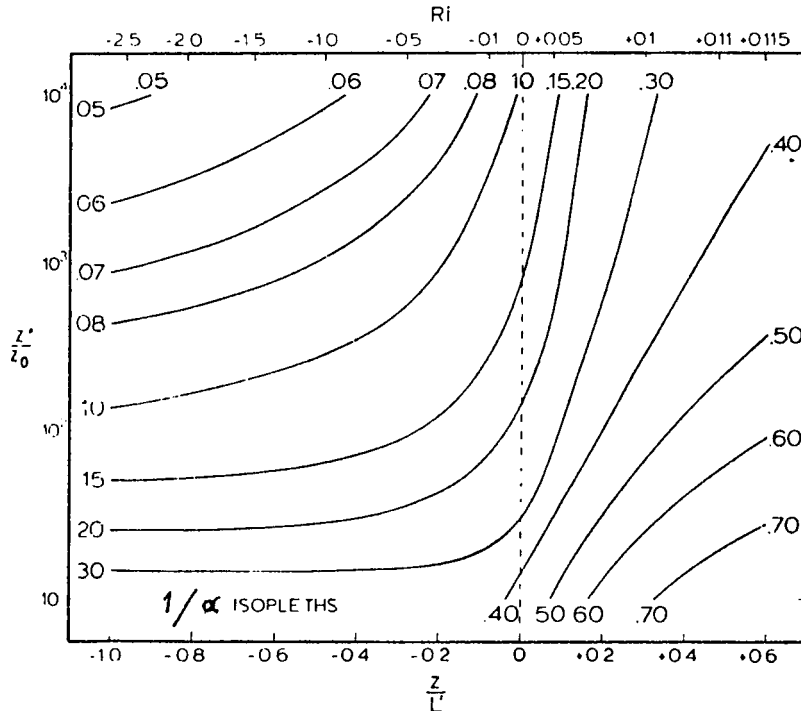


Figure 3.2.-Power law index as a function of stability.

rural terrain	$\delta = 275 \text{ m}$
urban terrain	$\delta = 520 \text{ m}$

Counihan (17) gives a value of approx. 600 m both for rural and urban terrain, which seems too high.

The surface layer is the region in which the shear stress is constant, its height is in the range of 30 to 100 m, Teunissen (78). Counihan (17) reports that the surface layer is approx. 100 m in height.

Mean Velocity Profile

As has been discussed before, the logarithmic velocity profile is expressed as a function of stability and roughness length. Equation (2.34b) applies for neutral stability. It will be slightly modified to account for the zero plane displacement (d). The zero plane displacement is that height above the roughness bottom at which the velocity falls to zero. Equation (2.34b) becomes:

$$\frac{\bar{u}}{u_*} = \frac{1}{k} \ln \frac{z-d}{z_0} \quad (3.1)$$

Another form to represent the mean velocity profile is a power law:

$$\frac{\bar{u}(z)}{\bar{u}(z_1)} = \left(\frac{z}{z_1} \right)^{1/\alpha} \quad (3.2)$$

The exponent $1/\alpha$ is a function of the type of terrain (z_0) and atmospheric stability (z/L). Values of $1/\alpha$ are given in Figure 3.2, according to Panofsky and Prasad (52). Counihan gives

the values of the exponent $1/\alpha$ as in equation (3.2) for neutral stability:

rural terrain	$1/\alpha = .143 - .167$
suburban terrain	$1/\alpha = .21 - .23$
urban terrain	$1/\alpha = .28$

Figure 3.1 also shows the Power Law index as a function of type of terrain (z_0) for neutral stability.

Roughness Length

The roughness length characterizes the terrain surface.

Counihan (17) gives for neutral stability:

rural	$.01 \leq z_0 \text{ (m)} \leq .15$
suburban	$z_0 \cong 1 \text{ m}$
urban	$z_0 \cong 2 - 3 \text{ m}$

z_0 is an important parameter for the application of the "Similarity Theory" (Cermak (7)).

Reynolds Stresses (\overline{uw})

The turbulent stress, \overline{uw} , is a measure of momentum flux. The product \overline{uw} is a function of height, surface roughness and of stability. Counihan (17) gives for a neutral atmosphere:

$$0.002 \leq -\overline{uw}/U_0^2 \leq 0.0025 \text{ for rural terrain and sea.}$$

Pasquill (54) submitted that the \overline{uw} product actually increases with roughness length:

$$\frac{\text{urban } \overline{uw}}{\text{rural } \overline{uw}} = 1.46 - 1.56 \text{ near ground level}$$

where for urban terrain $z_0 = 2.5 \text{ m}$ and for rural terrain, $z_0 = 0.1 \text{ m}$.

Haugen ,et al. (24) studied the momentum and heat fluxes in the surface layer and found for near neutral and stable conditions at a height of 22.6 m on a flat rural terrain:

$$\overline{uw} / u' w' = 0.3$$

decreasing to a value of approx. 0.1 for very unstable conditions ($Ri = - 2.0$ equivalent to an "A" Pasquill-Gifford stability) . He also found the momentum and heat fluxes to be constant within $\pm 20 \%$ in the lowest 20 meters of the A B L .

Friction Velocity , u_*

According to the similarity theory and experimental values of $\phi(z/L)$, Pasquill (56) proposed:

$$u_* \text{ unstable} > u_* \text{ neutral}$$

The ratio $u_*(\text{stable})/u_*(\text{neutral})$, has not been analyzed due to the sparcity of $\phi(z/L)$ data, but it is proposed by Pasquill (56) that :

$$u_* \text{ stable} < u_* \text{ neutral}$$

The same reference states that u_* increases with roughness length.

Turbulence intensities

The turbulence intensities particularly the vertical and lateral, are the most important parameters affecting the diffusion of contaminants. Table 3.1 shows the vertical and lateral turbulence intensities as a function of stability in the surface layer. Table 3.2 shows the longitudinal turbulence intensities for neutral stability.

TABLE 3.1

VERTICAL AND LATERAL TURBULENCE INTENSITIES

AS A FUNCTION OF ATMOSPHERIC STABILITY IN THE SURFACE LAYER

Atmospheric Stability	w'/u_*	w'/\bar{U}	v'/u_*	v'/\bar{U}	Ref. Meas. at (m)
Very Unstable [A]	- - -	$>.28$	- - -	$.24-.45$	65
	- - -	$(.25)$	- - -	$(.17)$	41 92
	- - -	$\langle .17-.30 \rangle$	- - -	$\langle .032-.24 \rangle$	68 16
	- - -	- - -	- - -	$>.17$	68 16
Unstable [B]	2.3	- - -	3.65	- - -	30
	up to 3	- - -	- - -	- - -	56 100
	- - -	$(.21)$	- - -	$(.14)$	41 92
	- - -	$\langle .10-.264 \rangle$	- - -	$\langle .032-.24 \rangle$	67 150-500
	- - -	$.22-.29$	- - -	- - -	68 16
Slightly Unstable [C]	2.2	- - -	3.43	- - -	30
	- - -	$(.14)$	- - -	$(.12)$	41 92
	- - -	$\langle .013-.23 \rangle$	- - -	$\langle .015-.2 \rangle$	65
	- - -	$.16-.28$	- - -	$.14-.24$	67 150-500
	- - -	$.11-.22$	- - -	- - -	68 16
Neutral [D]	1.25	- - -	2.0	- - -	56 100
	1.6	- - -	2.5	- - -	30
	1.3	- - -	- - -	- - -	78
	1.27	- - -	- - -	- - -	82
	1.2-1.3	- - -	- - -	- - -	24
	- - -	$.05-.10$ (rural)	- - -	- - -	17
	- - -	$.1-.17$ (urban)	- - -	- - -	17

Table 3.1 (continued)

Atmospheric Stability	w'/u_*	w'/\bar{U}	v'/u_*	v'/\bar{U}	Ref.	Meas. at (m)
Neutral [D]	- - -	(.065) <.017-.23>	- - -	(.067) <.015-.13>	41	92
	- - -	.10-.16	- - -	.10-.14	65	
	- - -	- - -	- - -	≈.10	68	16
	- - -	.06-.11	- - -	- - -	67	150-500
		1.27	- - -	1.6	- - -	30
Slightly Stable [E]	- - -	(.025) <.01-.065>	- - -	(.025) <.006-.064>	41	92
	- - -	.05-.10	- - -	.03-.09	65	
	- - -	.03-.06	- - -	- - -	67	150-500
	- - -	- - -	- - -	≈.09	68	
		1.24	- - -	1.75	- - -	30
Stable [F]	- - -	(.017) <.01-.06>	- - -	(.017) <.005-.042>	41	92
	- - -	<.04	- - -	<.03	65	
	- - -	- - -	- - -	<.08	68	
	- - -	<.03	- - -	- - -	67	150-500

Notes: () = median value ; = 70% of the values
 [] = Pasquill-Gifford Stability

TABLE 3.2
 LONGITUDINAL TURBULENCE INTENSITY
 FOR NEUTRAL STABILITY IN THE SURFACE LAYER

u'/u_*	u'/\bar{U}	Ref.	Remarks
2.58	- - -	30	
2.5	- - -	56	
- - -	.1-.2	17	rural
- - -	.2-.35	17	urban

One should be very careful when using Table 3.1, mainly because of the diversity of terrain types over which the data were obtained, e.g. Haugen, et al. (24), and Izumi (30) are from the same set of data (taken on the same site) corresponding to a flat rural terrain. Luna and Church data (41) were taken on rural but hilly terrain. Smith and Abbot (68) were obtained for open grassland, while Weber (82) more precisely, determined $z_0 = 0.08$ and 0.36 m, depending upon wind direction. The other cited references, Counihan (17), Pasquill (56), Slade (65), and Teunissen (78) are reviews for several sites but can be considered representative of rural terrain, unless otherwise specified.

The Tables 3.1 and 3.2 were done by reproducing the values reported by the references. Where the reported values were given as plots as a function of height and wind speed, e.g. references (65), (67) and (68), average values were taken for heights up to the height of the surface layer (30 to 100 m) and for moderate wind speeds.

It is very important to study the behavior of the turbulence intensities with height. The following conclusions were submitted by Slade (65). The lateral turbulence variance does not change appreciably with height under any stability condition. The vertical turbulence variance is constant with height under neutral conditions. In a stable atmosphere it decreases with height, but under unstable conditions increases markedly

with height. The longitudinal turbulence variance is independent of height under neutral and unstable conditions but decreases with height under stable conditions.

Energy Spectra

The importance of the energy spectrum arises from the necessity of matching boundary conditions with the approach flow as discussed in the last chapter. It is also important because it reflects the effect of stability in a quantitative way as will be discussed shortly. A large number of equations have been proposed to represent the energy spectrum, e.g. Busch and Panofsky (5), Lumley and Panofsky (40), and Kaimal, et al. (35). In the present work, the semi-empirical formulae proposed by Kaimal, et al. (35), will be adopted. It is a comprehensive study of the three velocity components as a function of stability; furthermore, other authors more recently have confirmed the validity of Kaimal's data and reported very similar values, e.g. Sharan and Wickerts (64), and Weber, et al. (82).

The approach of Kaimal, was to non-dimensionalize the energy spectrum in such a way that it would collapse to the same equation in the inertial subrange. According to Kolmogorov's law, at high Re numbers there is an inertial subrange where the energy spectrum is determined uniquely by the parameter (dissipation). It may be shown, starting from Kolmogorov's law for the inertial subrange, that:

$$F_{uu}(k_1) = \alpha_1 \epsilon^{2/3} k_1^{-5/3} \quad (3.3)$$

Where α_1 is a constant and $F_{u_i u_i}(k_1)$ is the one dimensional energy spectrum for the "u" component as a function of wave number in the main flow direction, k_1 . Further manipulation and substitution of $k_1 = 2\pi n/U$ (assuming Taylor's hypothesis) result in:

$$\frac{k_1 F_{u_i u_i}(k_1)}{u_*^2} = \frac{n S_{u_i u_i}(n)}{u_*^2} = \frac{\alpha_1}{(2\pi k)^{2/3}} \Phi_\varepsilon^{2/3} f^{-2/3} \quad (3.4)$$

where Φ_ε is the dimensionless dissipation rate:

$$\Phi_\varepsilon = k z \varepsilon / u_*^3 \quad (3.5)$$

$$f = n z / \bar{u} \quad (3.6)$$

Note that k is the von Karman constant. Dividing equation (3.4) by $\Phi_\varepsilon^{2/3}$, the dependency on (z/L) is eliminated:

$$\frac{n S_{u_i u_i}(n)}{u_*^2 \Phi_\varepsilon^{2/3}} = \frac{\alpha_1}{(2\pi k)^{2/3}} f^{-2/3} \quad (3.7)$$

Similar equations may be written for the energy spectrum in the inertial subrange for the vertical and lateral components, $S_{ww}(n)$ and $S_{vv}(n)$ respectively. It was found that the energy spectra converges to equation (3.7) irrespective of stability.

Figures 3.3, 3.4, and 3.5 show the $S_{ww}(n)$, $S_{uu}(n)$ and $S_{vv}(n)$ as a function of stability (z/L) , measured at three levels: 5.66, 11.3 and 22.6 m on rural terrain. Observe how the unstable spectrum is characterized by the increase of energy in the low frequency range. However, the dependency on (z/L) is not well organized in the $S_{ww}(n)$ spectrum except for slightly unstable conditions $(z/L < 0)$. Observe also an excluded region in the

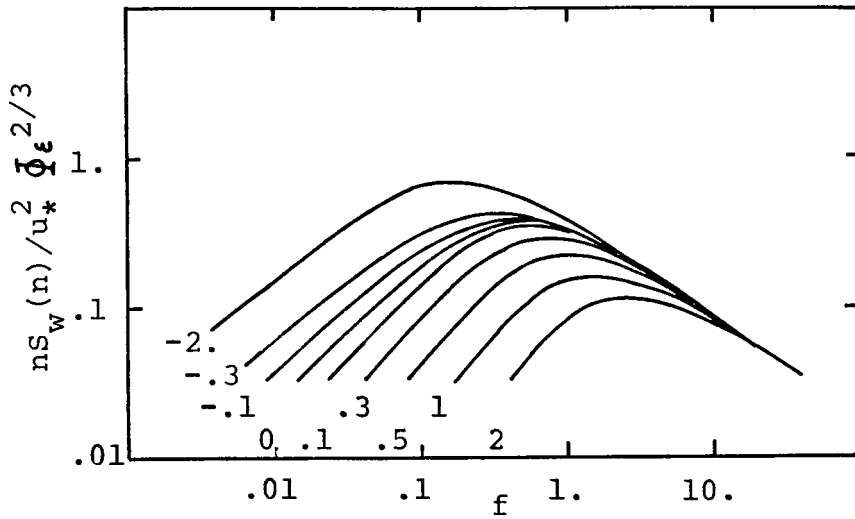


Figure 3.3.-Generalized w spectrum.

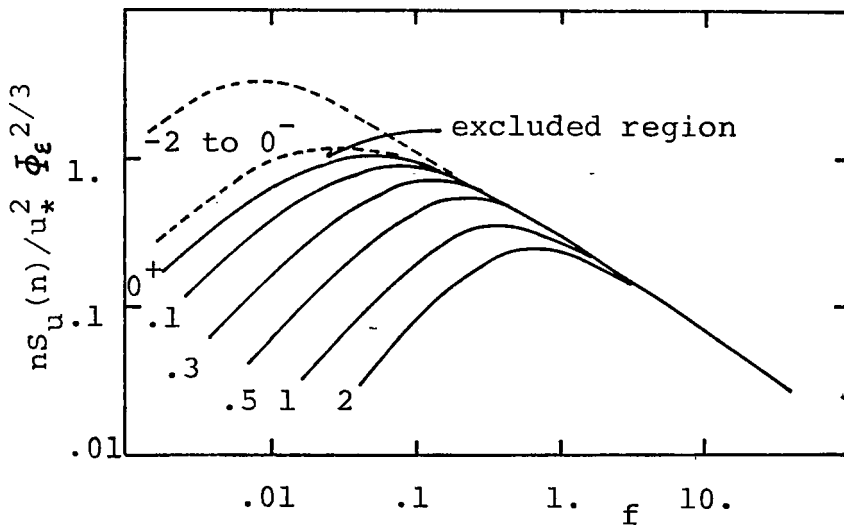


Figure 3.4.-Generalized u spectrum.

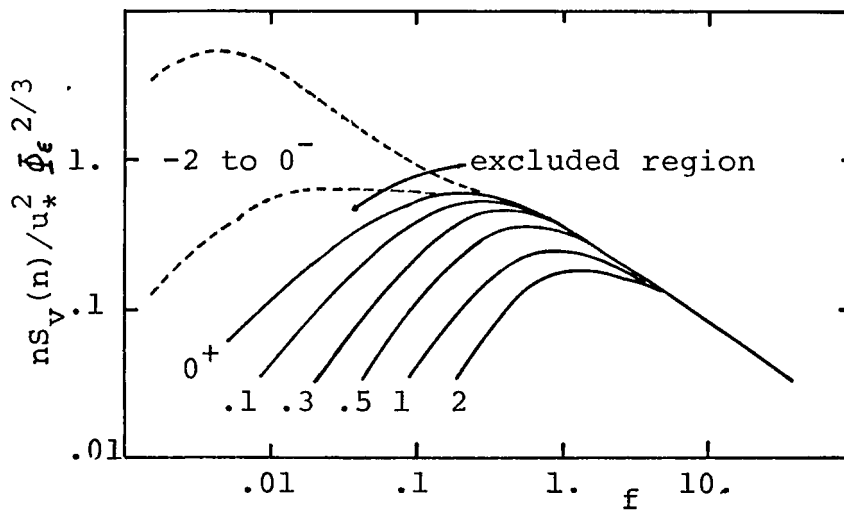


Figure 3.5.-Generalized v spectrum.

$S_{uu}(n)$ and $S_{vv}(n)$ spectrum were no data were found. These features were confirmed by Sharan and Wickerts (64) and Weber, et al. (82). The dependency on z/L of the three energy spectra is well organized for stable conditions ($z/L > 0$). Note that the peak of the energy spectra moves toward higher frequencies with increasing stability.

For the neutral atmosphere ($\Phi_E = 1$) Kaimal, et al. (35) proposed the following empirical formulae:

$$\frac{n S_{uu}(n)}{u_*^2} = \frac{105 f}{(1 + 33 f)^{5/3}} ; f_{\max} = 0.07 \quad (3.8)$$

$$\frac{n S_{vv}(n)}{u_*^2} = \frac{17 f}{(1 + 9.5 f)^{5/3}} ; f_{\max} = 0.25 \quad (3.9)$$

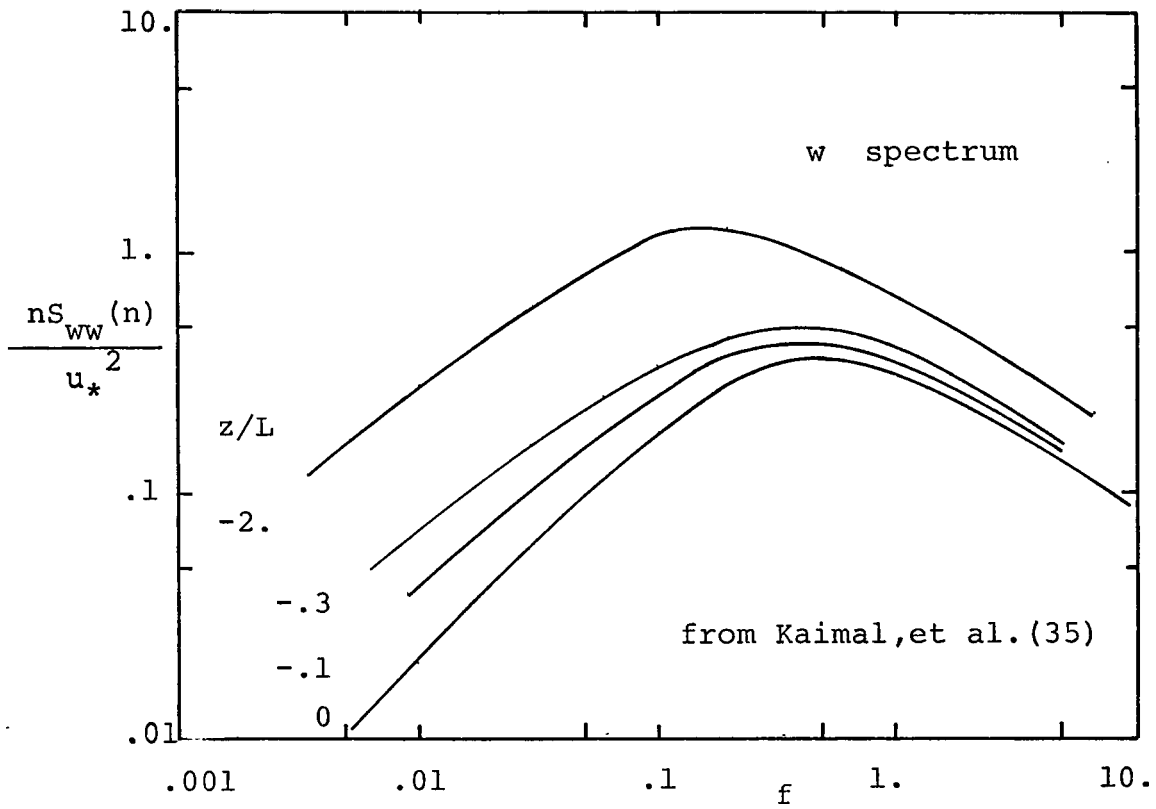
$$\frac{n S_{ww}(n)}{u_*^2} = \frac{2 f}{1 + 5.3 f}^{2/3} ; f_{\max} = 0.60 \quad (3.10)$$

where f_{\max} is the value of "f" corresponding to the maximum value of the function $n S(n)/u_*^2$. The following interpolation formulae is given for the factor Φ_E by the same reference:

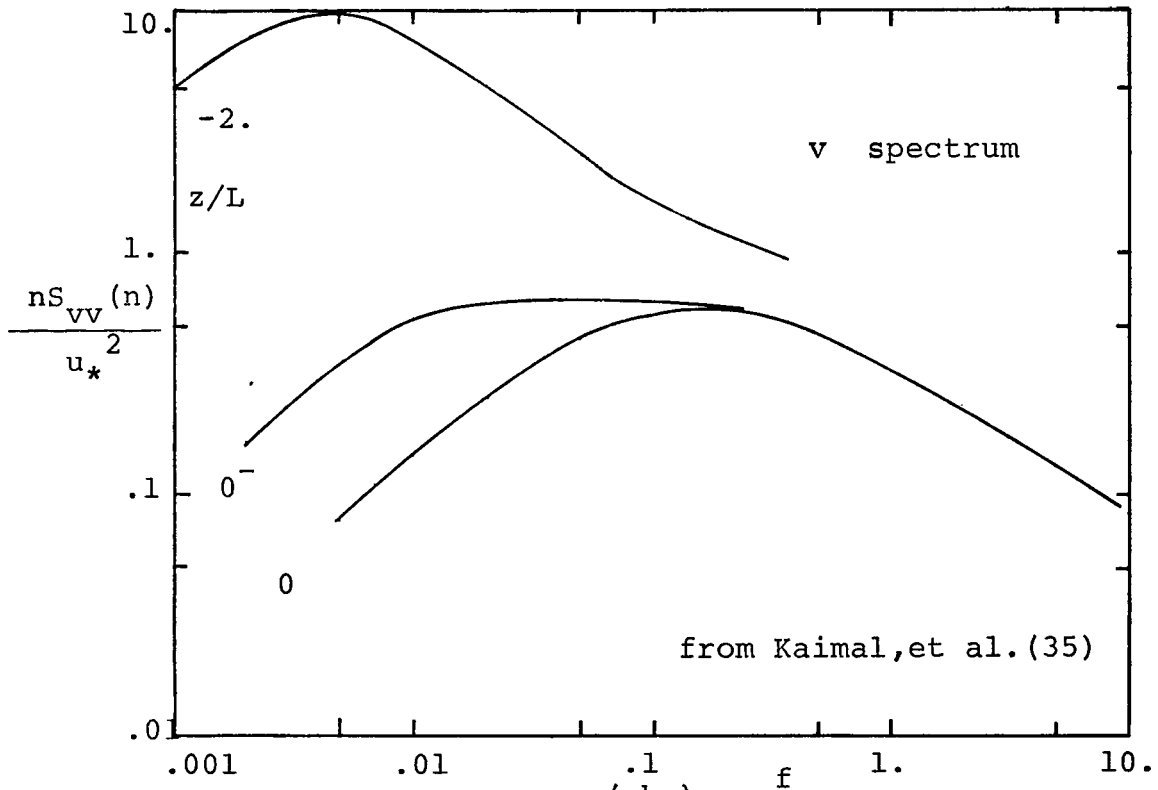
$$\Phi_E^{2/3} = 1 + 0.5 |z/L|^{2/3} ; -2. \leq z/L \leq 0. \quad (3.11a)$$

$$\Phi_E^{2/3} = 1 + 2.5 |z/L|^{3/5} ; 0 \leq z/L \leq 2. \quad (3.11b)$$

These two formula were used to regenerate $n S(n)/u_*^2$ values from values of $n S(n)/u_*^2 \Phi_E^{2/3}$ obtained from Figures 3.3, 3.4, and 3.5. The results are plotted in Figures 3.6 (a and b) and 3.7 (a and b). These plots will be referenced to later in order



(a)



(b)

Figure 3.6.-Unstable Energy Spectrum.

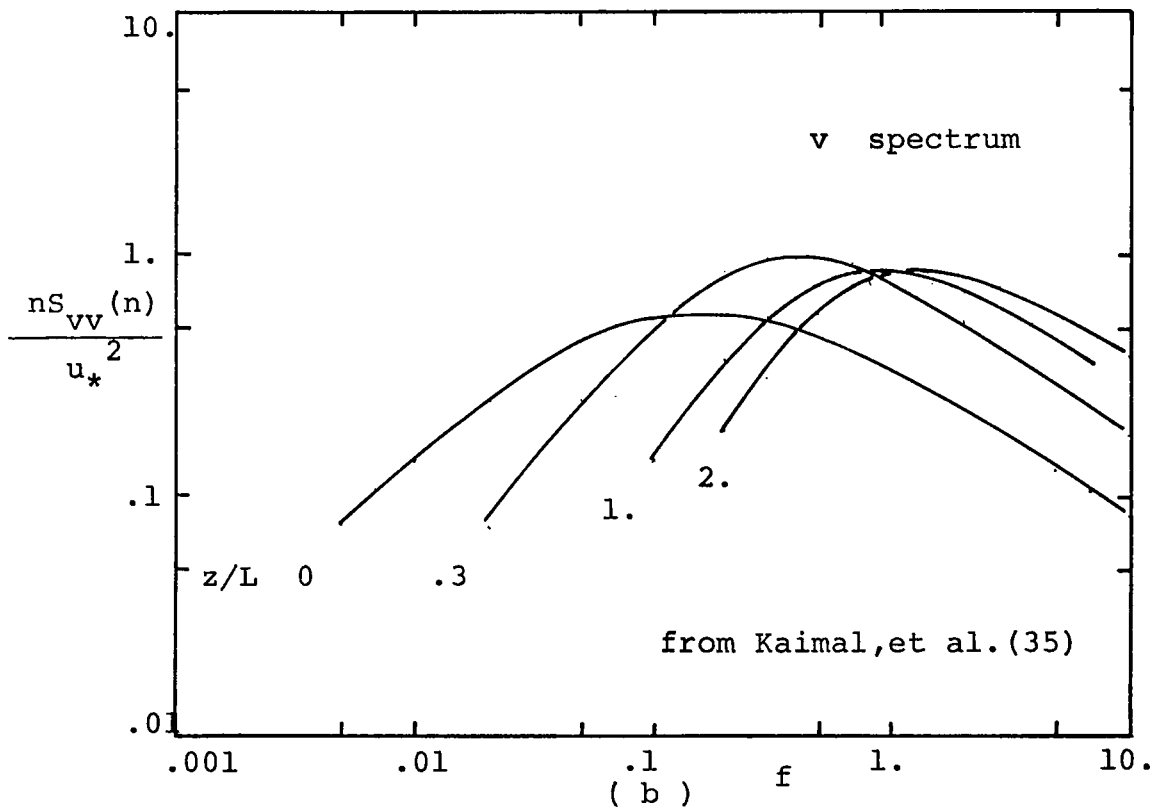
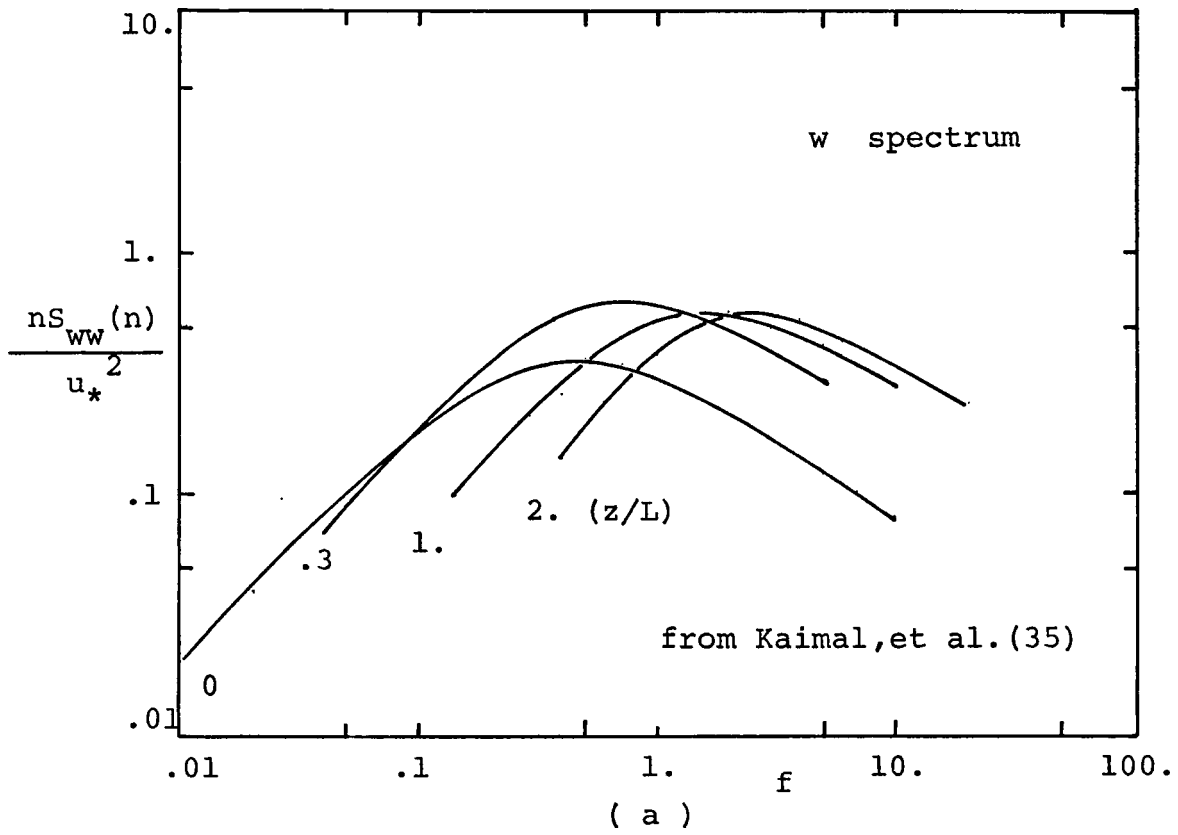


Figure 3.7.-Stable Energy Spectrum.

to compare the wind tunnel results since dissipation was not measured in the present work. In these Figures observe how f_{\max} moves towards lower frequencies with increasing instability and how it moves towards higher frequencies for increasing stability with respect to f_{\max} for neutral stability.

Length Scales

According to the statistical approach, the integral length scales are second in importance only to the variance; however, and unfortunately, there is not agreement between the various reports about their value in the A B L in the literature. All that can be done, at the present time, is to make broad generalizations. The magnitude of the length scales is a function of height, type of terrain and stability. Most of the available information is for the Vertical Length Scale, $L_{w,x}$. Vertical Length Scale.-Pasquill (56), presents a review and concludes:

- a) In neutral conditions:

$$L_{w,x} = 0.5 z \rightarrow 2z$$

in the lowest 20 meters.

- b) Variation with stability:

$$L_{w,x}(\text{unstable}) > L_{w,x}(\text{neutral}) > L_{w,x}(\text{stable})$$

Teunissen (78) review gives:

$$L_{w,x} = 0.4 z \quad ; \quad z < 300 \text{ m}$$

for flat terrain and neutral stability. Taylor, et al. (76) from aircraft measurements submitted:

$$L_{w,x} \cong z^{1/2} \quad ; \quad z < 200 \text{ m}$$

He found the same variation with height for neutral and unstable conditions and that values at the same height are larger for unstable than for stable conditions. Weber (82) by analysis of energy spectrum gave support to Pasquill (56) conclusion concerning the variation with stability. Lumley and Panofsky (40) proposed that $L_{w,x}$ increased with height up to about 100 to 200 meters and then remained constant. Kaimal and Haugen (34) proposed something similar, $L_{w,x}$ either remain constant or decrease with height above approximately $z=200$ m .

Longitudinal Length Scale.- $L_{u,x}$ is not as important as $L_{w,x}$ or $L_{v,x}$ even though it is the greatest. For neutral atmosphere Counihan (17) concluded: $L_{u,x}$ decreases with increase of surface roughness, increases with height up to 200 - 300 meters , and thereafter decreases with further increase of height, becoming independent of surface roughness. Additional analysis can be done by looking at the frequency, n_{max} , at which the energy spectrum plotted as $n S(n)$ vs. $f(nz/\bar{U})$ has a maximum, since the corresponding wave length λ_{max} ($\lambda_{max} = \bar{U}/n_{max}$) is proportional to the $L_{u,x}$ (Pasquill, (55)).

Lateral Length Scale.-Busch, et al. (6), report values of λ_{max} (from the lateral energy spectrum) between 150 to 300 meters for the range of heights 15 - 92 meters ; observing that λ_{max} at 92 meters is similar to the vertical λ_{max} at the same height but the lateral λ_{max} at 15 meters is much higher than the vertical.

Kaimal (33) found from analysis of his spectra (35) that, for stable conditions, the length scale could be represented as a function of Ri number, as shown in Table 3.3 . The equations proposed in Table 3.3 hold up to $z=22.5$ m .

TABLE 3.3

DIMENSIONLESS LENGTH SCALES AS A FUNCTION
OF Ri NUMBER : $0.05 < Ri < 0.2$

Length Scale	i=u	i=v	i=w
$L_{i,x}/z$	$0.082/Ri$	$0.027/Ri$	$0.015/Ri$
λ_{max}/z	$0.52 /Ri$	$0.173/Ri$	$0.093/Ri$

CHAPTER IV
PREVIOUS WORK AND
PRESENT WORK SIMULATION APPROACH

Previous Work

Wind tunnel modelling has received considerable attention during the last ten years as it is a convenient way to study the diffusion of pollutants. A considerable number of papers have been published in the literature dealing with rural and urban modelling under neutral and stratified conditions. Hunt and Fernholz (28) published a review of the methods used by European and U.S.A. institutions up to 1974. An up-to-date literature review is given in this section. Table 4.1 is a summary of the wind tunnel methods to simulate the A B L.

Counihan (2), (14), (15) used a barrier wall, vortex generators and surface roughness to produce a thick boundary layer in a short test section. He was able to reproduce the mean velocity, turbulence intensities and Reynolds stresses characteristic of a neutral rural A B L. He measured the longitudinal energy spectrum and found it to be similar to the field energy spectrum reported by Harris (23). Since the boundary layer is thickened in a short length, the approach flow is not expected to be in equilibrium. From his data, it is observed that indeed the turbulent intensities decay approx. 20 % in a distance -

TABLE 4.1

REVIEW OF ATMOSPHERIC BOUNDARY LAYER SIMULATION

Institution	δ at test point (cm)	Simulated terrain and stability	Reported measurements	References No.
Central Electricity Research Lab.	120	rural	neutral \bar{U}, u', v', w', uw $S_u(n)$	68
	15	rural	neutral \bar{U}, u', v', w', uw $S_u(n)$	14, 15
	15	urban	neutral \bar{U}, u', v', w', uw $S_u(n), S_w(n)$	16
University of Notre Dame	56	rural	neutral $u^2 + v^2, uw$	49
Illinois Institute of Technology	50	rural	neutral $u'/\bar{U}, uw$	48
University of Toronto U.T.I.A.S.	18	rural & urban	neutral \bar{U}, u', v', w', uw $S_u(n), S_v(n)$ $S_w(n)$	79, 80
New York University	18	rural	stratified \bar{U}, u', w', uw Conc.Meas.	51
	20	urban	neutral \bar{U}, u', uw Flow visual. Conc.Meas.	27

Table 4.1 (continued)

Institution	δ at test point (cm)	Simulated terrain and stability	Reported measurements	References No.	
National Inst.for Env.Studies(Japan)	- -	stratified	- - -	50	
Colorado State Univ.	70	rural	stable	\bar{U}, u', w'	3
	90	rural	- - -	\bar{U} , temperature	8
	-	rural	stable	\bar{U} , Conc.Meas.	11
	-	rural	stratified	Flow.Visual. Conc.Meas.	43
	-	urban	stratified	Temp. Flow Visual. Conc.Meas.	63
	-	urban	neutral	\bar{U} , Conc.Meas.	10
Laboratoire de Mecanique des Fluides	20	rural	neutral	\bar{U}, u', v', w', uw $S_u(n), S_w(n)$	61
	-	rural	stratified	\bar{U}, u', w' $S_u(n), S_w(n)$ Conc.Meas.	61
Env.Protection Agency	180	urban	neutral	$\bar{U}, u', \text{Conc.Meas}$	71

Table 4.1 (continued)

Institution	δ at test point (cm)	Simulated terrain and stability	Reported measurements	References No.
University of Bristol	50	urban neutral	\bar{U}, u', v', w' $S_u(n), S_v(n)$ $S_w(n)$	13
University of Ontario	-	rural (hilly) neutral	$S_u(n), \text{Conc. Meas.}$ Flow Visual.	29

equivalent to 1.5 boundary layer heights.

Counihan (16) used the same system described above but with a taller barrier wall to reproduce the neutral urban A B L . His mean velocity and turbulence intensity profiles agree well with field values. He assumed the longitudinal and vertical velocity component energy spectrum to be similar in shape to the rural one. The $S_{uu}(n)$ was compared to the Harris (23) spectrum and found to be similar. The approach flow in this simulation, as for the rural one, is expected to lack of equilibrium.

Nee, et al. (49) , used a "turbulence generating box" composed of opposite adjustable side jets placed upstream of the test section and a roughness surface to produce a thick boundary layer in which the velocity profile is logarithmic. The approach flow is observed to have longitudinal turbulence intensities decaying less than 10 % in a 4 m distance. However, no measurements of the vertical and lateral turbulence intensities and energy spectrum are reported.

Nagib (48) used discrete wall jets upstream from the test section together with a rough surface to produce a thick boundary layer (approx. 50 cm high) . Only mean velocity and longitudinal turbulence intensity profiles were measured and no comparison with field data was done.

Teunissen (79), (80) simulated the neutral rural and the neutral urban A.B.L. in a small wind tunnel in which the air is driven by a grid of adjustable jets. Virtually, any velocity

profile can be reproduced using this method. He also used a barrier and surface roughness to produce a flow of power law exponent 0.16 typical of flat rural terrain. All turbulence intensities and the uw product were compared to his review of the A B L characteristics (78) and found to be in agreement. The energy spectra, $S_{uu}(n)$, $S_{ww}(n)$, $S_{vv}(n)$, were compared to von Karman spectra for isotropic turbulence and found to agree well. Length scales were also measured and found in good agreement with his review. With a similar set up but with larger roughness elements than for the rural simulation, he obtained a flow field having a power law exponent of 0.35, typical of an urban terrain. The longitudinal turbulence intensities were typical of urban terrain. His longitudinal velocity component energy spectrum agrees with the von Karman spectrum, too. Teunissen submitted that with a grid of adjustable jets, it would be easy to create different temperature profiles for stratified flow studies.

Ogawa, Griffiths and Hoydysh (51) tried to reproduce the stratified A B L by heating or cooling the wind tunnel floor and the air. Neutral, unstable, stable and an elevated inversion were created. Measurements of wind velocity, mean temperature, longitudinal and vertical turbulence intensities and Reynolds stresses were reported, but no comparison with field data was done. They also studied a ground level source. Their results were compared with the Pasquill curves (see Seinfeld (62)),

Sec.6.4.2) and found to be shifted towards more stable categories. This effect was explained as a lack of mesoscale turbulence in the wind tunnel.

Ogawa, et al. (27), also studied urban modelling for a neutral A B L . They used blocks 5x5x5 cm and 5x10x5 cm to simulate the urban geometry. They sought to have equilibrium flow at the point of measurement. A critical Re number based on block height and a minimum distance of 20 block heights covered by blocks upstream the measurement point were found appropriate. Mean velocity profile, longitudinal turbulence intensities, Reynolds stresses were measured, and in addition concentration measurements and flow visualization experiments from an area source were carried out. None were compared to field data.

Ogawa, et al., proposed that since the turbulence characteristics inside the model will be affected strongly by the model geometry, an exact reproduction of the characteristics of the approach flow is not necessary.

Ogawa (50) described a large wind tunnel capable of reproducing any desired stratification by heating or cooling the floor and the ambient air and a temperature profile generator consisting of horizontal rods perpendicular to the mean flow which can be heated at will. However, there is still no work reported in the literature which has been performed in this wind tunnel.

The group of Colorado State University has two large wind

tunnels. In the "Environmental Wind Tunnel" only the neutral A B L. may be simulated, while in the "Meteorological Wind Tunnel", stratification can be simulated for flows having a Ri number between -0.5 to 0.5 by heating or cooling the floor and the ambient air, e.g. Cermak (8) .

Cermak, et al. (10) simulated the neutral urban A B L with an idealized city composed of uniform blocks. Concentration measurements and flow visualization were done from a line source. No comparison with field values was done.

In the Meteorological Wind Tunnel, Plate and Lin (59) studied the stratified rural A B L , using a rough surface in addition to the heated or cooled floor. They found that the mean velocity and temperature distributions are represented very well by the similarity theory.

Arya and Plate (3) studied the stable rural A B L . Stabilities from near neutral to moderately stable were produced and investigated. The turbulence intensities in the longitudinal and vertical directions were compared to the A B L field data and found to agree fairly well.

Chaudry and Meroney (11) did a similar study as above. They also found the velocity profile to obey the similarity theory. Concentration measurements from a ground level source were done and analyzed by the Lagrangian similarity theory (Cermak (7)), and good agreement was found.

The phenomenon of "fumigation", i.e. the behavior of a

plume when the flow near the floor is unstable but with an elevated inversion, was studied by Meroney, et al. (43) . In this work, vortex generators were used to enhance boundary layer growth. Concentration measurements and flow visualization were done.

Sethuraman and Cermak (63) studied the "heat island effect" i.e. the effect experienced by a plume coming from a rural terrain to a warmer urban terrain. Several stabilities were produced in the approach flow. Visualization studies, mean temperature profiles and mean concentration profiles were measured.

Schon and Mery (60) used injection of air from a porous plate at the beginning of the test section to produce a thick boundary layer without stratification even though the floor of this wind tunnel has the capability to be heated or cooled. They measured velocity profile, turbulence intensities and energy spectra for the longitudinal and vertical velocity components. They compare well with field measurements of the corresponding energy spectra.

Schon, et al. (61) simulated unstable conditions from $z/L = -0.2$ to zero. Measurements of wind velocity, longitudinal and vertical turbulence intensities, Reynolds stresses and correlations of the longitudinal and vertical fluctuating velocity component with the fluctuating temperature were done as a function of stability. Also, concentration measurements from a ground source were performed.

Mery, et al. (44) compared these data to field A B L data. They found the longitudinal and vertical turbulence intensities agreed well with field data. The concentration measurements were compared to reported data by Smith and Singer (69) and with the Lagrangian similarity hypothesis and found to agree well.

Snyder and Lawson (71) used the same set up as Counihan (14) to study the plume from a stack as affected by nearby buildings in order to determine optimum stack height. Flow visualization and concentration measurements were used to this purpose. The mean velocity profile was found to obey a 1/5th power law and the longitudinal turbulence intensity found to be similar to that reported by Harris (23) .

Iziumov, et al. (29) studied the plume behavior from a stack through hilly terrain under neutral stability. Measurements of wind velocity, concentration and longitudinal velocity component energy spectrum are reported. The energy spectrum agree moderately well with Davenport (18) field energy spectra.

Cook (13) developed a flow typical of the lower third of the neutral urban A B L . He used a tall barrier (20 cm) and roughness elements 9 cm in height to produce 50 cm of boundary layer which flow corresponds to 1/3 of the A B L . The flow has a velocity profile of which the power law exponent is 0.28 to 0.33, even though a logarithmic profile fits well, too. It has very high turbulence intensities in agreement with Counihan (17)

The longitudinal energy spectrum is similar to Harris (23) and Davenport (18) . The vertical energy spectrum compares well with Busch and Panofsky (40) . Even the longitudinal length scale is compared with rough boundary layer work.

Present Work Simulation Approach

In Chapter II ,the criteria of similarity between two flows was developed.These concepts together with those described in the rest of Chapter II concerning the fluid mechanics and diffusion aspects of the atmosphere are brought together to form the simulation approach used in this study.

The importance of the concept of Re number independence has already been discussed.Values of the critical Re number - (the minimum value of Re at which the flow is self preserving i.e.in equilibrium) are given later in this section.

The single most important parameter to be matched is the Ri number.The value of this parameter determines the mechanical behavior of the atmosphere as was discussed in Chapter II under the headings of "Atmospheric Stability".On the other hand there is definitely a dependence of statistical parameters,e.g. variance,mean velocity,energy spectrum and length scales on Ri number.These,in turn,are quantities upon which the statistical approach of turbulent diffusion is expressed.Thus,we - have in the statistical approach quantities,a common ground to study the wind tunnel modelling of turbulent diffusion in the

atmosphere.

The objective of this work is to simulate different stabilities by only mechanical means, i.e., the increase or decrease of turbulent energy otherwise produced through buoyancy forces arising from a non adiabatic temperature profile, will be tried by placing proper devices (such as barriers, mesh screens and different floor roughnesses) upstream the model. In doing so, one will have to make concessions in the simulation of certain parameters in order to reproduce others more important to the problem studied. It is already expected that an exact simulation of atmospheric flows, other than adiabatic, consistent with all of the criteria of similarity will not be possible. One has to recognize then which are the key parameters affecting atmospheric diffusion and focus attention on them.

If one considers this problem from a theoretically rigorous point of view, it is realized that in a boundary layer, it would be impossible to produce stabilities other than the neutral without imposing a temperature profile on the boundary layer flow. But one has to bear in mind that by introducing those devices noted above, the regular boundary layer flow is modified in some way. The way this flow is modified will be investigated by measuring the important statistical quantities involved. In order to evaluate the accuracy of the simulation, these quantities will be compared to the corresponding values found in the atmosphere for different stabilities.

The effect of the Coriolis force is to turn the wind with height. This can not be reproduced presently in any wind tunnel, but its effect is negligible in the surface layer (Tennekes and Lumley, (77) Sec.5.3) .The surface layer is that layer in which the shear stress is constant and is typically of the order of 100 meters above ground. So, we will try to reproduce the surface layer only rather than the entire boundary layer. In doing so, one still has to keep the Ro number criteria, i.e. $Ro \gg 1$.

Recall that the statistical approach is rigorously valid for a homogeneous turbulence field. This is true at any height, if two-dimensionality of the flow is assumed for the longitudinal and lateral coordinates. However, this approach can not hold for the vertical coordinate since large velocity gradients are found near the ground. Usually the major point sources of contaminant occur well above ground, e.g. stacks. But eventually the contaminant will reach a point where it will be subject to the effect of shear. According to Lee and Dukler (39), as discussed in Chapter II , the effect of shear is to lower the longitudinal diffusion for intermediate times. The flow at these intermediate times is of interest in the present work. If a wind tunnel simulation at a scale of 1:1000 is assumed, the distance from the source on which the effect of shear is felt is between 50 cm to 4 m . However in a flow in which the longitudinal diffusion is done mainly by convection, as in the atmosphere, this

effect will be considered of secondary importance. In fact for the same reason the longitudinal turbulence intensities will be considered of secondary importance, too.

The similarity theory, on the other hand, handles ground level sources, e.g. automotive emissions, which are also important, so when possible, parameters pertaining to such theory, e.g. roughness length, will be measured and reported. In what follows, the parameters to be reproduced are presented in detail and their relative importance discussed.

The simulation of the approach flow arises from the requirement of duplication of boundary conditions. By having an approach flow which is in equilibrium, one achieves Re number independence in the fluid mechanics sense. The atmospheric flow can be considered to be in equilibrium in this sense, due to the large length scales and therefore Reynolds numbers typically found. The question of whether or not this flow exhibits Re number independence as far as the diffusion of contaminants is concerned can only be answered by experiments. Ogawa, et al. (27) found a critical Re of 3400 based on block height, for those used to simulate urban terrain. Golden (21) used cubes and reported a critical Re of 11000 based on cube size. Smith (66) reported a critical Re between 2×10^4 and 2×10^5 for sharp edged buildings. Snyder (70) suggests that the value of this critical Re depends on model geometry and will increase as the geometry becomes more streamlined.

The vertical and lateral turbulence intensities are the most important parameters to be reproduced according to the statistical approach of turbulent diffusion. The magnitude of turbulence intensities depends on stability and type of terrain (rural or urban) .

As has already been discussed the shape of the energy spectrum, particularly for the vertical and lateral turbulence components, is dependent upon stability conditions. The shape of these energy spectra plotted on similarity coordinates and compared to atmospheric data will be another way to evaluate the stability. In analyzing these spectra, particular attention will be paid to the low frequency end, as it is more important for the problem studied.

The length scales are second in importance only to the turbulence intensities. Unfortunately, many of the reported atmospheric values are of such poor quality that only a qualitative comparison will be made. However, the value of the length scales is related to the shape of the spectrum of energy, e.g. the frequency at which the maximum of the energy spectrum plotted as $n S(n) / u_*^2$ vs. "f" occurs, is related to the length scale. Particular attention will be paid to this point when analyzing energy spectra.

The mean velocity profile has already been considered implicitly in the turbulence intensities. Recall that the turbulence intensities are defined as the ratio of the root mean

square value of the fluctuating component to the mean velocity at the location considered. Matching of the velocity profile is of secondary importance.

The requirement of geometrical similarity also arises from the boundary conditions similarity criteria. Scaling of the model will be done against the ratio of typical boundary layer heights from the atmosphere and wind tunnel flow. It is felt that the scaling should be done from length scales. But these, as noted above, are at the present time poorly evaluated. It is believed that when the approach flow is in equilibrium and correctly reproduced, in addition to having geometrical similarity, model and prototype flows will be similar.

It is the purpose of this work to reproduce rural flows for various stabilities and urban flows for neutral stability. Note that for the simulation of flows over complex geometry, which is one advantage of wind tunnel over other modelling techniques, the approach flow reproduction may be relaxed.

CHAPTER V

DESCRIPTION OF EXPERIMENTAL TECHNIQUE

Measurements of wind velocity and several flow visualization tests were performed in the University of Houston Environmental Wind Tunnel (UHEWT) with the objective of reproducing atmospheric flows in order to produce a physical simulation of atmospheric diffusion. The wind tunnel as well as the techniques used to collect and analyze the data are described in this chapter.

Environmental Wind Tunnel Characteristics

The UHEWT is a large, low speed wind tunnel whose configuration and overall dimension are shown in Figure 5.1 . The details of its construction and structural characteristics are given by Wilson (83) .

In this work only the improvements that have been made since Wilson's work are discussed in detail. Table 5.1 shows its main characteristics. The reported working section length is measured starting at 1.2 m from the end of the contraction i.e. where the particular rough or smooth flooring begins. The vortex generating devices were put between the end of the contraction and the beginning of the particular flooring. Three kinds of flooring were used :

- 1) Smooth : 1/4 inch hardboard is used to cover the entire working and test sections.

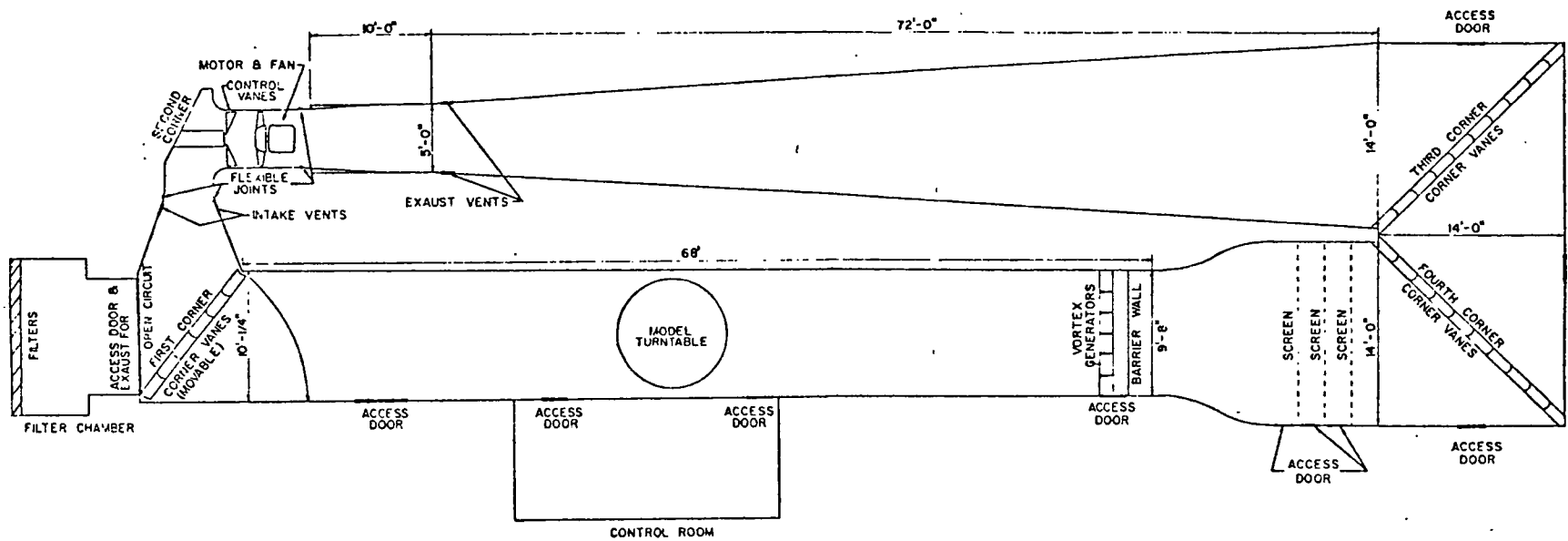


Figure 5.1.- Plan View of Environmental Wind Tunnel .

TABLE 5.1

ENVIRONMENTAL WIND TUNNEL MAIN CHARACTERISTICS

Working Section.-

Length : 8.53 m
Height : $1.4 \pm .15$ m
(at downstream end)
Width : 2.8 - 3 m

Test Section.-

Length : 9.0 m
Height : $1.4 \pm .15$ m
(at downstream end)
Width : 2.8 - 3 m

Contraction Ratio : 4.5 to 1 .

Range of Velocity .-

fan at low speed : 0.6 to 6 m/s
fan at fast speed: 4 to 10 m/s

Pressure Gradient.-

$\Delta P/2.5$ m / dynamic head = 5 %
 $\Delta P/2.5$ m / total head = 1 %

Mode of Operation :

The wind tunnel can operate at either closed or open circuit .

2) Sand roughness : the working and test sections were covered by 1/4 inch lebanite hardboard on whose surface clay chips (2 mm diameter) were glued .

3) Mesh roughness : the working section was covered by a 1.5 x .5 No.51 Aluminum Decorative Mesh from U.S.G. called "Armorweave".

In addition to the three different surface roughnesses, barriers and vortex generators were used. The barriers were constructed from strips of 1 inch thick plywood 2.8 m long and of varied widths (1.5, 3, and 4.5 in.) . The vortex generators are like those proposed by Armit and Counihan (1) . A drawing of them is given in Wilson's M.S. Thesis (83). They are right triangle in profile : 60 cm high with a 35 cm base and 6 cm thick at the back. They are wedged, the thinner front faces the flow.

The boundary layer heights achievable depend upon the type of roughness and the barrier height. Boundary layer heights measured at $x=10.9$ m range from 18 to 45 cm . All values of the longitudinal coordinate, x , are reported as measured from the beginning of the working section.

The 3/16 inch clear polycarbonate observation window described by Wilson (83) was replaced by a 1/4 inch plate glass, measuring 2.33 m x 0.8 m , in order to provide an unobstructed view of the test section.

In order to reach velocities lower than 2 m/s the four

exhaust vents downstream from the fan (approx. .35 x 1.35 m each) were equipped with a removable flow deflector (skimmers) of variable length set at 45° angle. Using this technique, sufficient air is exhausted to reduce the free stream velocity at the test section to 0.6 m/s .

A bank of 24 air filters Farr High Performance Model HP-15, each measuring 24x24x12 inches was placed at the wind tunnel exhaust for use in open circuit operation. Each filter has a rated capacity of 2000 CFM and can remove 99.8 % of particles of 10 microns .

The carriage instrument or the traverse described by - Wilson (83) , is powered by a motor through a rack and pinion system. The frame of the carriage rolls on a 3x1 in. channel. This frame for the channel was moved to the upper part of the main traversing body thus increasing the distance from the floor to the lower part of the carriage structure. A picture of the carriage and a close up of the system that provides the motion for the probe in the lateral and vertical directions are given as Figures 5.2 and 5.3 respectively.

The hot wire anemometer probes were placed within a vertical distance of 45 cm . The probes were supported by either a TSI 1150-18 or a TSI 1155-18 probe support placed inside of a locking and protecting sleeve (TSI 1158-18) . The sleeve measured 18 inches in length with an outside diameter of 1/4 in. A probe holder with a higher mass than the probe support was

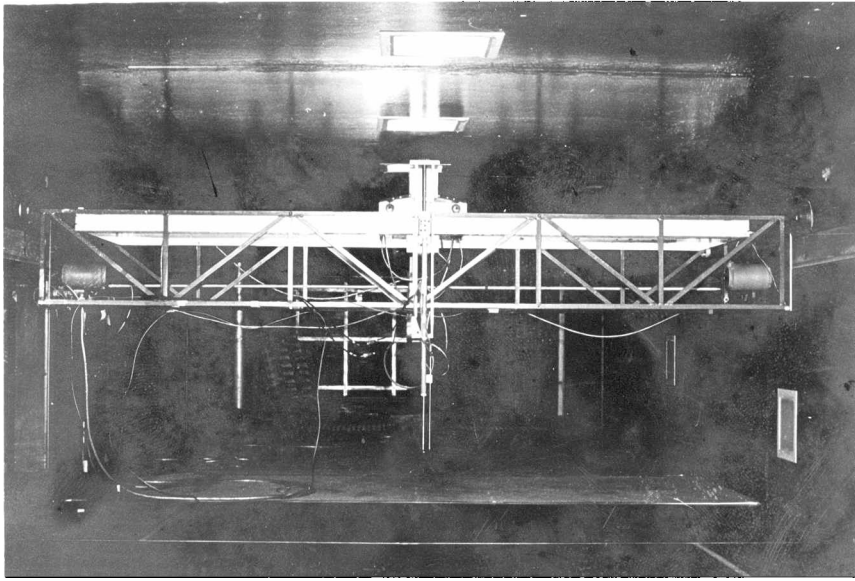


Figure 5.2 .- Instrument Carriage.

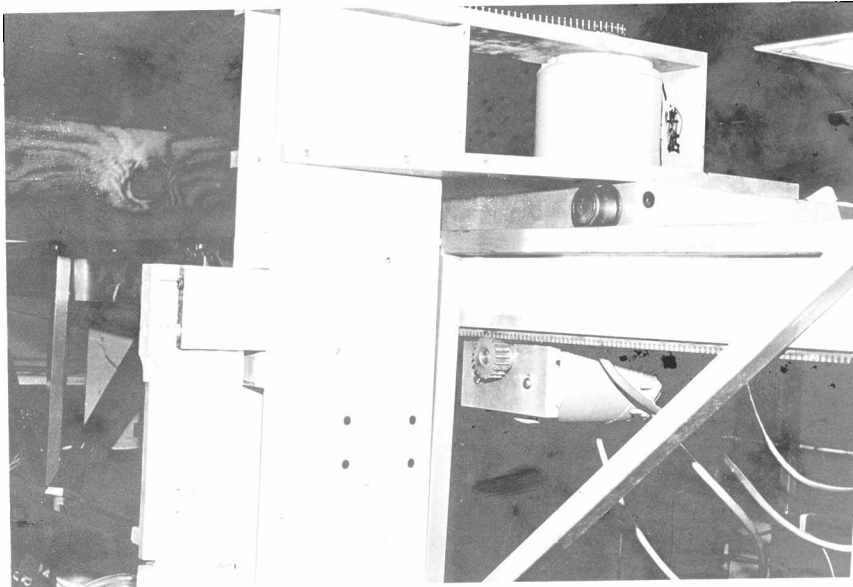


Figure 5.3 .- Driving mechanism for vertical and lateral motion of the probe in the instrument carriage.

used in order to dampen any vibrations. A probe holder with a Joukowski profile shape was designed. The drawing of this probe holder, and a photograph of the system of measuring instruments including the Pitot tube and the pressure transducer are given as Figures 5.4 and 5.5 respectively.

Vibrations measurements were performed on the test section using a vibration meter Type 1553-A from General Radio Co. . The results are given in Table 5.2 .

TABLE 5.2
VIBRATION MEASUREMENTS ON TEST SECTION

Point of Measurements	Acceleration (in./s ²)	Peak to Peak Displacement (in.)	Frequency (Hz)
Probe holder block	7.0	.006	5.4
Traverse frame	10.0	.006	6.5
Floor	10.	.006	6.5

The vibrations are of low frequency (in the range of interest of the measured energy spectrum), but the amplitude of the displacement is very small. The energy spectra measurements will not be influenced by the vibration of the wind tunnel test section.

Instrumentation

An schematic diagram of the instrumentation used to collect wind velocity data is given in Figure 5.6 . Every component of this system is described below.

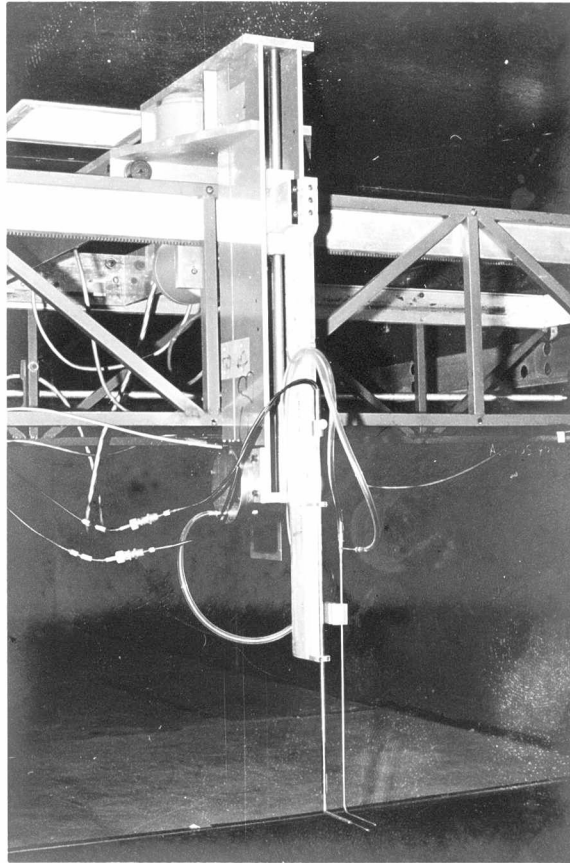
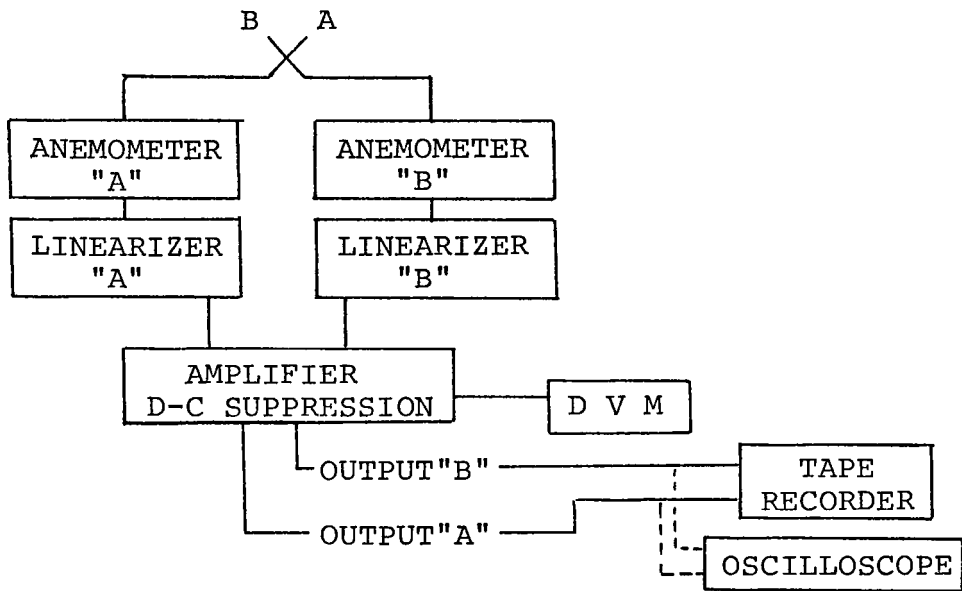


Figure 5.5 .-Probe holding system.

Constant Temperature Hot Wire Anemometer System



Pitot Tube and Pressure Transducer System

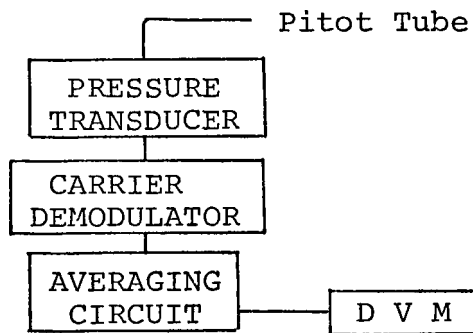


Figure 5.6.-Instrumentation

Schematic Diagram

The hot film probe and sensors used are the TSI Model 1210-20 (single wire) or the TSI Model 1241-20 (X configuration for end flow). The sensor size is .002 in. diameter x .040 in. long (.051 x 1.0 mm). This is a cylindrical quartz coated hot film. The relative frequency response quoted by the manufacturer is 40000 Hz, this being the response relationship between sensors when used with an 80 KC constant temperature anemometer in air at 300 ft/sec (≈ 100 m/s) .

Constant Temperature Anemometer.-

The system is composed of a TSI Model 1051-2 Monitor and Power Supply, 2 TSI Model 1054-A Constant Temperature Linearized Anemometer modules, and 2 TSI Model 1056 Variable Decade modules. The length of each cable from probe to anemometer was 15.2 m (50 ft.) of TSI Coaxial Probe Cable Type 10110-50. Due to malfunctioning of the 1054-A linearizers, 2 TSI Model 1005-B linearizers were used instead. The exponent of the squaring circuit $N \hat{=} .2$ was set to 2.0 . The frequency response of the whole system operating under typical conditions was 800 Hz. This measurement was done according to the TSI Manual for Model 1010A Hot Wire Anemometer. The obtained value is only approximate, but it is enough for this work's purposes since the frequencies of interest in the wind tunnel are less than 100 Hz. The noise level from the linearizer output is approx. 10 mV peak to peak of random high frequency waves. The noise to signal ratio was of the order of 1 % .

Amplifier-DC Suppression.-

In order to minimize the effect of the noise from the tape recorder, the signal was amplified by a factor of 10. At the same time, the mean of the signal was suppressed. The DC suppressed voltage was read in a Digital Volt Meter accurate to the fourth significant figure. An special circuit was built for this operation. For a diagram of this circuit, refer to Lee (38).

Oscilloscope.-

A Tektronix Type 502 A Dual Beam oscilloscope was used to continuously monitor the operation of the anemometry system and of the recording operation.

Tape Recorder.-

The tape recorder used is a portable FM recorder HP 3960 of four channels. It was operated at the speed of 3-3/4 ips for which its frequency response is 0-1250 Hz (± 1.0 dB referenced to 10 % of upper band-edge) at a signal to noise ratio of 48 dB.

Pitot Tube / Pressure Transducer.-

A Pitot Tube of 1.08 mm I.D. and 3.02 mm O.D. was used to measure the dynamic head, i.e. the velocity of the wind. The Pitot tube was connected to the pressure transducer by 1 m of Tygon tubing of 3/16 in. I.D.. The pressure transducer is a Validyne Model DP 103 for a range of $\pm .02$ psid (137.9 N/m^2) Full Scale. The sensitivity is $= .1 \text{ N/m}^2$. The carrier demodulator used was the Validyne Model CD-15 with an output of ± 10 VDC. The frequen-

cy response for the carrier demodulator is flat from 0-1000 Hz within 10 % .The noise level was of the order of 5-10 mV peak to peak of random high frequency waves 10 KHz .

Averaging Circuit.-

In order to have an average value of the signal from the pressure transducer (for mean velocity determination) was fed to an "averaging circuit" which is essentially a variable time constant capacitor. The maximum time constant, of the order of a few seconds was used.

Analysis of Data

The analysis of data was done in the Engineering Systems Simulation Laboratory (ESSL) of the Cullen College of Engineering. The taped information from the wind tunnel runs was digitized and analyzed using the Hybrid System available at ESSL . This system consists of an analog computer Hybrid Systems - Inc. HSI SS-100, a Digital-Analog Interface HSI 1044 and the IBM 360 Model 44 Digital Computer.

An X configuration hot film probe was used to obtain information about the three turbulence components of the velocity. When the X hot film forms an angle of 45° with respect to the X coordinate (in the mean direction of the flow) in the "xz" plane, both the longitudinal and the vertical turbulence velocities may be determined from the following equations (see TSI instruction manual for the Model 1015-C Correlator) :

$$u = (V_A + V_B) / \sqrt{2} \quad (5.1)$$

$$w = (V_A - V_B) / \sqrt{2} \quad (5.2)$$

where V_A and V_B are the velocities perpendicular to the hot films A and B respectively. When the X hot film forms an angle of 45° with respect to the "x" coordinate but in the "xy" plane the lateral component of the velocity is obtained from:

$$V = (V_A - V_B) / \sqrt{2} \quad (5.3)$$

The digitization program developed by Lee (38) was used with some modifications. The program works for two purposes: calibration or digitization. In the calibration mode it takes the average of the supplied signals (voltage from linearizers) and together with the supplied velocity data from the Pitot tube, performs a linear least squares fit. The linear least squares subroutine can perform up to a fourth degree polynomial fit, but only straight line fits were used. The hot wire anemometer calibration details are given in Appendix B .

In digitization mode, the coefficients of the data fit are supplied to convert the voltage signal to velocity. The digitized values of voltage are converted to velocity by using the mentioned coefficients and the equations (5.1), (5.2) and (5.3). The mean velocity, as well as the root mean square values of the fluctuating velocity in the x and y or x and z directions are calculated as well as the product $u(t)w(t)$. Eventually the values of $u(t)$ and $w(t)$ or $v(t)$ are written on digital tape if desired. A printout of the program containing definitions is on file, input and control data are explained in Appendix E 1.

The linearized anemometer output vs. mean velocity calculated from the Pitot tube is given in Appendix B . The linearity is very good for the range of velocities 2-6 m/s . Good linearity was also found for a set of runs in the range 1-2 m/s (the calibration line showed less than 1% average percent deviation). For velocities lower than 1 m/s such linearity was not investigated . In the Figure B 1 presented in Appendix B two lines are shown : for the uncorrected and corrected velocity from Pitot tube data (see Appendix A) . The correction has virtually no effect in the range 2-6 m/s, but becomes important for lower velocities, amounting to 10 % for velocities of the order of 0.5 m/s .

When measuring velocities lower than 1 m/s it would be advisable to check the following:

a) Check linearity of the linearized anemometer output (in the range of velocities investigated) .

b) Correct for the effect of viscosity on Pitot tube readings as indicated in Appendix A .

c) The zero from the pressure transducer suffers a shift of 10-20 mV during a typical run . This effect is not important for velocities greater than 2 m/s but it would amount to 30 - 40 % differences for velocities of the order of 0.5 m/s .

The values of mean velocity calculated by the digitization program should agree with the corresponding velocities calculated from Pitot Tube readings.

Values of mean velocity obtained by single wire measurements are 0.8 % consistently smaller than those obtained from Pitot tube as can be observed in Appendix C 3 . The X wire mean velocity values show differences of $\pm 1\%$ as compared to Pitot tube values (see Appendix C 3) . Based on these results an estimation of the accuracy of the turbulence intensities and Reynolds stresses (\overline{uw}) may be done . For a typical situation in which the root mean square velocity is 10 % of the total mean velocity, the turbulence intensities are expected to be accurate within $\pm 10\%$ and the Reynolds stresses (\overline{uw}) are expected to be accurate within $\pm 20\%$.

When digitizing data, a Low Pass Filter Hewlett Packard Model 5489 A was used . The effect of a finite sampling time and duration of sampling leads to an error that can not be avoided due to the discrete nature of the analysis . The duration of sampling is related to the sampling frequency required by the particular analysis , but it must be enough to sample 8192 data points required by the program , e.g. if the interest is on frequencies up to 100 Hz , according to the Nyquist criterion , the sampling frequency is of 200 samples/sec ; in order to provide the 8192 data points , the duration of sampling must be at least 40.96 sec long . The sampling frequency required by the particular analysis was determined in such a way that the output values of energy spectrum from the analysis program be in the low frequency end , comparable to atmospheric values and that the maximum of the energy spectrum -

plotted as $nS_{u_i u_i}(n)/u_*^2$ vs. $f=nz/\bar{U}$ could be observed .

A tabulation of results obtained by using two sampling frequencies , 500 and 50 samples/sec ,on the same set of runs is given in Appendix C 2 . The value of \bar{U} is the least affected ,it oscillates by about 1 % ,this fact being a good proof of stationarity . In this analysis u'_{500}/u'_{50} is consistently higher than 1 by an average of 8 % ; w'_{500}/w'_{50} oscillates - about the value of 1 by 8.5 % and similarly the \overline{uw} values by 25 % . In taking the results presented in Appendix C 2 , frequencies greater than 300 Hz for the 500 samples/sec analysis were cut-off whereas for the 50 samples/sec analysis the cut-off was for frequencies greater than 30 Hz . This seems to have no effect on the obtained results since the values of w'_{500}/w'_{50} and $\overline{uw}_{500}/\overline{uw}_{50}$ oscillate about 1 .

A sinusoidal signal whose RMS voltage read with a true RMS meter (TSI Model 1060) was .0734 showed a value of .0745 as calculated by the digitization program , a 1.5 % higher value .

A very important feature of the digitization program is the ability of sampling analog signals simultaneously . This feature was tested always before running the digitization program by analysing a common signal to the multiplexers . Sampling times up to 500 samples/sec were normally used in this work , however even a sampling time of 10000 samples/sec was tried once and very good results obtained.

A set of runs was analyzed by two methods : by the digitization program and by using a correlator (TSI Model 1015-C) and an RMS Meter (TSI Model 1060) . The results for u'/\bar{U}_{\max} and w'/\bar{U}_{\max} are compared in the Appendix C 1 . Average percent deviations of 4 % are found for the former and of 8 % for the latter .

All the above results give reliability to the method of analysis of data used in this work .

The program allows for temperature compensation (see Lee (38)) . However the change in temperature during a set of runs very rarely exceeded 2°F and the temperature compensation factor was always very close to 1 .

An improved version of the statistical analysis program developed by Lee (38) was used . The program accepts an input of fluctuating velocity obtained by the digitization program (either $u(t)$ and $w(t)$ or $v(t)$) and recorded on digital tape and calculates and plots :

a) Probability density distribution for u and w (or u and v) .

b) Using the Fast Fourier Transform technique , the energy spectrum (S_{uu}, S_{ww} or S_{vv} and S_{uw}) and the correlation coefficient (R_u, R_w or R_v and R_{uw}) are obtained . The output of energy spectrum has been averaged on frequency domain and every value plotted is actually an average of 27 individual values.

Depending upon the frequency range of interest , the sam-

pling time is set according to the Nyquist criterion, i.e. sampling time equal to twice the maximum frequency of interest. The Hewlett Packard 5489 Low Pass Filter was used to eliminate those frequencies above the maximum of interest in order to avoid the aliasing effect. The performance of this filter is given in the Appendix D. Input control data are explained in Appendix E 2. A printout of the program is on file.

In order to test the program, a sinusoidal signal of 10 Hz was analyzed. The correct shape of probability density, energy spectrum and correlation coefficient was obtained. The only point of the energy spectrum occurs at 9.9 Hz. The correlation coefficient shows a cosine wave of 10 Hz.

The root mean square value of the signal can be calculated from the correlation coefficient at $\tau=0$. The values of u' , w' and \overline{uw} calculated in this way agreed very well (within $\pm 2\%$) when compared to the corresponding values calculated from the digitization program.

Smoke Generator .-

Smoke for the flow visualization tests was produced by a smoke generator. The pump and electric heater from a commercially available "fogger" were used in the construction of the smoke generator. A schematic diagram of the smoke generator is given as Figure 5.7. When working the pump intermittently, the frequency and length of shot may be controlled by a pump control circuit constructed for this purpose. The drop size

may also be controlled by an adjustment in the pump . A homogeneization chamber was necessary when working the pump intermittently in order to have a constant density smoke at the dosification point .

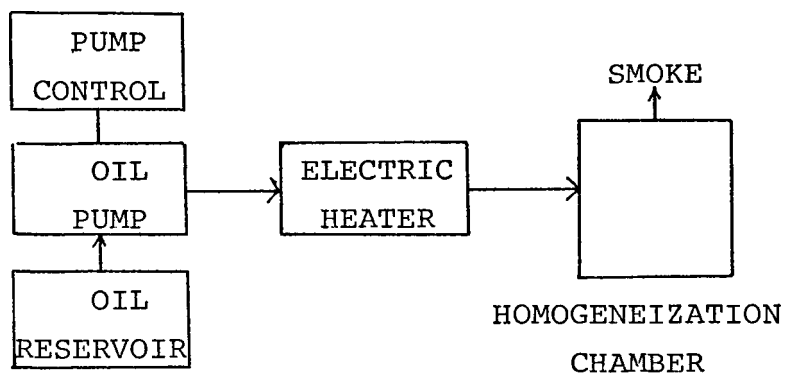


Figure 5.7.-Smoke Generator

CHAPTER VI

EXPERIMENTAL RESULTS

The effect of the turbulence generating devices on the wind tunnel flow characteristics is studied in the next section . The turbulence intensities and Reynolds stresses (referred to the free stream velocity) reported in this section are subject to a systematic error . The reported turbulence intensities and Reynolds stresses values are estimated to be 5 and 10 % higher than the correct values respectively . The error arised from a mistake in the Pitot tube viscosity effects correction (see Appendixes A and B). Such systematic error is small and will be neglected . All the reported mean velocity data have been corrected and are no subject to the error noted above . The objective of this section is to select the potentially useful configurations for simulating A B L flows . Such configurations will be investigated in detail in the second part of this chapter .

Turbulence Generating Devices Effect on Flow Field

The system composed of surface roughness , vortex generators and a barrier was chosen for developing flows similar to those typically found in the atmosphere . A considerable number of authors have reported the effect of the above mentioned devices on boundary layer flow . However, due to the different

dimensions of wind tunnels and the diversity of surface roughnesses , barrier heights and the shape of vortex generators used by different authors , the results in the literature can only be used as a qualitative guide . In this section these effects are quantified for the U H E W T and often compared to the results reported by other investigators under similar conditions for consistency . Another objective of the work discussed in this section is to observe which devices are useful and to what degree for reproducing the desired features of A B L flows .

Since our first concern is to produce an approach flow which is in equilibrium (self preserving) , measurements of the mean velocity using a hot wire anemometer or Pitot tube were taken in order to find whether an equilibrium flow is reached or not . The criteria for equilibrium developed in Chapter II was followed . According to this criterion , the shape factor should be approx. 1.3 and the parameter $C \cong 6.1$ (see equation 2.49) . The mean velocity profile plotted as the velocity defect law should exhibit a universal shape consistent with equilibrium boundary layer experiments under zero pressure gradient .

Mean velocity profiles measured with a Pitot tube are very close to the corresponding velocity profiles measured with a single hot wire anemometer . In an analysis of two sets of runs , Pitot tube values were on an average 0.8 % higher

than single hot wire measurements . A similar comparison between X hot film values and Pitot tube values for three sets of runs showed an average of 1 % difference (see Appendix C 3) .

In Table 6.1 the boundary layer displacement and momentum thicknesses as well as the shape factor and the parameter C (equation (2.49)) are shown for a variety of surface roughness and barrier heights . The boundary layer thickness has been defined as the distance from the surface at which the mean velocity attains 99 % of its free stream value . This value is not very accurate , but it is needed for scaling determination by comparison with typical boundary layer heights measured in the A B L .

Analysis of the smooth surface data reveals that the shape factor values are close to 1.3 and do not vary with velocity at a fixed distance e.g. $x=10.9$ or with distance between $x=8.5$ and 10.9 m for the same velocity . However, the value of H for the lowest free stream velocity case (0.6 m/s) is too low . Further comments on this point will be done after analysis of the Law of the Wall and the Velocity Defect Law . The parameter $C = 6.54$ is also in fair agreement with the equilibrium value (7 % higher) .

Analysis of the sand roughness surface data reveals values of the shape factor in the range 1.3 to 1.4 between $x=8.5$ and 10.9 m . The parameter $C = 6.05$ is in excellent agreement with the equilibrium value of 6.1 . The effect of putting a 1.5 in.

TABLE 6.1

BOUNDARY LAYER CHARACTERISTICS

Set No.	\bar{U} (m/s)	x (m)	type of surface	δ (cm)	δ_x (cm)	θ_M (cm)	H	C	Data Source
1012-B	6.06	8.5	smooth	15.0	2.16	1.56	1.38		P
1012-A	6.05	10.9	smooth	17.5	2.61	1.92	1.36	6.54	P
1016-A	2.05	10.9	smooth	18.0	2.83	1.99	1.42		P
1019-A	2.10	10.9	smooth	18.0	3.39	2.44	1.39		S
1016-B	0.90	10.9	smooth	12.0	1.14	.93	1.23		P
1019-B	0.58	10.9	smooth	12.0	1.67	1.39	1.20		S
108	6.21	8.5	sand	17.5	2.88	2.10	1.37		S
107	6.24	9.7	sand	20.0	3.11	2.29	1.36	6.05	S
711-A	6.14	10.9	sand	22.5	3.42	2.56	1.33		X
703-B	6.04	10.9	sand+1.5in. barrier	30.0	4.03	3.11	1.30		X
109	6.24	9.7	sand+3in. bar.at x= 3.66 m	42.0	4.64	3.76	1.23		S
203-A	6.06	11.6	idem	40.5	4.51	3.55	1.27		P
815-B	6.12	8.6	mesh	33.0	8.36	5.10	1.64	6.43	S

P : from Pitot tube

S : from single hot film

X : from X hot film

barrier 0.6 m before the beginning of the working section does not affect the equilibrium at a distance where a model would be typically placed . The shape factor is 1.3 .

When a 3 in. barrier is placed 3.66 m from the beginning of the working section (6 m from the measuring point) , a velocity profile with an acceptable low shape factor (1.23) measured at $x=9.7$ m is produced . The value of H for this case changes to 1.27 at $x=11.6$ m .

The shape factor for the mesh roughness surface measured at $x=8.6$ m is considerable higher than 1.3 , the equilibrium value , but the parameter $C = 6.43$ is in fair agreement with the equilibrium value of 6.1 . Clauser (12) stated that the shape factor H is not a universal parameter , whereas C is a universal parameter . The high value of H is due to the large roughness height of the mesh roughness ,but that effect is included in u_* in the parameter C (see equation (2.49)) .

It is concluded from this analysis that the sand and mesh roughness surface flows are in equilibrium for a free stream velocity of 6 m/s , as measured at $x \geq 8.6$ m, i.e. where a model would be placed . For the smooth surface flows , equilibrium was found in the range of velocities 0.6 - 6 m/s at a distance $x \geq 8.6$ m . The 1.5 in. barrier placed at 0.6 m before the beginning of the working section does not affect the equilibrium . Placing the barrier at $x=3.66$ m produces a near to equilibrium flow .

Velocity Effect.-

It has been concluded that equilibrium flows are found in the range of free stream velocities 0.6 to 6 m/s . The Law of the Wall is plotted for the free stream velocities 6.15, 2.08 and .573 m/s over a smooth surface in Figure 6.2 . A table presenting the most important parameters of the runs presented on the Figures of this chapter is given in Appendix F . The value of u_* has been calculated by assuming the Law of the Wall, as proposed by Clauser (12), holds in the range $50 < zu_*/\nu < 500$. Clauser proposed the following formula which fits the results of various investigators :

$$\frac{\bar{u}}{u_*} = 2.44 \ln \frac{u_* z}{\nu} + 4.9 \quad (6.1)$$

It is concluded from Figure 6.2 that flows in the range of free stream velocities 0.6 - 6 m/s closely obey the Law of the Wall .

The same sets of runs are plotted as the Velocity Defect Law in Figure 6.3 and compared against Clauser (12) who proposed the formula :

$$\frac{\bar{u}_\delta - \bar{u}}{u_*} = -2.44 \ln \frac{z}{\delta} + 2.5 \quad ; \quad z < \delta < 0.15 \quad (6.2)$$

Klebanoff and Diehl (37) proposed:

$$\frac{\bar{u}_\delta - \bar{u}}{u_*} = -\frac{1}{k} \ln \frac{z}{\delta} + 2.35 \quad ; \quad z/\delta < 0.15 \quad (6.3)$$

where $k=0.4$. Equations (6.2) and (6.3) are almost equivalent.

SET	FLOOR	$1/\alpha$
○ 1012-A	SMOOTH	.117
□ 628	SAND	.177
△ 815-B	MESH	.389
⊕ 804-B	MESH/SMOOTH	

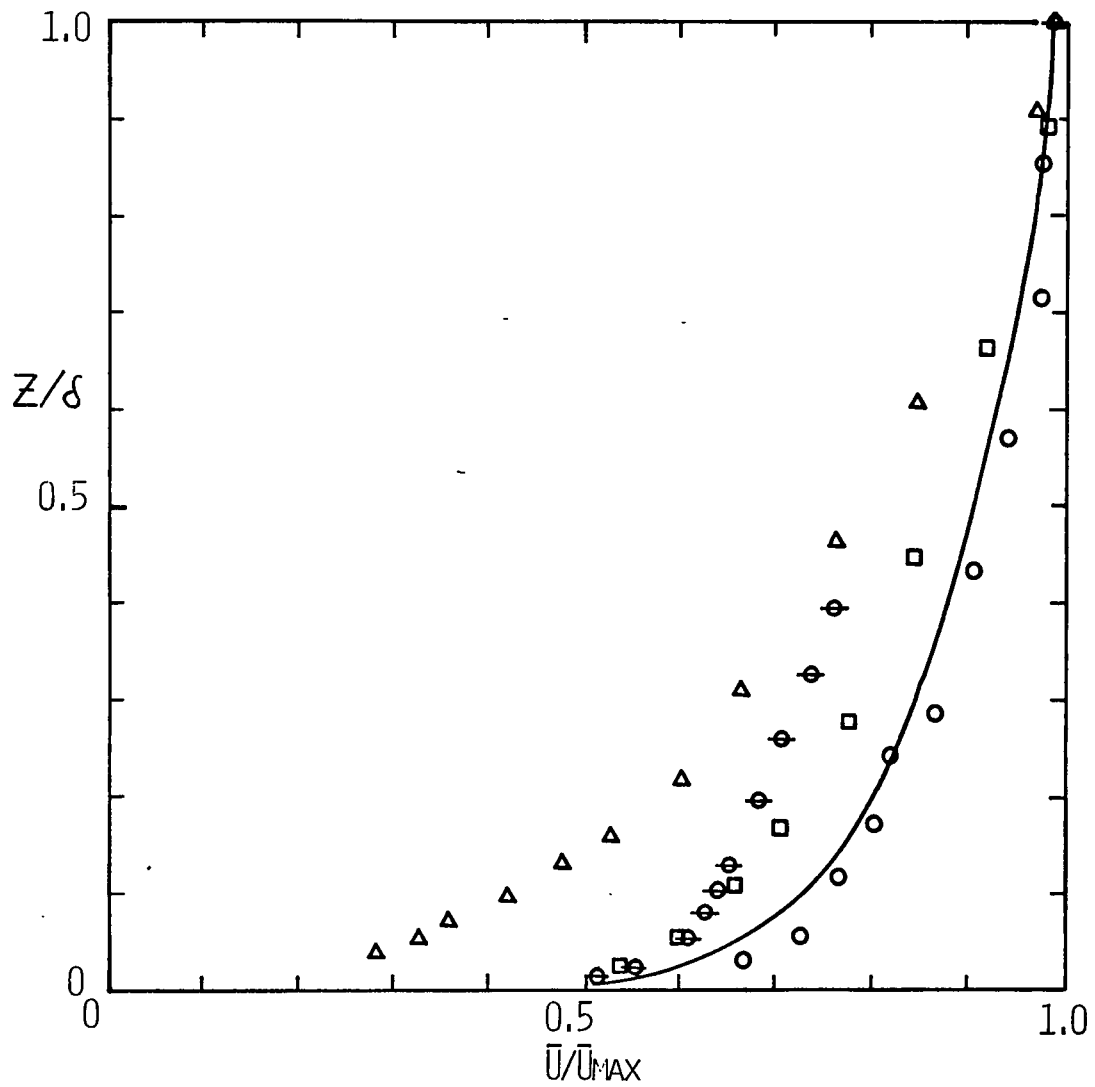


FIGURE 6.1.- ROUGHNESS EFFECT ON MEAN VELOCITY PROFILE.

	SET	FLOOR	\bar{U}_S (m/s)
○	1018-A	SMOOTH	6.15
□	108	SAND	6.15
△	815-B	MESH	6.06
⊕	1019-A	SMOOTH	2.08
⊙	1019-B	SMOOTH	0.573

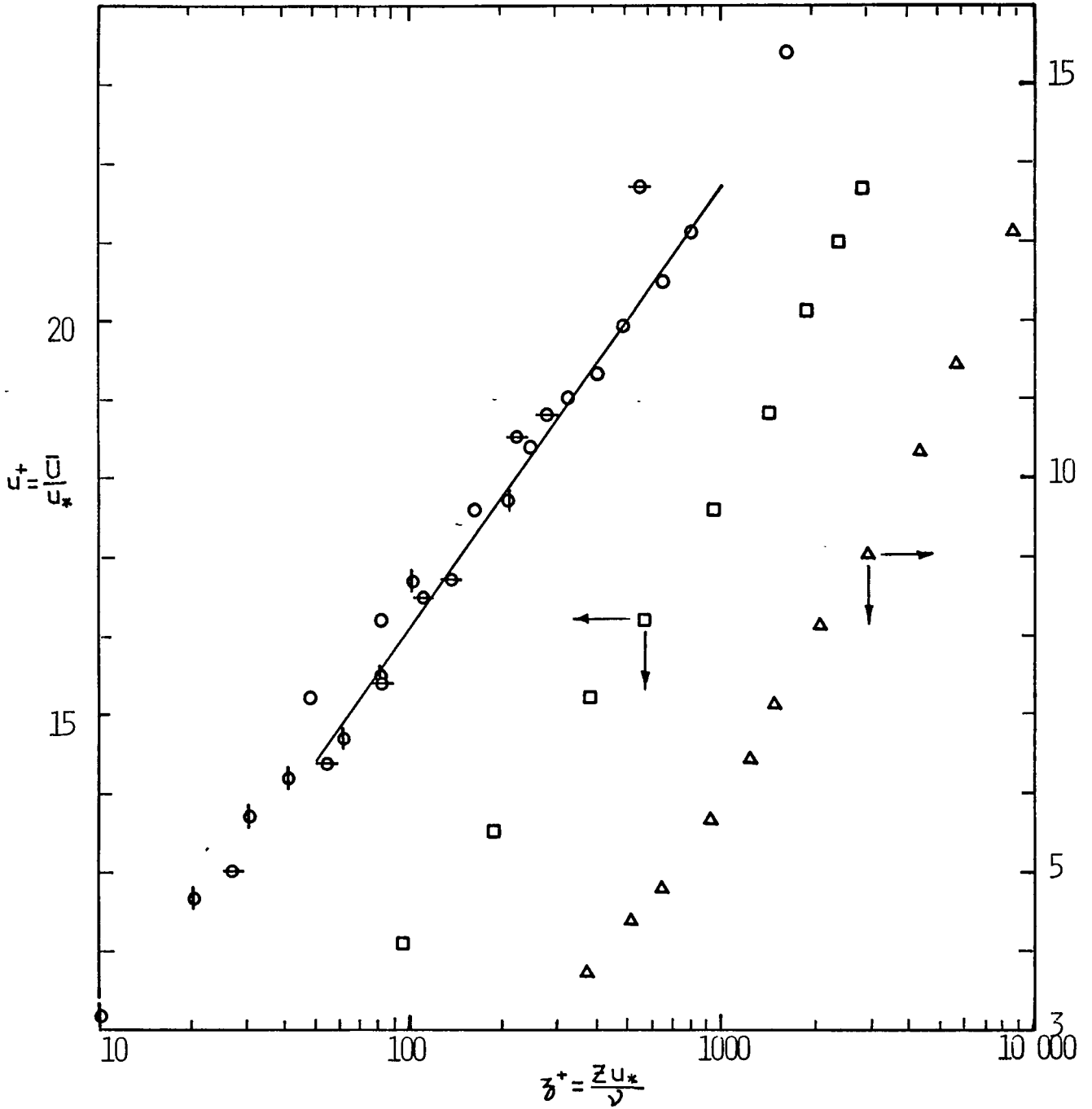


FIGURE 6.2.- LAW OF THE WALL
ROUGHNESS AND VELOCITY EFFECT

	SET	FLOOR	\bar{U}_δ (m/s)	K
○	1018-A	SMOOTH	6.15	.507
□	108	SAND	6.15	.420
△	815-B	MESH	6.06	.430
⊖	1019-A	SMOOTH	2.08	.404
ϕ	1019-B	SMOOTH	0.573	.450
▲	819	MESH (x=7.2m)	6.00	.410

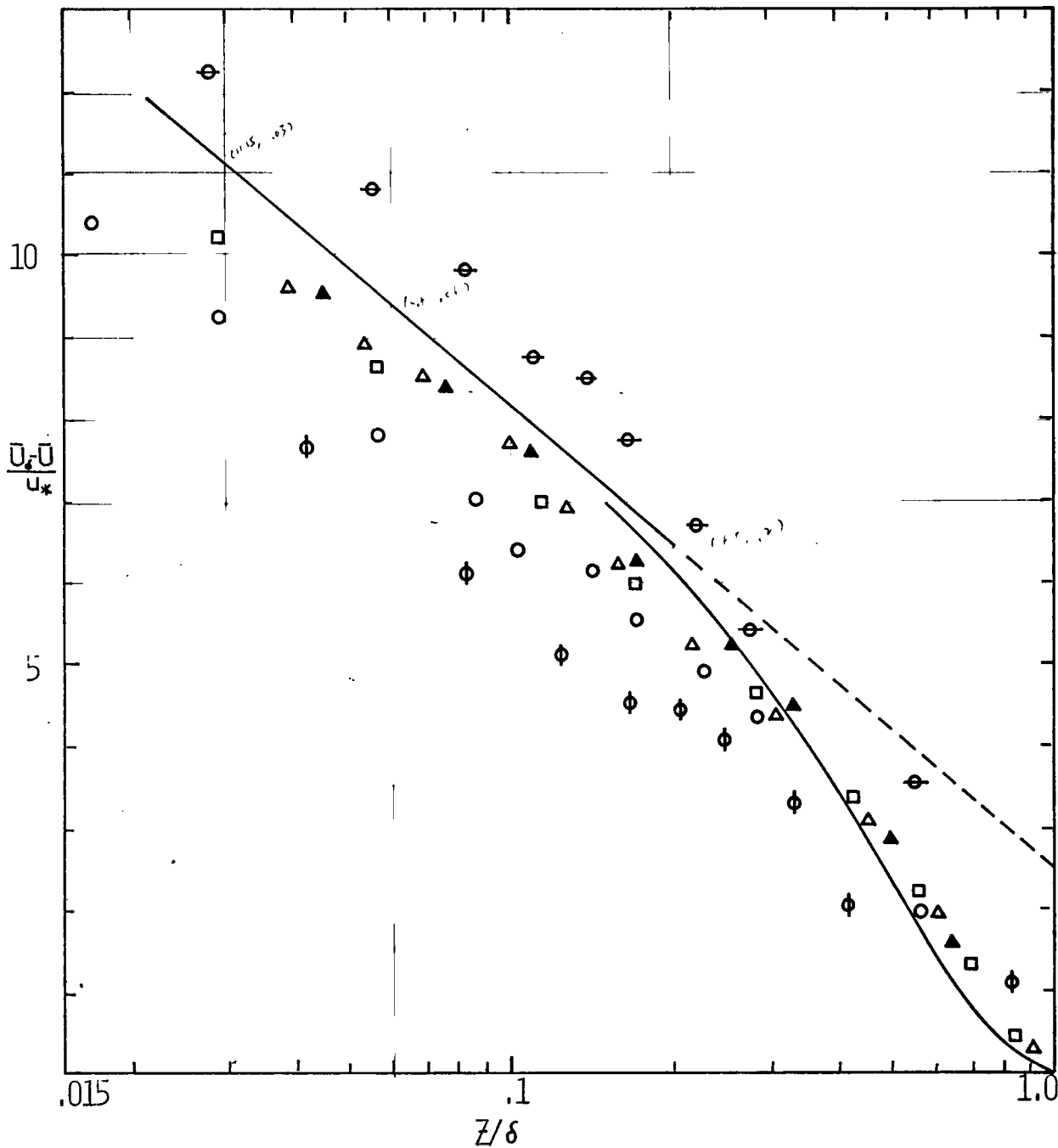


FIGURE 6.3.- VELOCITY DEFECT,
ROUGHNESS AND VELOCITY EFFECT.

For values of $z/\delta > 0.15$, Hama (22) proposed the equation:

$$\frac{\bar{u}_z - \bar{u}}{u_*} = 9.6 \left(1 - \frac{z}{\delta} \right)^2 ; z/\delta > 0.15 \quad (6.4)$$

which is also plotted in Figure 6.3 .

The values of k according to equation (6.3) which would best fit this work's data are given on Figure 6.3 .Considerable differences between the runs over smooth surface at free stream velocities of 6.15 and .573 m/s , and equation (6.2)are found. It is believed that this differences are due to inaccuracy in the u_* values . Note that a 20 % difference in the u_* value would give a very good fit for the set at a free stream velocity of 6.15 m/s . The u_* values are estimated to be accurate within ± 10 % .

The flows for free stream velocities greater than 2 m/s satisfy all the criteria for equilibrium . The flow having a free stream velocity of 0.6 m/s shows a low shape factor and a poor Velocity Defect fit . The estimated accuracy for velocity values of the order of 0.5 m/s is estimated to be ± 10 % . Reliable conclusions can not be obtained with such a low accuracy on velocity data . However , since the above noted deviations are not large , it is believed at the present time ,that an equilibrium flow is found even at free stream velocities as low as 0.6 m/s and for distances "x" greater than ≈ 10 m .
Roughness Effect.-

Three types of surfaces : smooth , sand roughness and -

mesh roughness were used in the wind tunnel runs in order to assess their effect on mean velocity profile , longitudinal , vertical and lateral turbulence intensities , Reynolds stresses (\overline{uw}) , and the length scales at downstream distances where a model would be placed . The characteristics of these surfaces have already been given in Chapter V .

Roughness Effect on Mean Velocity.-

The mean velocity profile has been plotted in Figure 6.1 . The power law exponent for each set of runs is shown on the plot . The effect of a rougher surface is to produce a velocity profile having a higher power law exponent according to equation (3.2) . The 1/7 power law profile is also shown for comparison . Teunissen (79) (80) obtained similar results.

The effect of roughness on the Law of the Wall is plotted in Figure 6.2 . The value of u_* for rough surfaces is calculated from equation (2.34b) assuming $k=0.4$. When the roughness height is large, e.g. for the mesh roughness , equation (2.34b) is modified to account for the zero plane displacement, d , i.e. the distance above the wall but between the height of the roughness elements at which the mean velocity profile seems to fall to zero . Equation (2.34b) becomes

$$\frac{\bar{u}}{u_*} = \frac{1}{k} \ln \frac{z-d}{z_0} \quad (6.5)$$

According to this equation, the roughness length z_0 for the mesh roughness was calculated to be 0.314 cm , and according to -

equation (2.34b) for the sand roughness $z_0 = 0.00436$ cm . The value of d was such that it would give the best fit of a logarithmic velocity profile similar to equation (6.5) .

Hama (22) reported that the effect of roughness on the Law of the Wall was to produce a shift downwards equivalent to $\Delta\bar{u}/u_*$. He proposed the equation :

$$\frac{\bar{u}}{u_*} = 2.44 \ln \frac{u_* z}{\nu} + 4.9 - \frac{\Delta\bar{u}}{u_*} \quad (6.6)$$

where $\Delta\bar{u}/u_*$ depends on the roughness length and increases with it . Observation of Figure 6.2 shows that the results are consistent with the above equation . Equation (6.1) is plotted for comparison .

The Velocity Defect Law should be universal , in this case, independent of roughness . It is plotted in Figure 6.3 for the smooth and two rough surfaces and compared to the equations (6.2) and (6.4) . The agreement is good for the sand and mesh roughness , having a value of k according to equation (6.3) of .42 and .43, respectively . The change in the Velocity Defect for the mesh roughness flooring is not significant between $x = 7.2$ and 8.5 m . This fact is consistent with the conclusion made earlier about having an equilibrium flow from analysis of the parameter C (equation (2.49)) . Note that the flow produced by the mesh roughness has a power law similar to the one characteristic of flow over an urban area .The experimental results on the Velocity Defect Law above a smooth surface have already been discussed .

	SET	FLOOR	x (m)
○	1012-A	SMOOTH	10.9
□	628	SAND	8.5
△	812-A	MESH	8.5
⊕	711-A	SAND/SMOOTH	10.9
ϕ	803	MESH/SMOOTH	10.9

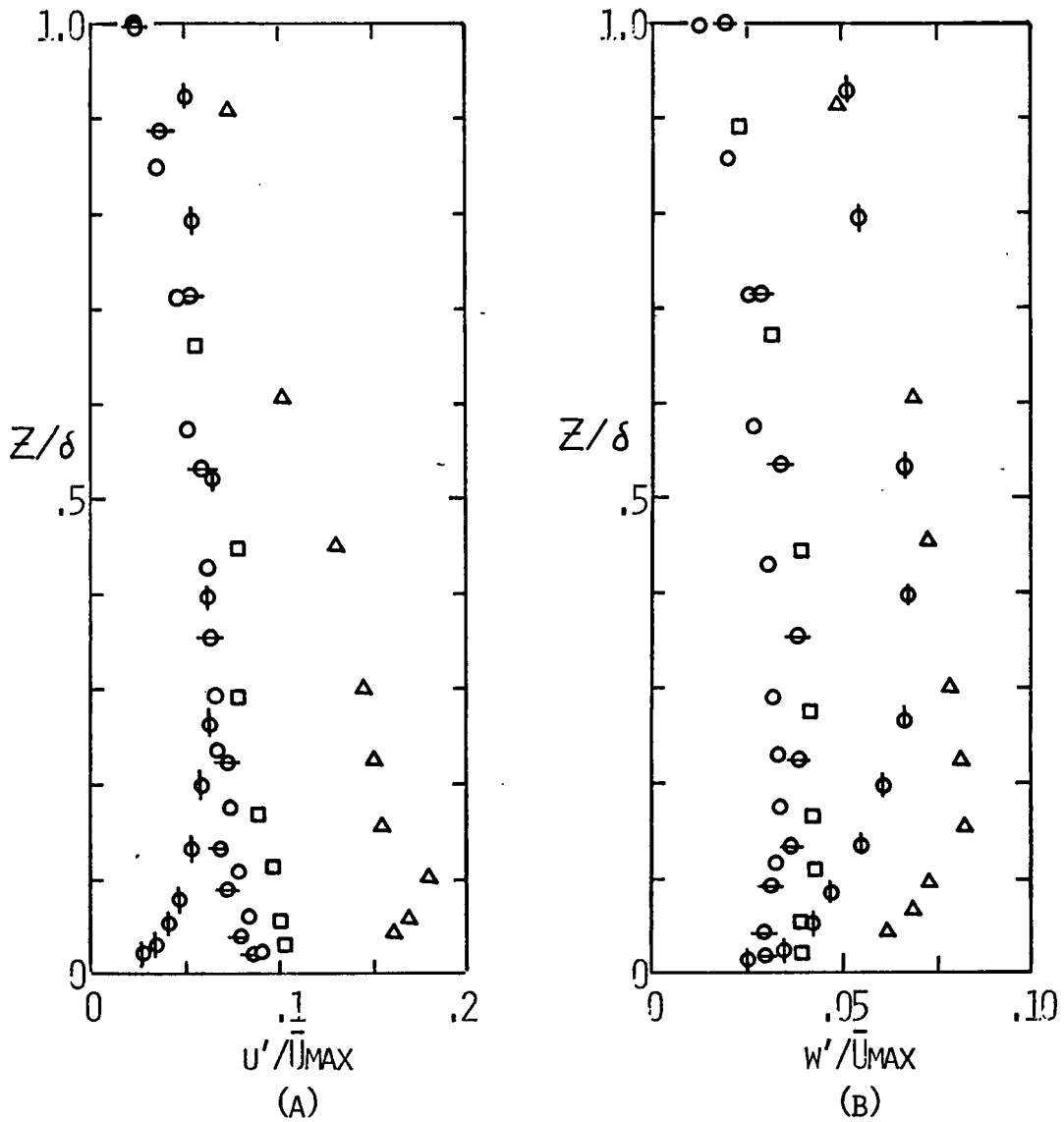


FIGURE 6.4.- ROUGHNESS EFFECT ON TURBULENCE INTENSITIES.

SET	FLOOR	SET	FLOOR		
○	1121	SMOOTH	○	1012-A	SMOOTH
□	115	SAND	□	628	SAND
△	814	MESH	△	812-A	MESH
⊖	712-A	SAND/SMOOTH	⊖	711-A	SAND/SMOOTH
ϕ	804-A	MESH/SMOOTH	ϕ	803	MESH/SMOOTH

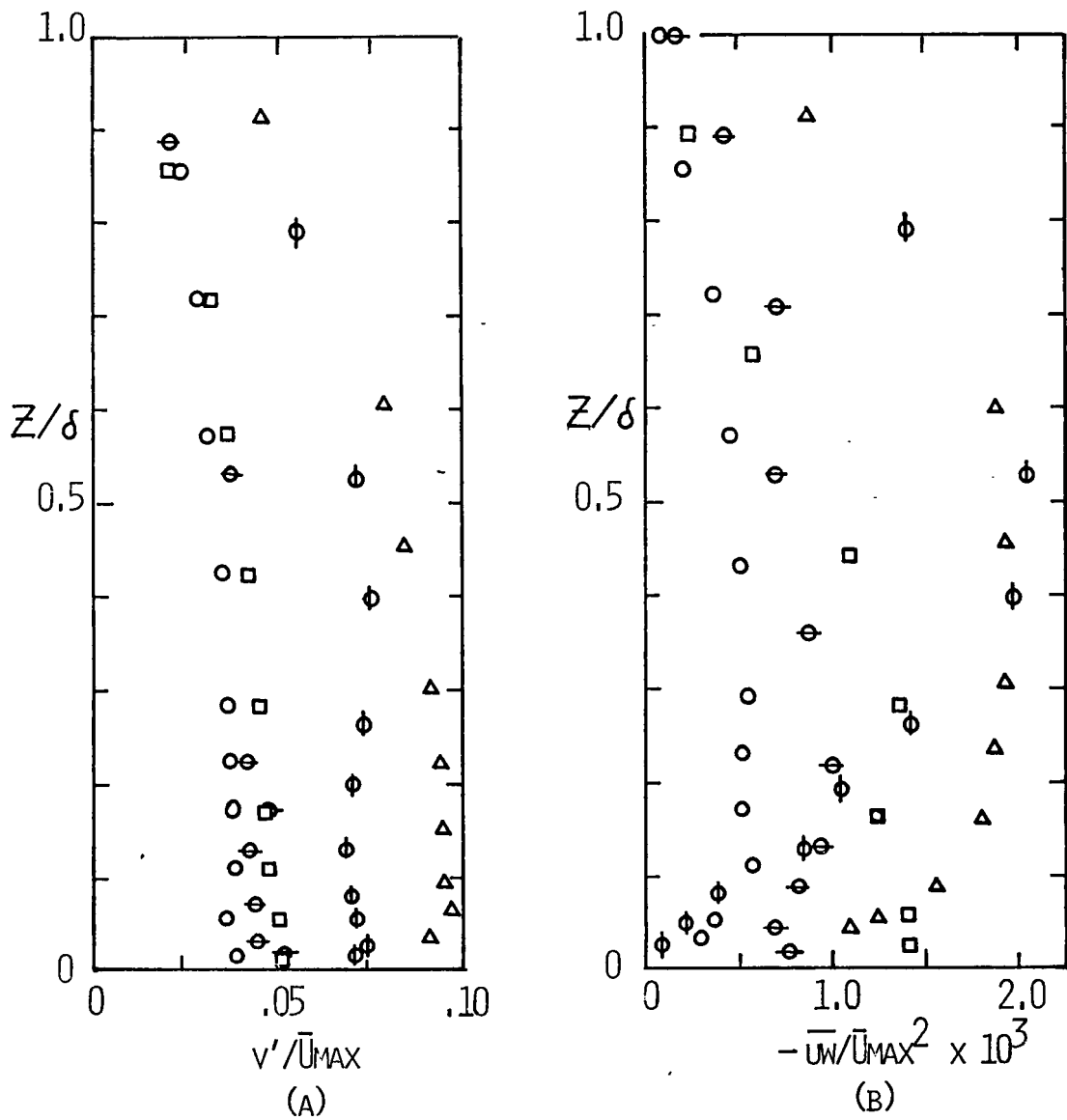


FIGURE 6.5.- ROUGHNESS EFFECT ON TURBULENCE INTENSITIES AND REYNOLDS STRESS.

Roughness Effect on Turbulence Intensities and Reynolds Stresses (\overline{uw}) .-

The roughness effect on turbulence intensities and Reynolds stresses (\overline{uw}) is plotted in Figures 6.4 and 6.5 as a function of height . Also plotted in these Figures is a set of runs - where measurements are taken after a change of surface roughness , rough to smooth . They will be discussed later .

It is observed that the rougher the surface , the higher the values for turbulence intensities in all three directions and for the Reynolds stresses (\overline{uw}) . The turbulence intensities produced by the mesh roughness double those produced by the sand roughness in the lower third of the boundary layer. In the lower half of the boundary layer , the longitudinal - turbulence intensity is greater than the lateral , which in turn is even greater than the vertical for the three types of surface tested . This is consistent with Counihan (17) .

Roughness Effect on Vertical Length Scales.-

The length scales $L_{w,x}$ are obtained by integration of the correlation coefficient (see equation (2.72)) resulting from the statistical analysis performed on the corresponding component of the Eulerian fluctuating velocity as described in Chapter II . The Taylor's Hypothesis has been assumed in order to convert the time scale obtained to a length scale (see eqn. (2.73)) . In order to integrate the correlation coefficient, it was truncated arbitrarily after it falls to zero and starts

oscillating about the time axis . The truncation was done at the point where the curve cuts the time axis for the second time . This value was in the average $\pm 10\%$ different from the value obtained either at the first or third crossing of the time axis .

The effect of roughness in the vertical length scales is shown in Table 6.2 .

TABLE 6.2
EFFECT OF ROUGHNESS ON VERTICAL LENGTH SCALES

Set No.	Roughness	z (cm)	z/δ	$L_{w,x}$ (cm)	$L_{w,x}/\delta$
628	Sand	16.	.89	2.71	.151
		8.	.44	2.76	.153
		3.	.17	2.40	.133
		1.	.06	1.35	.075
812-A	Mesh	20.	.61	5.83	.177
		10.	.30	4.10	.124
		5.	.15	4.00	.121
		2.	.06	2.11	.064
1012-A	Smooth	10.	.57	2.15	.123
		5.	.29	1.74	.100
		3.	.17	2.02	.115
		2.	.11	1.48	.085

The higher the roughness ,the higher is the vertical length scale . However,the normalized values , are similar for the three types of working section surface .

Change of Surface . Transition Effects .-

When the surface characteristics change ,so do the characteristics of the flow . An internal boundary layer is developed. The characteristics of this internal boundary layer depend - upon the surface type above which it develops . An approach flow already in equilibrium is modified after a roughness change. This effect is studied in this section . Jackson (31) derived from the analysis of available experimental data , a correlation for the "zone of influence height" as a function of distance downstream the change of roughness point . Antonia and Luxton (1) found that for a change in roughness from rough to smooth,a new state of equilibrium for the whole boundary layer is attained only at about 16 boundary layer heights downstream of the transition point with the region close to the wall being the first to adapt to the new surface conditions . The roughness height was 3.2 mm and the boundary layer height was 6.1 cm in their experiments .

In Figure 6.6 the Law of the Wall is plotted in order to observe the transition rough-smooth effect . The rough surface flooring was up to 8.5 m of the test section and the measurements were done on the smooth surface 2.4 m downstream from the roughness change . The values measured above sand and mesh roughness , as well as above smooth floor , are plotted for comparison . The lower part of the boundary layer (up to $z^+ = 1000$) obtained the characteristics of the smooth floor in -

SET	FLOOR	x (m)
○ 1018-A	SMOOTH	10.9
□ 108	SAND	8.5
△ 815-B	MESH	8.5
⊕ 718-A	SAND/SMOOTH	10.9
ϕ 804-B	MESH/SMOOTH	10.9

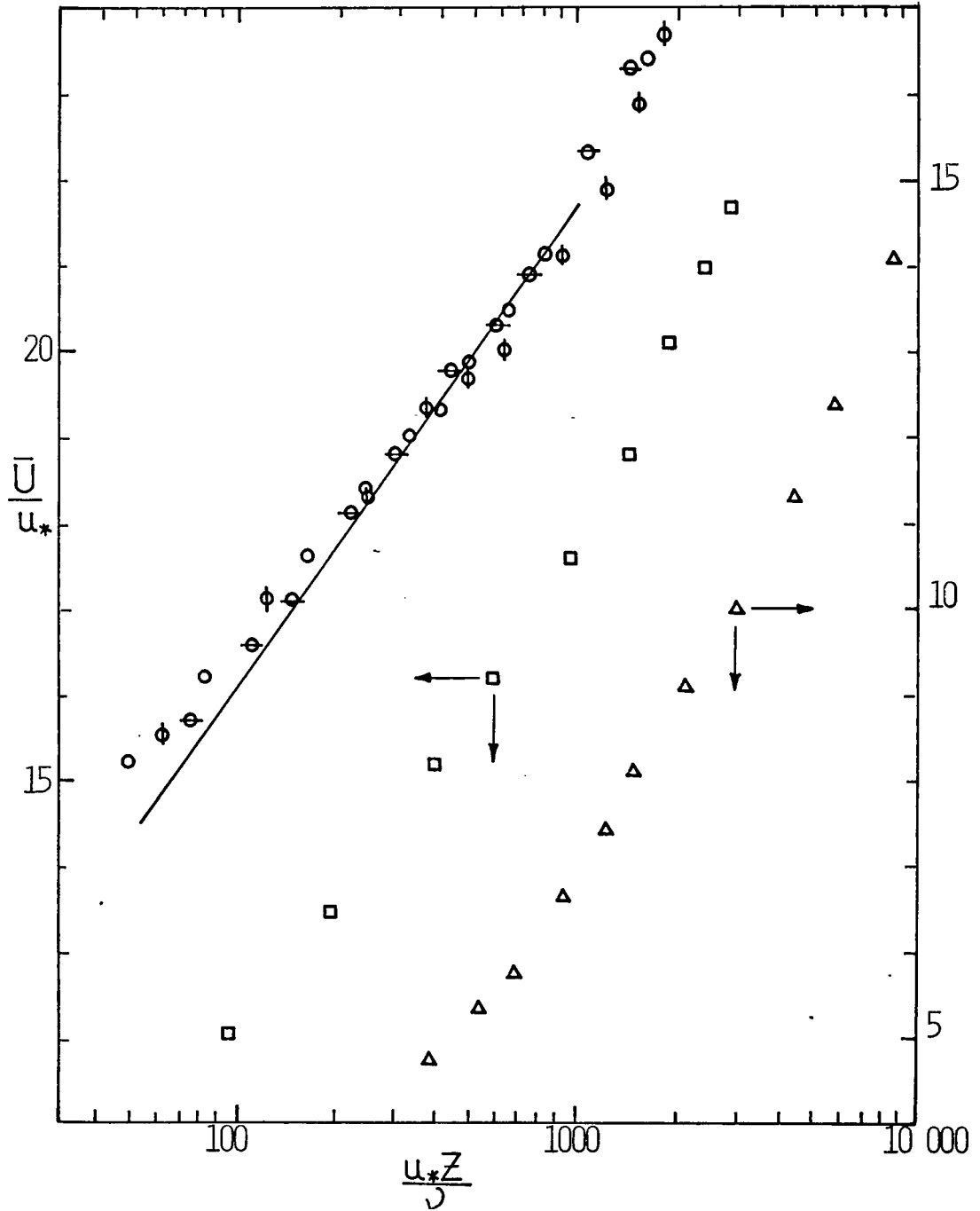


FIGURE 6.6.- LAW OF THE WALL.
TRANSITION ROUGH/SMOOTH EFFECT.

this 2.4 m interval . However , in Figure 6.1 the velocity profile for the mesh-smooth transition attains its characteristic mesh roughness velocity profile at $z/\delta \sim 0.5$. The transition rough-smooth effect on turbulence intensities and Reynolds stresses (\overline{uw}) may also be observed from Figures 6.4 and 6.5.

The turbulence intensities decrease after the change in roughness particularly in the lower part of the boundary layer and the Reynolds stresses are extremely small near the smooth floor . The approach flow to a model must be in equilibrium. It is advisable to avoid any change of surface roughness upstream from the model .

Barrier Effect.-

The effect on the flow field produced by three different barriers : 1.5 , 3 and 5 inches in height , placed 0.6 m before the beginning of the working section ($x=0$) and the effect of a 3 inches barrier placed at $x=3.66$ and 6.1 m on the working section is studied below . The working section floor was covered by the sand roughness surface up to $x=8.5$ m followed by smooth floor . Most of the measurements were done at $x=10.9$ m. The expected rough-smooth transition effect can not affect this analysis on barrier effect since the barrier affects the outer portion of the boundary layer . The effect of a barrier is to produce a flatter velocity profile , as can be observed in Figure 6.7a . The power law exponent $1/\alpha$ decreases with increasing barrier height . The 5 inches barrier produces a

SAND ROUGHNESS FLOOR, $x=10.9$ M
 SET BAR. HEIGHT (IN) $1/\alpha$

SAND ROUGHNESS FLOOR
 SET 3" BAR. AT x (M)
 $X = (M)$

○	711-A	---	.138
□	703-B	1.5	.127
△	711-B	3.0	.112
●	222	5.0	.107

○	109	3.66	9.7
□	207	6.10	9.7
●	203-A	3.66	11.6
■	203-B	6.10	11.6

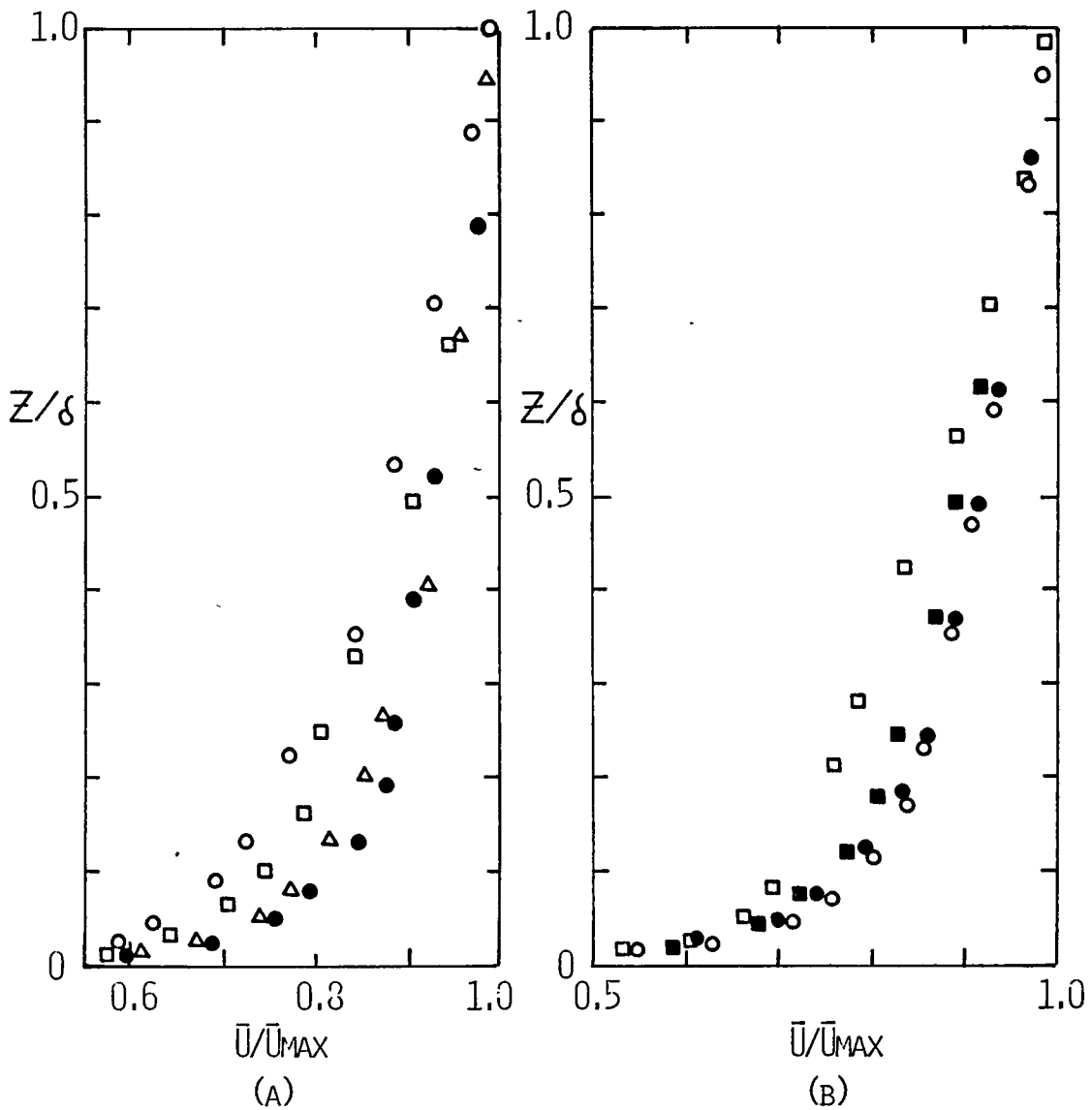


FIGURE 6.7.- BARRIER EFFECT ON MEAN VELOCITY PROFILE.

velocity profile with an inflection around $z/\delta \sim 0.3$ and the velocity profile for this case is not accurately represented by a power law . The above trend is opposite to the results reported by Counihan (16) . However , he measured his velocity at a distance downstream from the barrier having 4.5 boundary layer heights much nearer to the barrier than in this work's experiments . The barrier produces a thicker boundary layer which is directly proportional to boundary layer height. This trend is consistent with Teunissen (79) .

Placing the 3 inches barrier at $x=3.66$ m (see Figure 6.7 b) results in a mean velocity profile which does not change appreciably between $x=9.7$ and 11.6 m . Whereas when the 3 in. barrier is placed at 6.10 m, the mean velocity profile changes, increasing about 5 % from 9.7 to 11.6 m in the region of most interest, i.e. $0.1 < z/\delta < 0.4$, which is an indication of non - equilibrium .

The effect of the barrier on longitudinal and vertical turbulence intensities is shown in Figure 6.8a and 6.8b and the effect on the lateral turbulence intensity and on Reynolds stresses is shown in Figures 6.9a and 6.9b respectively . All turbulence intensities and the Reynolds stresses are increased by using a taller barrier . This effect is greater in the upper part of the boundary layer . The above results are consistent with the data of Mc Vehil (42) and Teunissen (79) .

The turbulence intensities and Reynolds stresses produced

SET	BAR. SIZE (IN)
○ 711-A	---
□ 703-B	1.5
△ 711-B	3.0
● 222	5.0

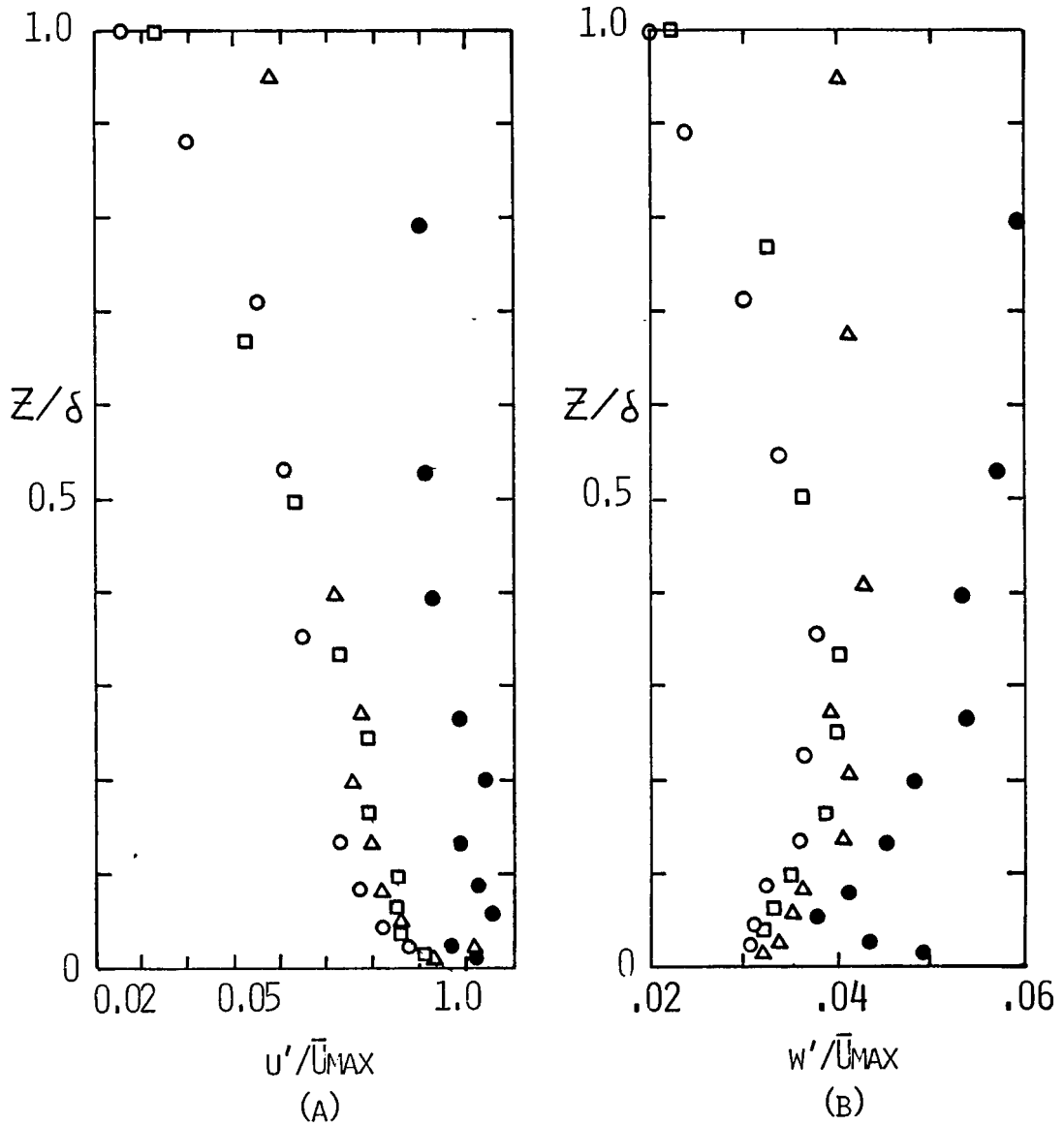


FIGURE 6.8.- BARRIER EFFECT ON TURBULENCE INTENSITIES.

SET	BAR. SIZE (IN)	SET	BAR. SIZE (IN)
○ 712-A	---	○ 711-A	---
□ 712-B	1.5	□ 703-B	1.5
△ 712-C	3.0	△ 711-B	3.0
		● 222	5.0

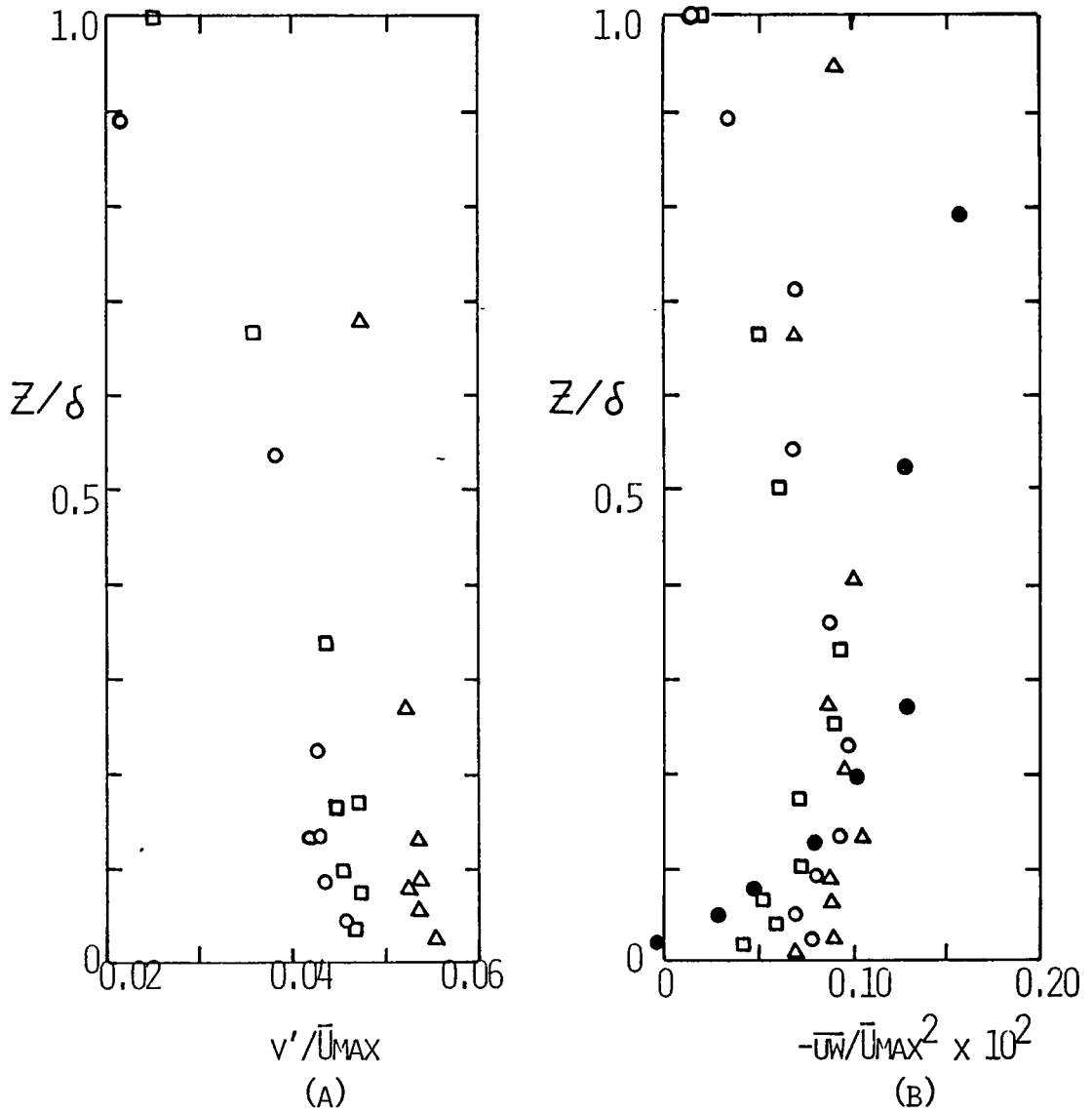


FIGURE 6.9.- BARRIER EFFECT ON LATERAL TURBULENCE INTENSITIES AND REYNOLDS STRESSES.

by the 5 in. barrier continue increasing even at values of $z/\delta \sim 1$. Both turbulence intensities and Reynolds stresses are expected to reach a maximum near the floor and then decrease as the full boundary layer height is approached which is consistent with the behavior of a flat plate boundary layer.

Because of this and the inflection point found in the velocity profile produced by the 5 in. barrier, this barrier will not be used in future work.

The effect of placing the 3 in. barrier at $x=3.66$ and 6.1 m on vertical and lateral turbulence intensities and Reynolds stresses is shown in Figure 6.10 a,b,c. When the barrier is placed at $x=3.66$ m, the turbulence intensities and Reynolds stresses change little, less than 5% between $x=9.5$ and 11.6 m. However, when the barrier is placed at $x=6.1$ m the change is considerable (approx. 15% decay).

It is concluded that placing the 3 in. barrier at $x=3.66$ m produces a flow that does not change appreciably in mean velocity, turbulence intensities or Reynolds stresses (\overline{uw}) between 9.7 and 11.6 m, i.e. the section that would be occupied by a model. However, considerable changes are observed when the barrier is placed at 6.1 m. In order to get a better picture of the flow field, the length scales corresponding to the longitudinal, vertical and lateral components of the velocity, i.e. $L_{u,x}$, $L_{w,x}$ and $L_{v,x}$, are shown in Figure 6.11 a and b. In this Figure, the length scales have been normal -

SET	X (m)	x (m)
○ 111	3.66	9.7
● 203-A	3.66	11.6
□ 204	6.10	9.7
■ 203-B	6.10	11.6

SET	X (m)	x (m)
○ 112	3.66	9.7
● 205-C	3.66	11.6
□ 205-A	6.10	9.7
■ 205-B	6.10	11.6

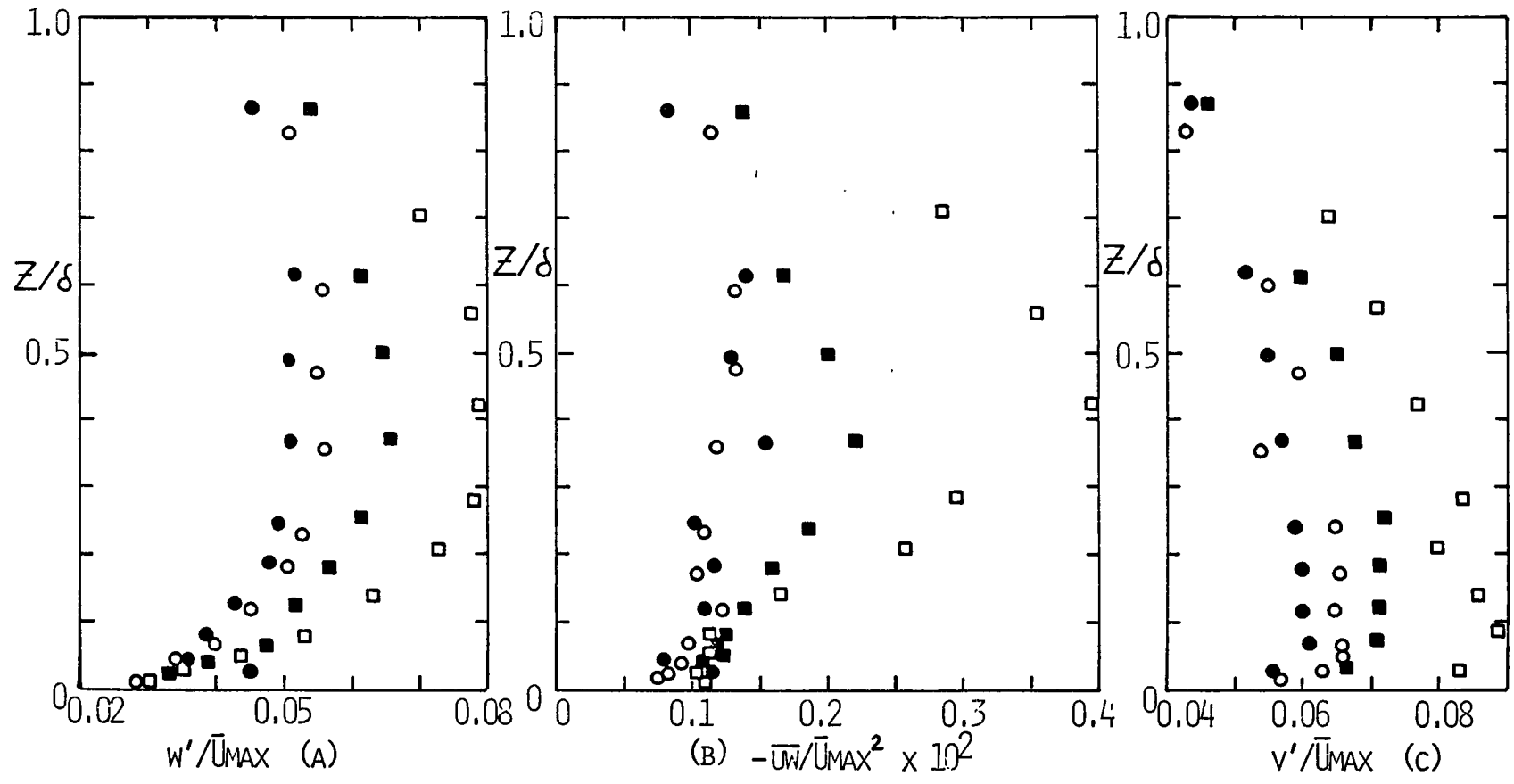
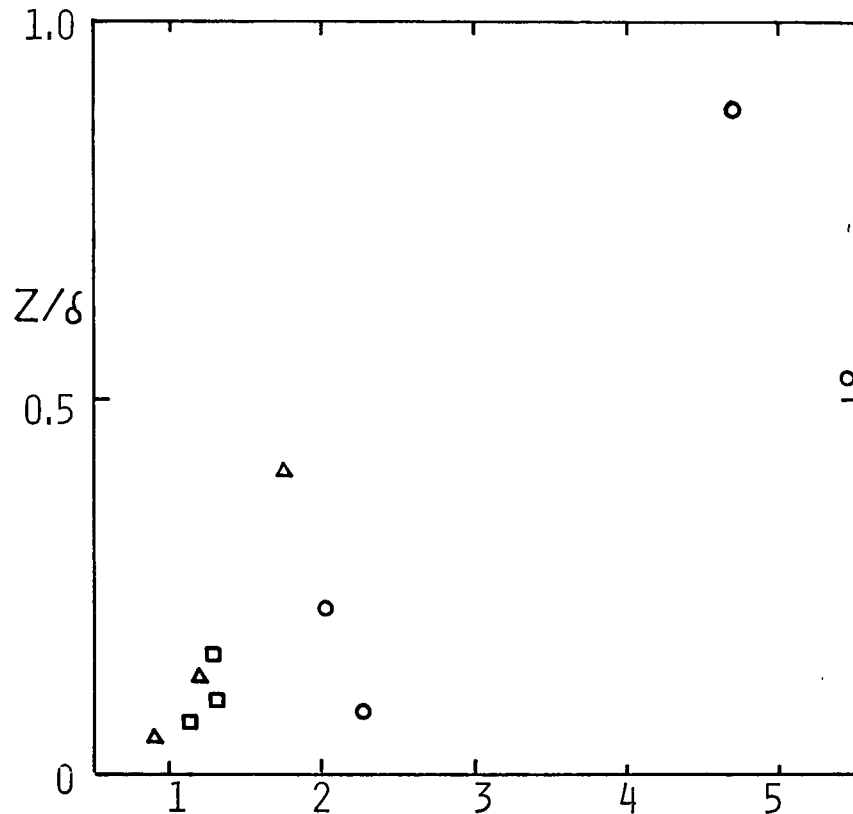


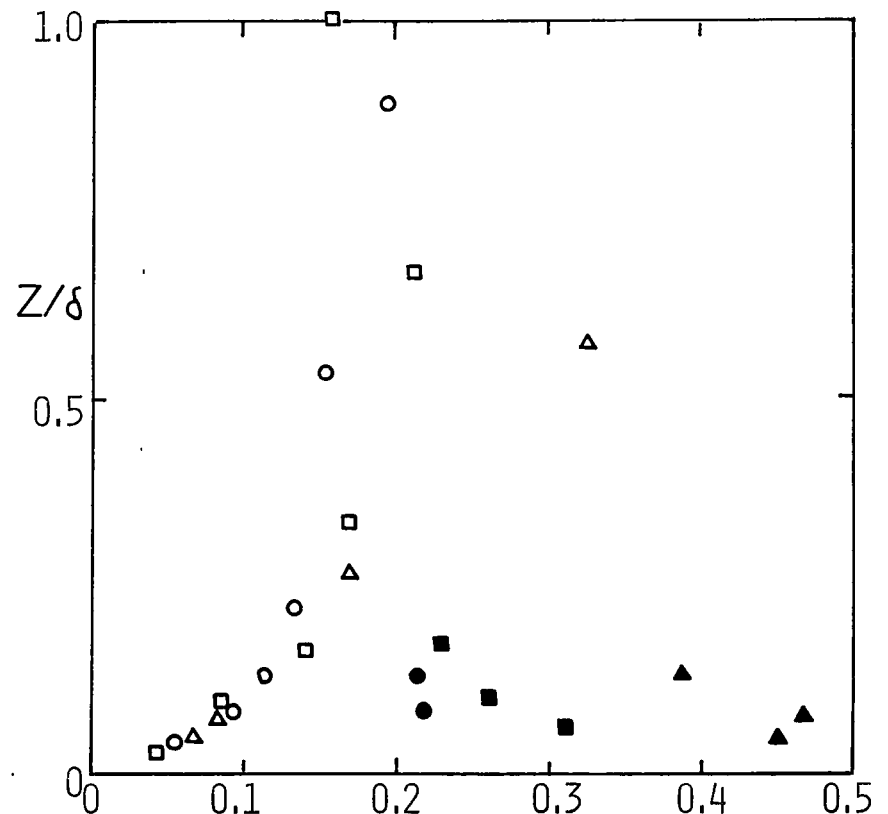
FIGURE 6.10.- EFFECT OF PLACING A 3" BARRIER AT A DISTANCE X ON TURBULENCE INTENSITIES AND REYNOLDS STRESSES.

SET	BAR. HEIGHT (IN)
○ 711-A	---
□ 703-B	1.5
△ 711-B	3.0

SET	$L_{w,x}$	$L_{v,x}$	BAR. HEIGHT (IN)
711-A 712-A	○	●	---
703-B 712-B	□	■	1.5
711-B 712-C	△	▲	3.0



$L_{u,x}/\delta$
(A)



$L_{w,x}/\delta$ OR $L_{v,x}/\delta$
(B)

FIGURE 6.11.- BARRIER EFFECT ON LENGTH SCALES.

ized by the boundary layer height .

The use of a barrier decreases the longitudinal length scale , approximately by a factor of 2 in the region $z/\delta < .25$, but the effect of using either a 1.5 or a 3 in. barrier is very similar . The vertical length scale is seen to be unaffected in the region $z/\delta < .25$ by the use of a barrier , but at $z/\delta > .25$ the use of a barrier increases its value . Only three values are available for the lateral length scale . These values cover only the bottom 1/5th of the boundary layer . Nevertheless it can be observed that by the use of a 3 in. barrier, the lateral length scales are doubled with respect to the case when no barrier is used . The effect of using the 1.5 in. barrier is moderate , the lateral length scales corresponding to this case in comparison with those obtained without barrier are slightly higher (15 %) .

In summary, the use of a barrier produces short longitudinal length scales and large vertical length scales in the upper 80 % of the boundary layer . Large lateral length scales are produced in the lower 20 % of the boundary layer .

Vortex Generators Effect.-

Vortex generators were used by Counihan (2) (14) (15) (16) with the purpose of diffusing outwards the high intensity turbulence produced by his rough wall in a short distance . The vortex generators employed in the present work are similar to those used by Counihan and are described in Chapter V .

Figure 6.12a shows that the vortex generators have no effect on the velocity profile at $x=10.9$ m with sand roughness surface and at $x=8.5$ with mesh roughness surface . Similarly, the longitudinal and vertical turbulence intensities plotted in Figures 6.12b and 6.13a , do not seem to be affected at these measuring points ($x= 8.5$ and 10.9 m) .

Mc Vehil (42) used a set of vortex generators slightly different from those used in this work . Mc Vehil reported that the vortex generators had no effect on mean velocity or longitudinal turbulence intensities , consistent with the above results .

The Reynolds stresses (\overline{uw}) are plotted in Figure 6.13b . The vortex generators produce a region close to the wall in which the product \overline{uw} goes to zero and even becomes positive . This phenomena is not consistent with boundary layer behavior.

It is concluded that the vortex generators used do not modify the mean velocity profile and turbulence intensities ; rather they produce undesired features , positive values of \overline{uw} . The vortex generators were not used further in the present work .

Cross-stream Horizontal Homogeneity .-

In this section , the two dimensionality of the approach flow is studied . Measurements of mean velocity , turbulence intensities and Reynolds stresses were taken at the tunnel centerline and at 95 cm from the centerline on both sides ,

SET	
●	321-A SAND + V.G.
○	307-D SAND
■	823-A MESH + V.G.
□	812-A MESH

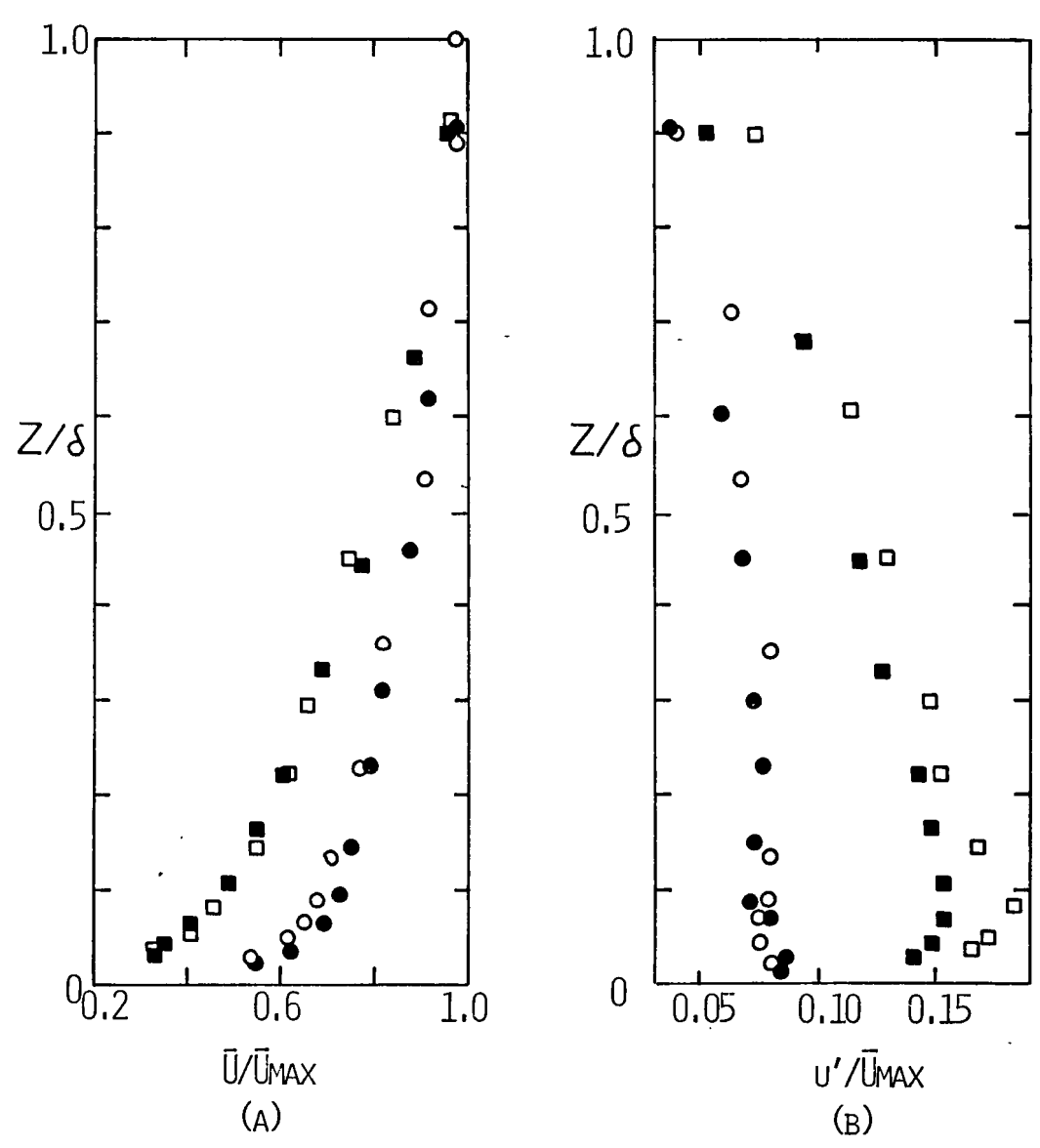


FIGURE 6.12.- VORTEX GENERATORS EFFECT ON VELOCITY PROFILE AND TURBULENCE INTENSITIES.

SET	
○	307-D SAND
○	321-A SAND + V.G.
□	812-A MESH
□	823-A MESH + V.G.

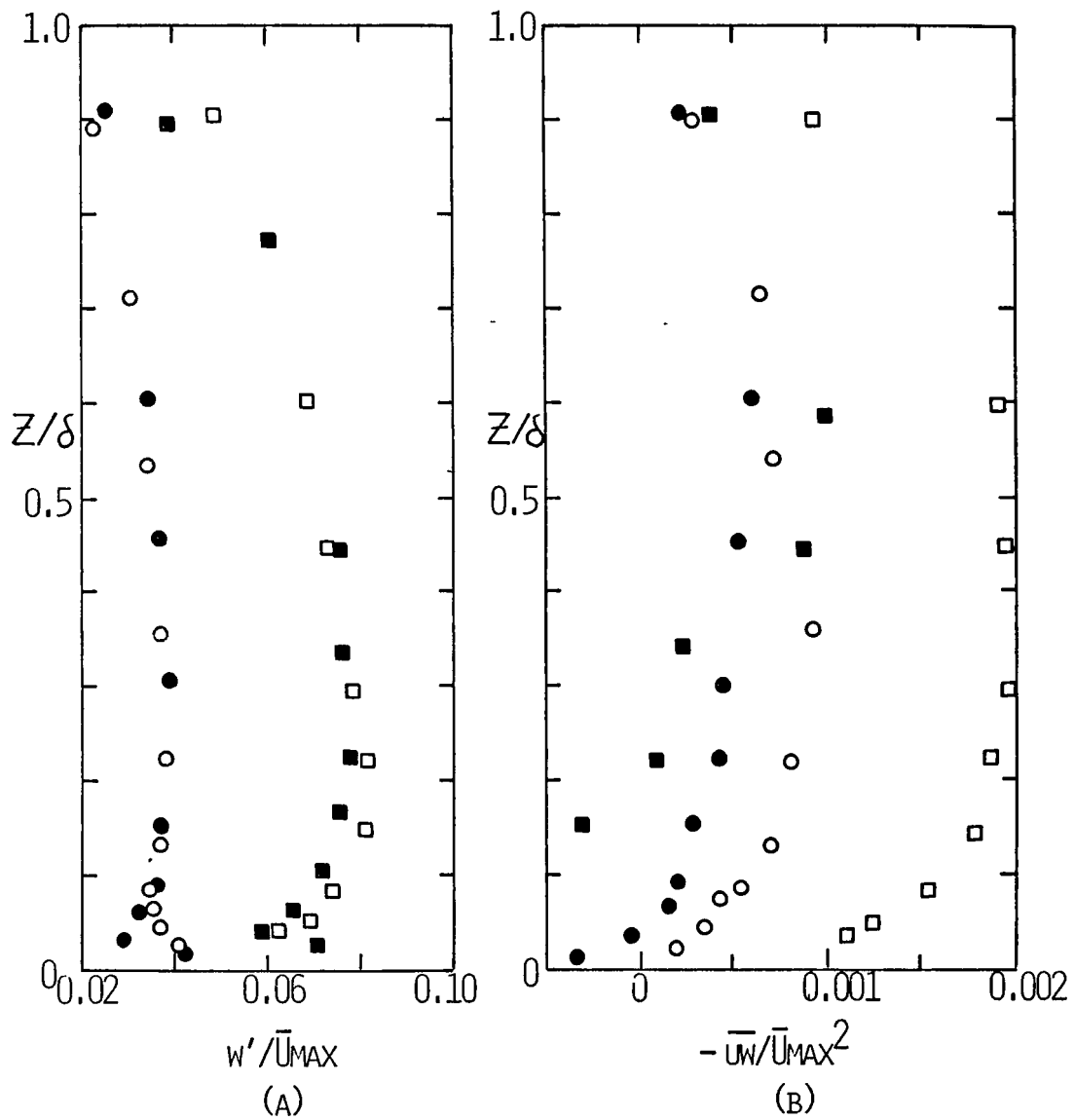


FIGURE 6.13.- VORTEX GENERATORS EFFECT ON VERTICAL TURBULENCE INTENSITIES AND REYNOLDS STRESSES (\bar{u}_w).

which is the maximum cross stream distance the probes can be placed due to the instruments carriage design . Positive values of the y coordinate are defined to the right of the centerline when it is observed going in the same direction as the mean wind flow . The measurements were taken for two configurations: sand roughness at x=8.5 m and sand roughness plus a 3 in . - barrier placed at 3.66 m from the beginning of the working section as measured at x=9.7 m.

Figures 6.14 a and b show the cross stream horizontal - homogeneity of the mean velocity for both configurations . For both cases the values for y=95 and -95 cm are off the centerline values by about 3 % . Therefore , the cross stream horizontal homogeneity of mean wind velocity can be regarded as satisfactory . Both the vertical and lateral turbulence intensities for the sand roughness case obtained at the centerline (Figure 6.15a) are 10 and 20 % higher than those obtained at y= -95 and 95 cm respectively . The vertical and lateral turbulence intensities for the sand roughness + 3 in.barrier at 3.66 m configuration are shown in Figure 6.15b . The cross-stream horizontal homogeneity is 5 % for the vertical and 5-10 % for the lateral . Since these differences are of the order of the estimated accuracy of the turbulence intensities, i.e. $\pm 10\%$, it is concluded that the cross stream horizontal homogeneity of turbulence intensities for both configurations studied is satisfactory .

SAND ROUGHNESS	
SET	Y (cm)
○ 108	0
□ 215-A	-95
△ 215-B	95

SAND + 3" BAR. AT X=3.66 m.	
SET	Y (cm)
○ 109	0
□ 215-C	95
△ 215-D	-95

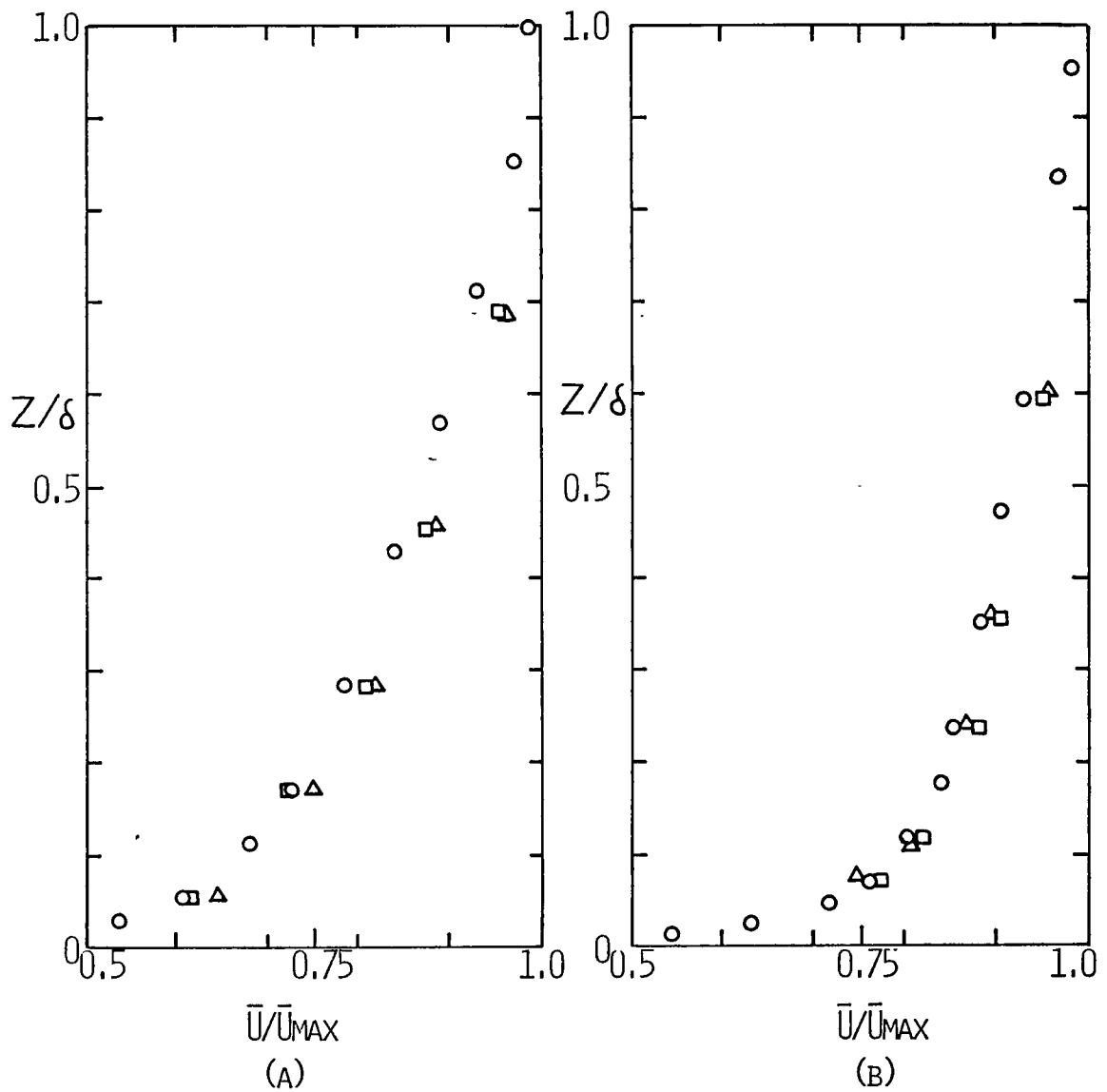


FIGURE 6.14.- MEAN VELOCITY PROFILE
CROSS-STREAM HORIZONTAL HOMOGENEITY.

SAND ROUGHNESS			
w'/U_{MAX}		v'/U_{MAX}	
SET	Y (cm)	SET	
○	628	0	● 115
□	215-A	-95	■ 216-A
△	215-B	95	▲ 216-B

SAND+3" BAR. AT X=3.66 m.			
w'/U_{MAX}		v'/U_{MAX}	
SET	Y (cm)	SET	
○	111	0	● 112
□	215-C	-95	■ 216-C
△	215-D	95	▲ 216-D

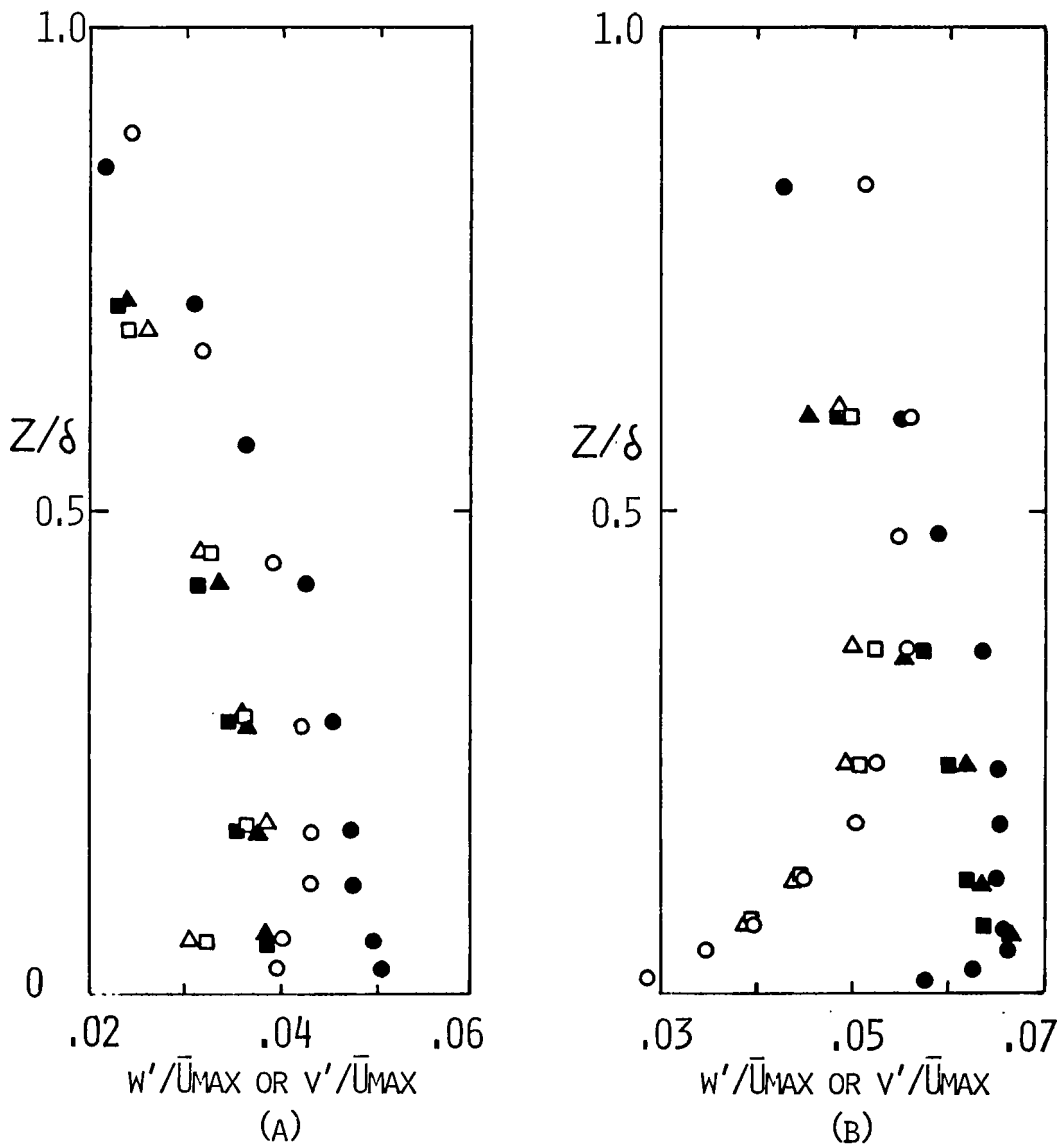


FIGURE 6.15.- TURBULENCE INTENSITIES.
CROSS-STREAM HORIZONTAL HOMOGENEITY.

SAND ROUGHNESS		
	SET	Y (cm)
○	628	0
□	215-A	-95
△	215-B	95

SAND + 3" BARRIER.		
	SET	Y (cm)
○	111	0
□	215-C	-95
△	215-D	95

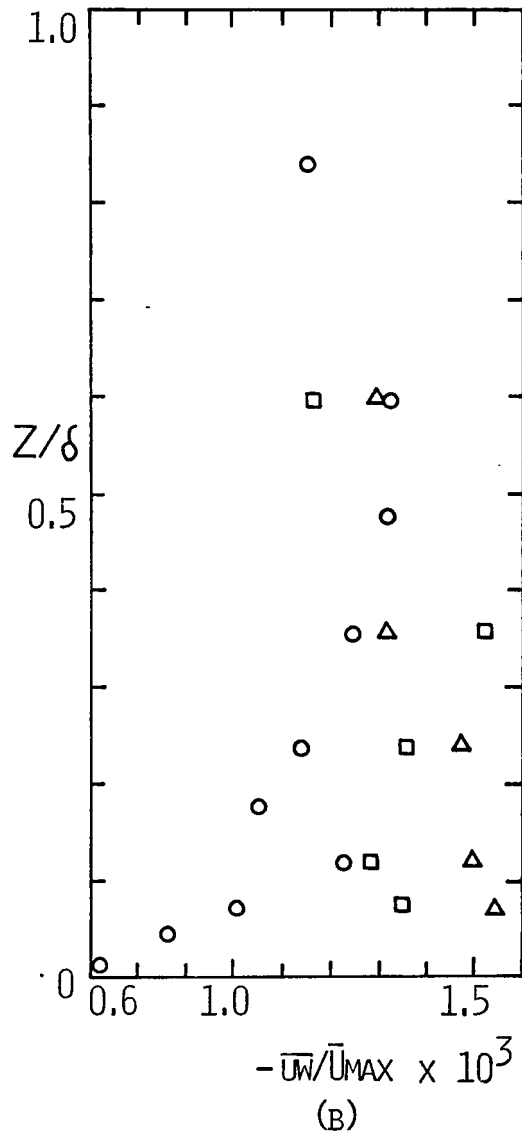
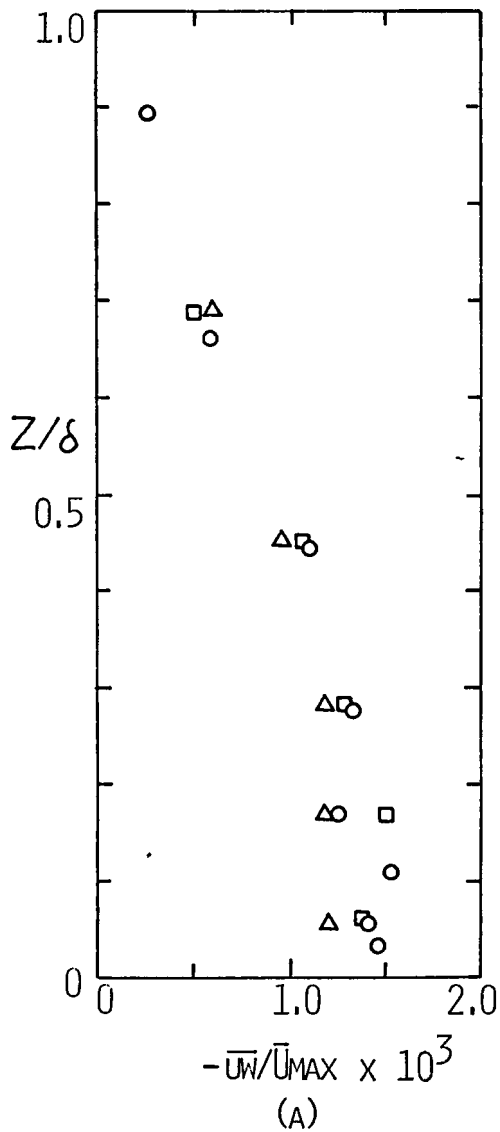


FIGURE 6.16.- REYNOLDS STRESSES
CROSS-STREAM HORIZONTAL HOMOGENEITY.

The cross-stream horizontal homogeneity of the Reynolds stresses (\overline{uw}) values are presented in Figures 6.16 a and b . Variations of $\pm 20\%$ and $\pm 15\%$ are found for the sand roughness and sand roughness + barrier respectively . These variations are also within the estimated accuracy of the \overline{uw} values ($\pm 20\%$) , and therefore, the cross-stream horizontal homogeneity of the Reynolds stresses for both configurations is satisfactory .

It is concluded from the results presented in this section that: (1) the sand and mesh roughness floor configurations are capable of producing flows characteristic of the neutral rural and urban A B L respectively ;(2) the smooth surface may be used to produce stable flows and (3) the 3 inches barrier placed at 3.66 m over sand roughness produces a large scale flow characteristic of unstable atmospheric flows . These configurations are tested in detail in the next section .

Simulation of Atmospheric Flows

The objective of this work is the simulation of the A B L under various stabilities. The last section has provided information about the flow characteristics obtainable in the UHEWT. This information is used in parallel with the information on the A B L description to select the configurations (kind of floor, barrier height, etc.) which are potentially useful for the development of the desired flow characteristics. In order

to evaluate the simulation , the wind tunnel data will be compared to A B L flow characteristics and analyzed under the criteria developed in Chapter IV (present's work simulation approach) . For this purpose, values of the turbulence intensities referred to the local mean velocity , energy spectrum and length scales corresponding to various configurations will be presented and discussed below .

Tables 3.1 and 3.2 will be used to compare the turbulence intensities from the wind tunnel and the A B L Pasquill stability categories in order to evaluate stability . Henceforth, the comparison of the energy spectra will be done against the A B L energy spectra reported by Kaimal, et al. (35) unless specifically stated otherwise .

Neutral Stability Simulation

The sand roughness and mesh roughness floors were selected as developing flows typical of the neutral rural and urban A B L . Using a scale of 1:1000 , the length scale for the sand roughness is typical of rural terrain , whereas the length scale for the mesh roughness is typical of urban terrain . The equilibrium and two-dimensionality of sand roughness approach flows have already been discussed in the last section . Equilibrium for the mesh roughness approach flow was also shown . The case where a 1.5 in. barrier was placed 0.6 m before the beginning of the working section , the working section being covered by sand roughness , will also be investigated .

Figure 6.17 shows the turbulence intensities referred to the local mean velocity in the lower third of the boundary layer . The vertical turbulence intensity for those cases intended to simulate the rural terrain does not change appreciably with height . The sand roughness + 1.5 in.barrier configuration produces a lateral turbulence intensity that does not change appreciably with height . Both of these observations are in agreement with Slade (65) . However , the lateral turbulence intensity for the sand roughness configuration changes appreciably with height in disagreement with Slade (65) . Trends for the variation of turbulence intensities with height for urban terrain have not been reported in the literature .

In Table 6.3 , the range of values for turbulence intensities in the lower third of the boundary layer are presented. The estimated Pasquill stability categories obtained by comparison with A B L values (Tables 3.1 and 3.2) are indicated in parenthesis .

TABLE 6.3
TURBULENCE INTENSITIES IN THE LOWER THIRD
OF THE BOUNDARY LAYER.NEUTRAL SIMULATION.

SET	CONFIGURATION	u'/\bar{U}	v'/\bar{U}	w'/\bar{U}	$-\overline{uw}/\bar{U}_\infty^2$	$-\overline{uw}/u'w'$
628 115	Sand Roughness (S.R.)	.11-.19 (D)	.06-.10 (D-E)	.06-.08 (D)	.0014 - -	.344 - -
703-B	S.R.+1.5 in.barrier	.09-.15 (D-E)	.05-.08 (E)	.05 (E)	.0008 - -	.248 - -
812-A	Mesh Roughness (M.R.)	.21-.45 (D-Urban)	.13-.25 - -	.11-.17 (D-Urban)	.0014 - -	.132 - -

u'/\bar{U}	w'/\bar{U}	v'/\bar{U}	SET	CONFIGURATION.
○	□	△	628/115	SAND
	■	▲	812-A/814	MESH
φ	φ	⋈	703-B/712-B	SAND + 1.5" BAR.

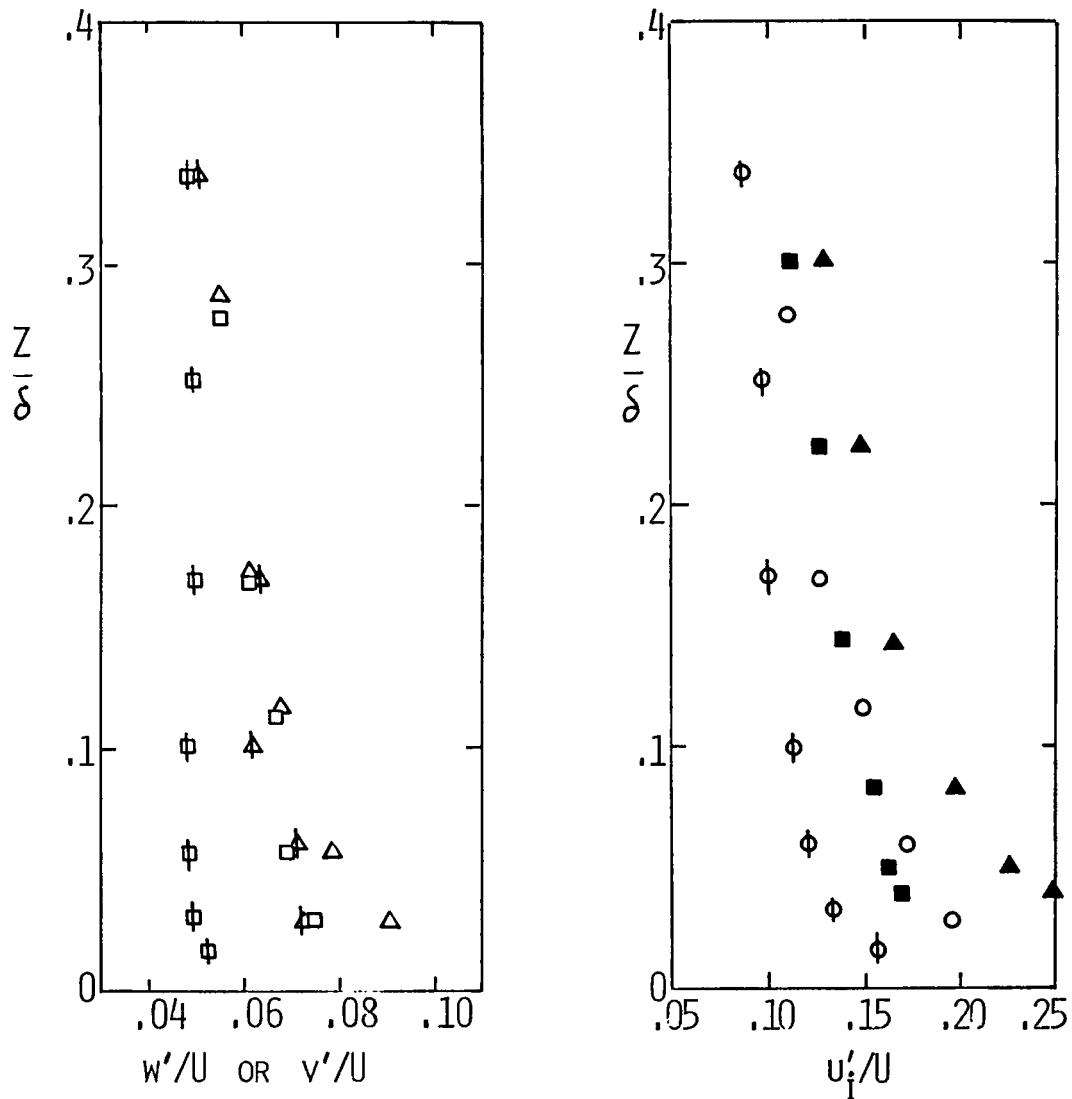


FIGURE 6.17.- NEUTRAL ATMOSPHERE SIMULATION.
TURBULENCE INTENSITIES.

The simulated Reynolds stresses for the three cases as compared against Counihan (17), e.g. $.002 < \overline{uw}/\bar{U}_w^2 < .0025$, are low. But the cross correlation coefficient $\overline{uw}/u'w'$ is comparable to those reported by Haugen, et al. (24).

The vertical turbulence component energy spectrum for the three configurations: sand roughness, sand roughness+1.5 in. barrier and mesh roughness is given in Figure 6.18. All energy spectra reported in this section have been measured at values of z/δ in the surface layer comparable to the A B L energy spectrum reported by Kaimal, et al. (35), e.g. $z/\delta \approx 0.1$.

The vertical energy spectrum for the sand roughness case agrees well with the neutral ($z/L=0$) A B L energy spectrum. The energy spectrum for the case of sand roughness + 1.5 in. barrier is shifted upwards from the A B L neutral energy spectrum showing a very similar shape. Since the vertical turbulence intensity for this case was below the neutral A B L values this upwards shift may be due to an underestimation of u_* . The vertical velocity energy spectrum for the mesh roughness case is in fair agreement with the neutral rural A B L energy spectrum. In the absence of reported urban A B L energy spectrum, it will be assumed here as others have done, e.g. Counihan, (16); Teunissen, (79), (80), that the urban neutral A B L energy spectrum is similar to the corresponding rural one.

Figure 6.19 shows the lateral component energy spectrum for the three configurations studied. The agreement between

SET	Z/δ	CONFIGURATION.
○ 628	.167	SAND
● 628	.056	SAND
□ 703-B	.167	SAND + 1.5" BAR.
■ 703-B	.100	SAND + 1.5" BAR.
△ 812-A	.159	MESH
▲ 812-A	.069	MESH

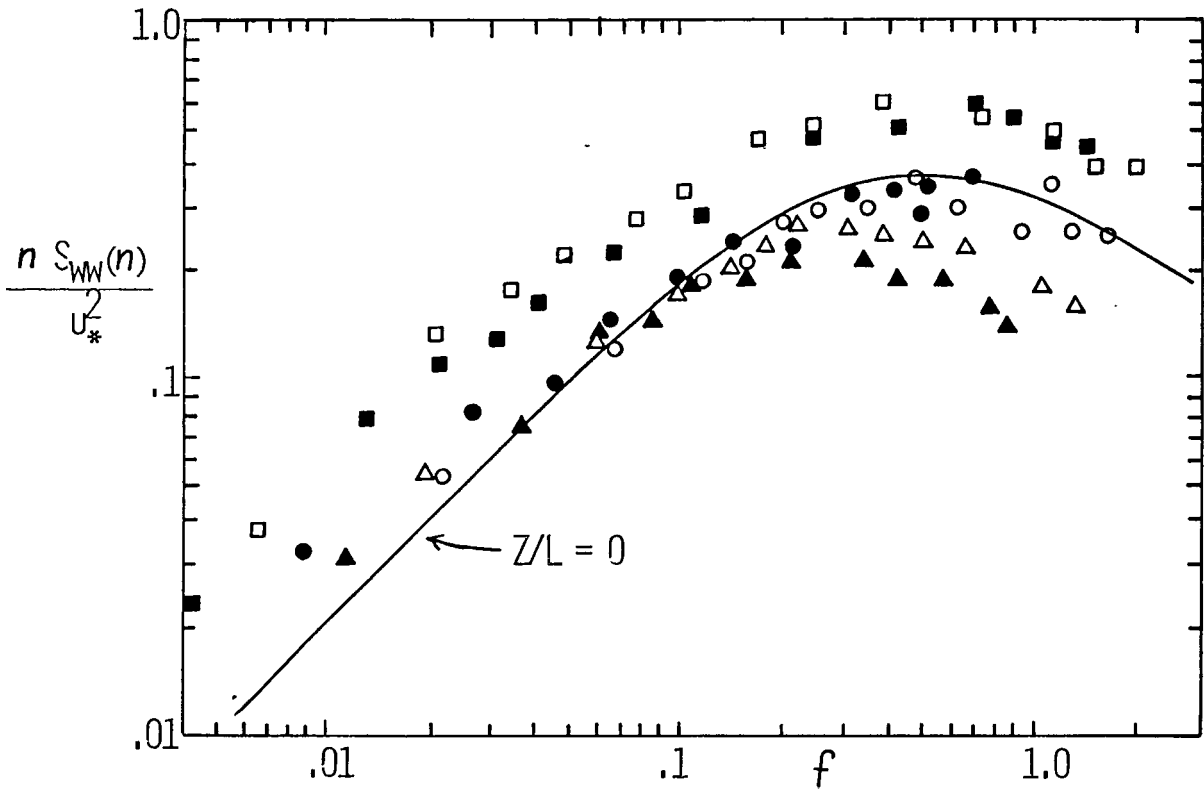


FIGURE 6.18.- NEUTRAL ATMOSPHERE SIMULATION.
VERTICAL VELOCITY ENERGY SPECTRUM.

	SET	Z/δ	CONFIGURATION
○	115	.171	SAND
●	115	.114	SAND
□	712-B	.167	SAND + 1.5" BAR.
■	712-B	.100	SAND + 1.5" BAR.
△	814	.159	MESH
▲	814	.069	MESH

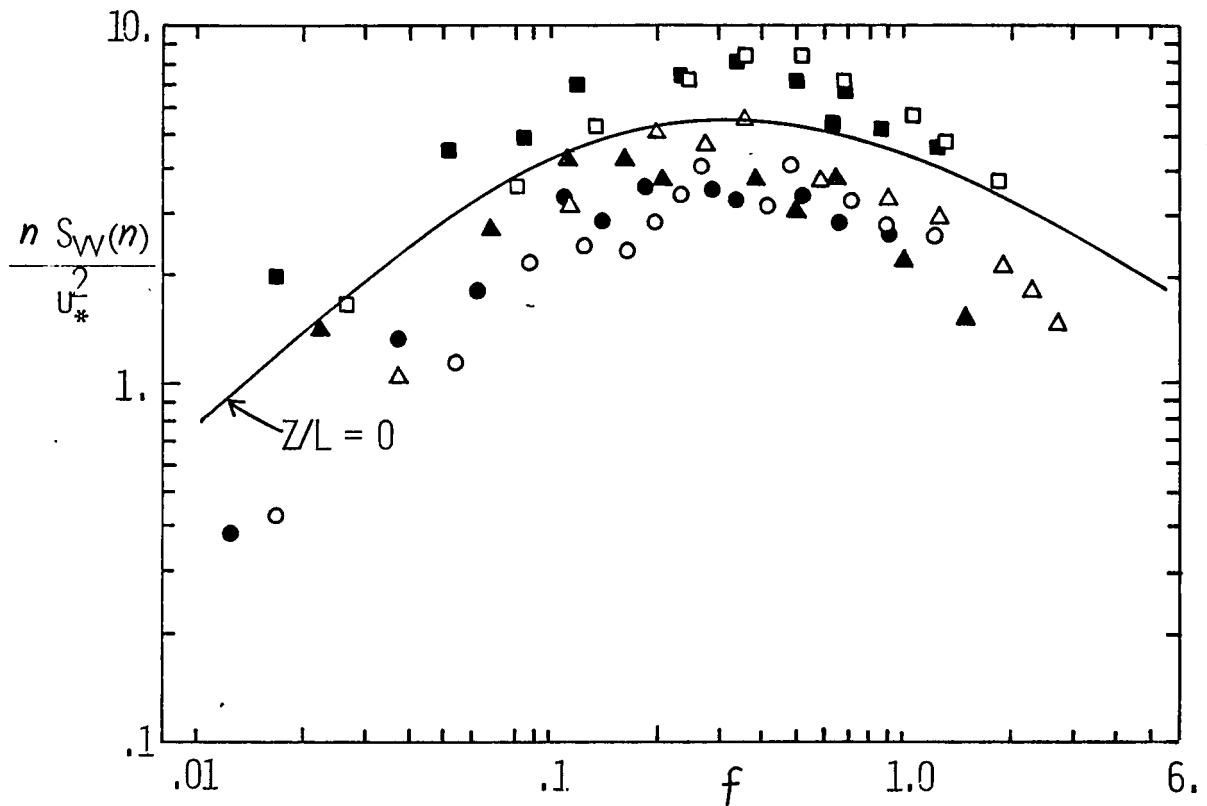


FIGURE 6.19.- NEUTRAL ATMOSPHERE SIMULATION,
LATERAL VELOCITY ENERGY SPECTRUM.

the sand roughness lateral energy spectrum and the Kaimal, et al. (35) energy spectrum is fair . The shape is similar , but it is shifted downwards by approximately 50 % . The agreement for the sand roughness + 1.5 in. barrier is also weak . The shape is similar but it is shifted upwards . Again , poor estimated values of u_* may have caused this shift in data . The mesh roughness energy spectrum compares fairly well with the neutral rural A B L energy spectrum .

The vertical and lateral length scales $L_{w,x}$ and $L_{v,x}$ are shown in Figure 6.20 . The comparison of this work's experimental values is done against those proposed by Teunissen (78) and Pasquill (56) for the neutral A B L . Such comparison has to be rather qualitative , but the analysis of the energy spectrum shape helps such an analysis due to the relationship existing between the length scale and the energy spectrum shape (Pasquill, (55)) .

The vertical length scales normalized by the boundary layer height are very similar for the three configurations and follow the trend proposed by Pasquill (56) , and Teunissen (78) for the neutral A,B L . The fact that they become approximately constant for $z/\delta > 0.3$ is consistent with both Lumley and Panofsky (40) and Kaimal and Haugen (34) .

The lateral length scale is approximately constant with height for the sand roughness configuration . For the mesh - roughness and sand roughness + 1.5 in. barrier configurations

$L_{w,x}$	$L_{v,x}$	SET	CONFIGURATION.
○	□	628/115	SAND
●	■	812-A/814	MESH
φ	⊕	703-B/712-B	SAND + 1.5" BAR.

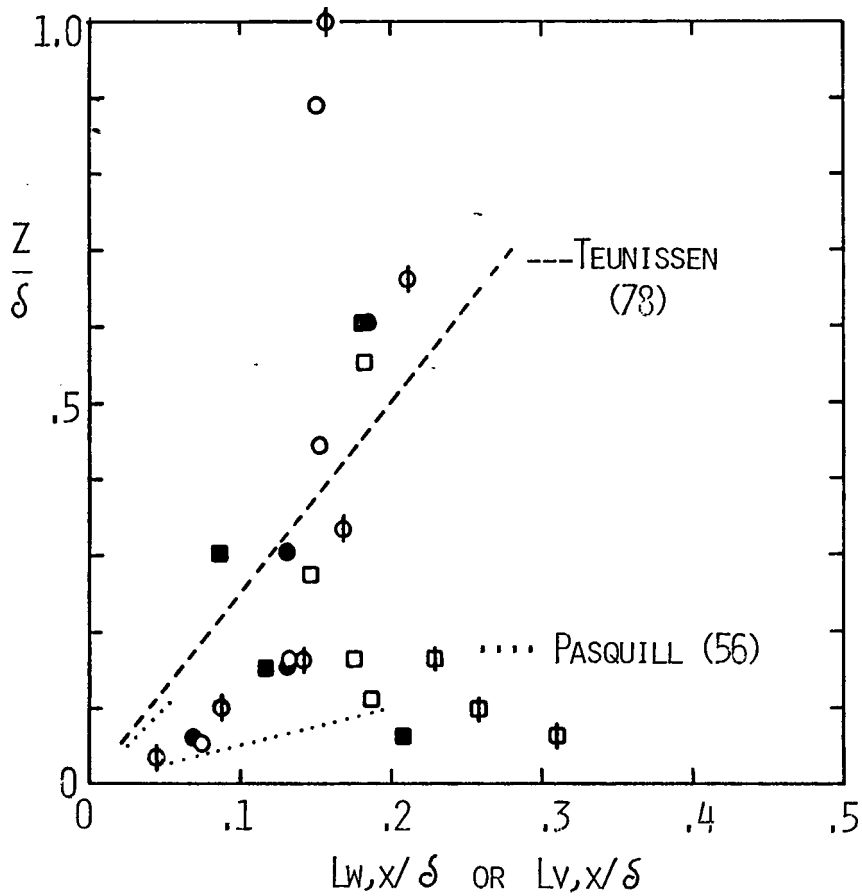


FIGURE 6.20.- NEUTRAL ATMOSPHERE SIMULATION.
VERTICAL AND LATERAL LENGTH SCALES.

it appears that $L_{v,x}$ tends to decrease with height which is in agreement with Busch, et al. (6) . The mean velocity for the sand roughness and mesh roughness configurations have been plotted in Figure 6.1 . The corresponding power law exponents are typical of rural and urban flows respectively . The Law of the Wall and Velocity Defect Law for these two configurations were plotted in Figure 6.2 and 6.3 respectively . The mean velocity for the configuration sand roughness + 1.5 in. barrier has been plotted in Figure 6.7 (a) showing that its power law exponent is typical of rural flows .

A summary of the evaluation of turbulence intensities , energy spectrum and length scales for the proposed configurations is given in Table 6.8 . The evaluation of stability category was undertaken in the most quantitative way possible . However, due to poor A B L length scale values and sometimes due to inconsistencies between the wind tunnel simulation values, e.g. E stability category turbulence intensities with a D stability category energy spectrum and length scales , judgement based on Taylor's equation (2.94) was applied in order to reach a compromise .

It is concluded that the sand roughness produces a flow characteristic of the neutral rural A B L ; the mesh roughness produces a flow with the characteristics of the urban neutral A B L and the sand roughness + 1.5 in. barrier configuration produces a flow corresponding to a D-E Pasquill stability cat-

egory, that is neutral/slightly stable . However , in this last configuration the sand roughness covered the working section up to $x=8.5$ m and from thereon the surface was smooth . The measurements were taken at $x=10.9$ m . It is believed that if the test section was also covered by sand roughness , the turbulence intensities would be high enough to fall into the neutral category and thus , all measurements would support a neutral (D) simulation .

Simulation of the Stable Atmosphere

The sand and mesh roughness floors produced flows typical of the neutral rural and urban A B L . Since in principle , the turbulence intensities obtained with the smooth floor are lower than those obtained with rough floors , a smooth floor should produce flows characteristic of the stable atmosphere .

Three free stream velocities were used over the smooth surface : ~ 6 , ~ 2 and $\sim .7$ m/s . It has already been noted that the measurements taken at velocities smaller than 1 m/s are not as reliable as those velocities larger than 2 m/s . The measurements at a free stream velocity of ~ 2 m/s produce identical results to those having a free stream velocity of ~ 6 m/s therefore giving credibility to the former data . However , the results using a free stream velocity of $\sim .7$ m/s have some features that make them unreliable .

An important characteristic of stable flows is the small length scale of vertical motions . A 1/4 in. square grid and a

32 mesh grid were put at $x=8.5$ m , normal to the mean flow and extending from $z=0$ to a height of approximately 30 cm (higher than the expected boundary layer) . This was intended to reduce both the turbulence intensities and the vertical length scale as measured at $x=10.9$ m . The peak on the vertical energy spectrum would then move towards higher frequencies in agreement with stable A B L energy spectrum .

Equilibrium of flows over a smooth floor has already been shown as well as cross-stream horizontal homogeneity of the flow over sand roughness surface . It is expected that the cross - stream horizontal homogeneity of the flow over smooth surface is also good .

The measured turbulence intensities referred to the local mean velocity for smooth floor and smooth floor + screen configurations in the lower third of the boundary layer are given in Figure 6.21 . The measured vertical turbulence intensities for smooth floors for free stream velocities of ~ 0.7 and ~ 6 m/s decrease with height up to $z/\delta \sim 0.1$ and thereafter become nearly constant , while those for the free stream velocity of ~ 2 m/s increase with height up to $z/\delta \sim 0.1$ and thereafter become constant . According to Slade (65) , the A B L vertical and lateral turbulence intensities decrease with height .The use of a 1/4 in. square grid screen produces vertical turbulence intensities slightly decreasing with height , while the 32 mesh screen vertical turbulence intensities decrease considerably with height.

u'/\bar{U}	w'/\bar{U}	v'/\bar{U}	SET	CONFIGURATION.
\ominus	\oplus		1120	SMOOTH + $\frac{1}{4}$ " GRID AT 8.5 M
\ominus	\oplus		1125	SMOOTH + 32 MESH GRID "
\circ	\square	\triangle	1012-A/1121	SMOOTH (6 m/s)
\bullet	\blacksquare	\blacktriangle	1016-A/1022-A	SMOOTH (2 m/s)
ϕ	ϕ	\blacklozenge	1016-B/1022-B	SMOOTH (.7 m/s)

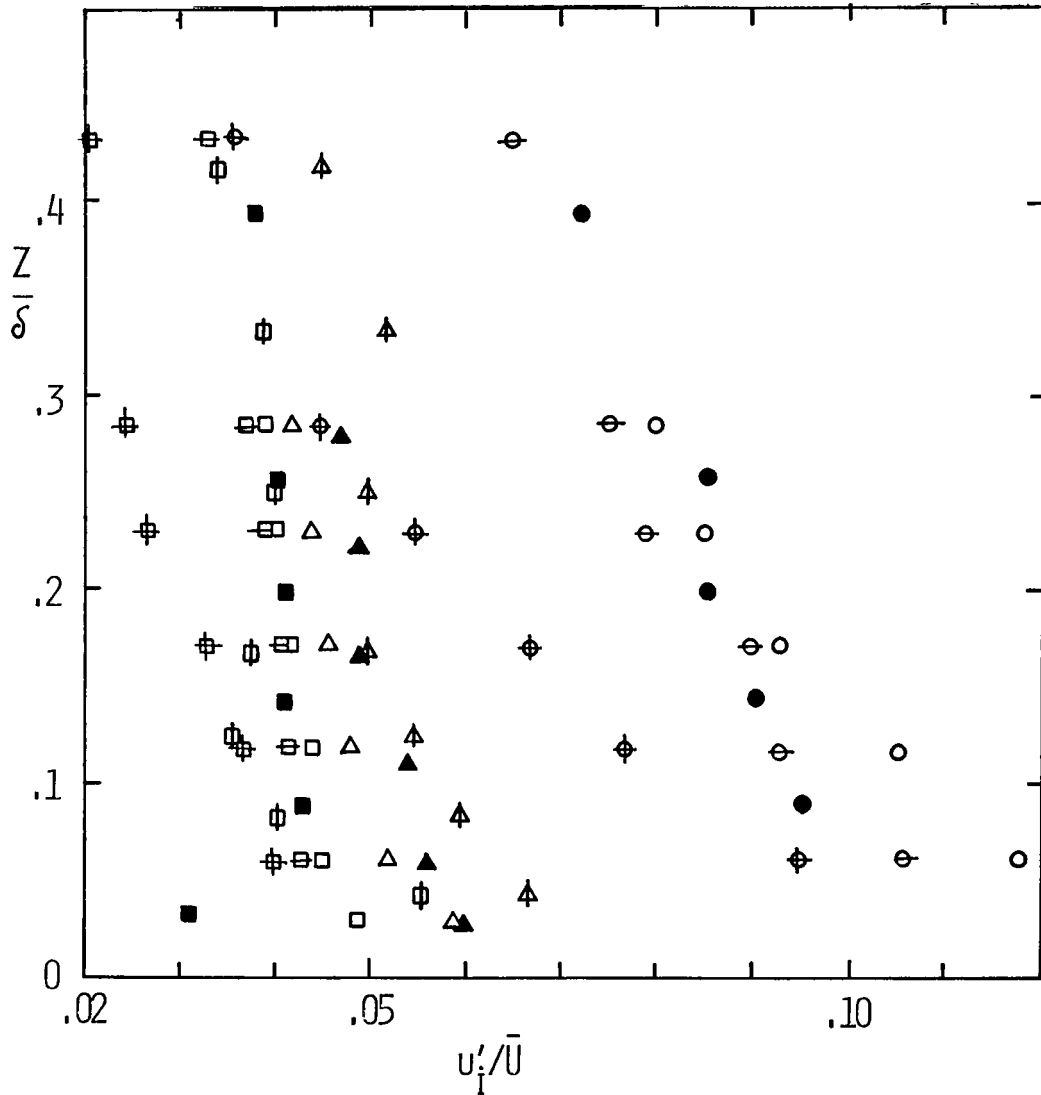


FIGURE 6.21.- STABLE ATMOSPHERE SIMULATION.
TURBULENCE INTENSITIES.

The lateral turbulence intensities produced by the smooth floor configuration for the free stream velocities of ~ 6 m/s, ~ 2 m/s and $\sim .7$ m/s decrease with height . The longitudinal turbulence intensities are plotted for completeness .

The range of values of turbulence intensities for each particular configuration in the lower third of the boundary layer is shown in Table 6.4 , the estimated Pasquill stability category determined by comparison with Table 3.1 is given in parenthesis .

TABLE 6.4
TURBULENCE INTENSITIES IN THE LOWER THIRD
OF THE BOUNDARY LAYER. STABLE SIMULATION.

SET	CONFIGURATION	u'/\bar{U}	v'/\bar{U}	w'/\bar{U}	$- uw / \bar{U}_\infty^2$
1012-A 1121	Smooth Surface \bar{U} 6 m/s	.08-.14 (D-E)	.04-.06 (E-F)	.04-.05 (E)	.00045 - -
1016-A 1022-A	Smooth Surface \bar{U} 2 m/s	.08-.13 (D-E)	.04-.06 (E-F)	.04-.05 (E)	.0008 - -
1016-B 1022-B	Smooth Surface \bar{U} .7 m/s	.09-.25 (D)	.05-.07 (E)	.04-.06 (E)	negative! - -
1120	Smooth+1/4 in. square grid	.08-.12 (D-E)	- -	.035-.045 (E-F)	.0003 - -
1125	Smooth+32 mesh grid .	.05-.11 (E)	- -	.025-.045 (F)	.0002 - -

It is noted in this Table that positive Reynolds stresses

\overline{uw} were found for the case having a free stream velocity of ~ 7 m/s . Since \overline{uw} values should be negative , these values are considered as unreliable .

Figure 6.22 shows the vertical energy spectrum for the - smooth surface and smooth surface + screen configurations .The vertical energy spectrum for the smooth surface with a free stream velocity of approx. 6 m/s has a shape similar to the neutral A B L vertical energy spectrum but it is shifted downwards . When the free stream velocity is ~ 2 m/s the shape is similar to the one for the higher free stream velocity of ~ 6 m/s , reaching the maximum at approximately the same value of $f=nz/\overline{U}$, but then it decreases much faster as f increases , showing a small inertial subrange . This was to be expected since the width of the inertial subrange is proportional to the Reynolds number .

The vertical energy spectrum for the free stream velocity of ~ 0.7 m/s has a shape not similar to the neutral and is shifted much downwards from the neutral A B L energy spectrum .

In Figure 6.22 , the energy spectrum for slightly stable conditions ($z/L=0.3$) is also plotted . None of the smooth surface vertical energy spectrum has its maximum displaced towards higher values of "f" than for the neutral stability spectrum . The addition of a screen upstream from the measurement point (at $x=8.5$ m) was taken with the purpose of breaking the scale of the motion so that the maximum of the spectrum moved to

SET	Z/δ	CONFIGURATION.
□	.171	SMOOTH + ¼" GRID AT 8.5 M
△	.114	SMOOTH + 32 MESH GRID "
○	.171	SMOOTH
●	.114	SMOOTH
⊕	.089	SMOOTH ($\bar{U}_\infty \sim 2$ M/s)
+	.125	SMOOTH ($\bar{U}_\infty \sim .7$ M/s)

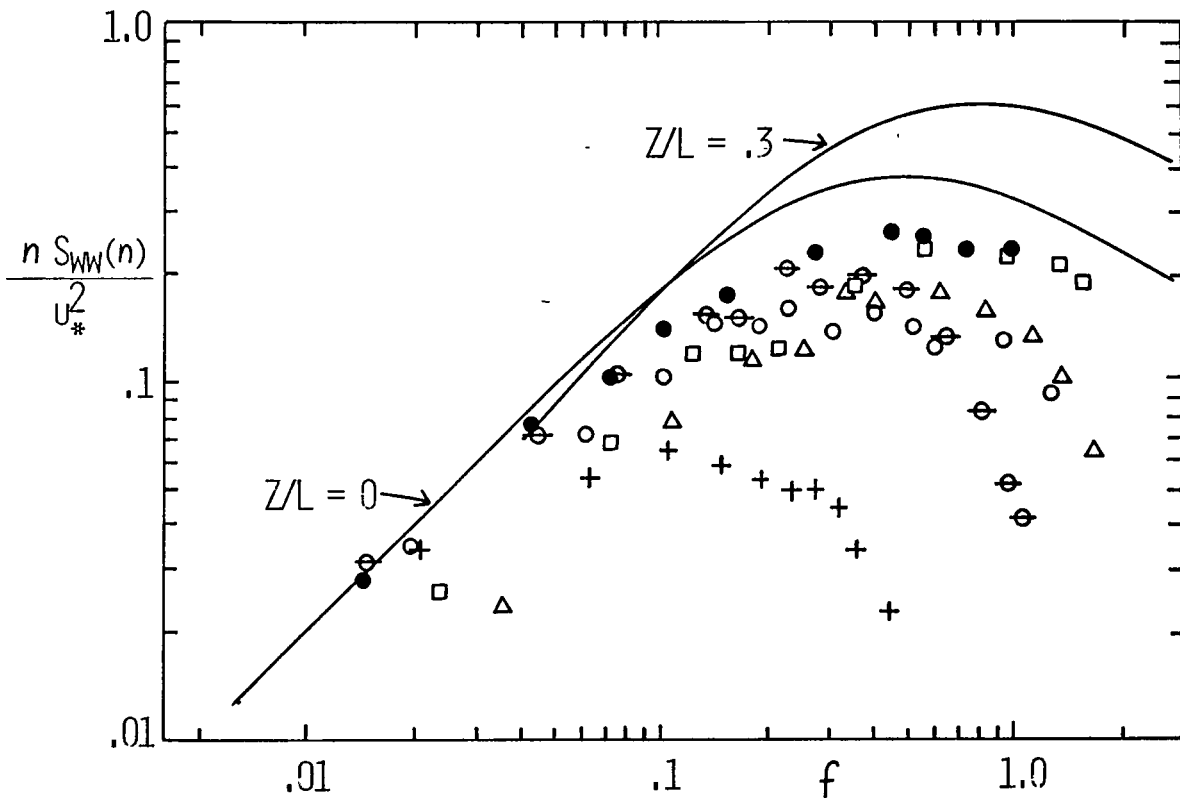


FIGURE 6.22.- STABLE ATMOSPHERE SIMULATION.
VERTICAL VELOCITY ENERGY SPECTRUM.

a higher value of "f" . However , the resulting energy spectrum is still similar to that of the neutral A B L .

The value of u_* / \bar{U}_∞ requires special attention when trying to develop stable flows . The value of u_* / \bar{U}_∞ should decrease with increasing stability (this is why the energy spectrum for $z/L=0.3$ looks above the neutral eventhough the amount of turbulent energy,proportional to the turbulence intensity is lower), but u_* being a function of the roughness length can not be decreased to a lower value than for the smooth floor value by only mechanical means .

The lateral spectrum for the smooth surface flows is plotted in Figure 6.23 and compared to the neutral and slightly stable energy spectrum . The observations are essentially the same as for the corresponding vertical energy spectrum , namely that for free stream velocities of ~ 6 and ~ 2 m/s the shapes are similar and shifted downwards from the neutral A B L energy - spectrum and that for the latter there is not appreciable inertial subrange .

The vertical and lateral length scales $L_{w,x}$ and $L_{v,x}$ for the stable simulation runs are plotted in Figure 6.24 . The vertical length scale $L_{w,x}$ is very similar for the smooth surface configuration at free stream velocities of approximately 6 and 2 m/s . Also slightly smaller values were obtained by the use of a screen . The vertical length scale,at a given - height , decreases with increasing stability (Pasquill,(56)).

SET	Z/δ	CONFIGURATION
○ 1121	.114	SMOOTH (U _∞ ~ 6 m/s)
● 1022	.056	SMOOTH (U _∞ ~ 2 m/s)
+ 1024	.125	SMOOTH (U _∞ ~ .7 m/s)

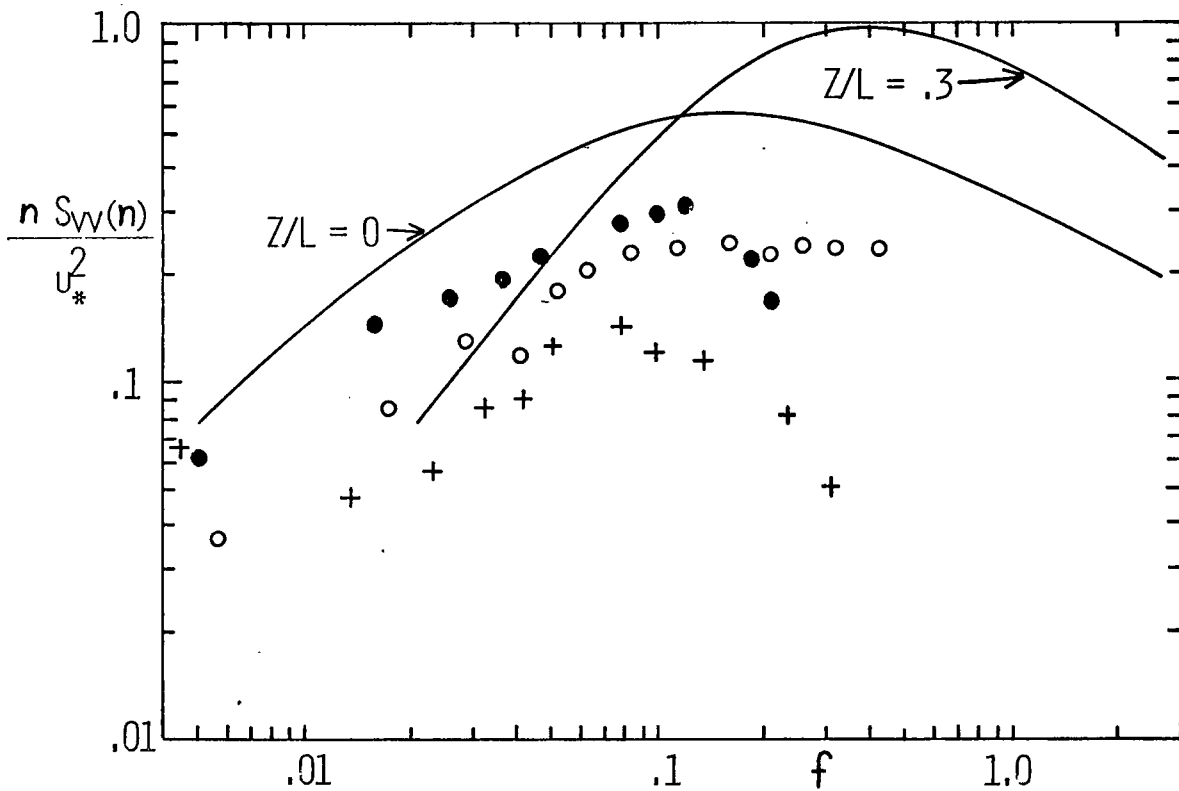


FIGURE 6.23.- STABLE ATMOSPHERE SIMULATION.
LATERAL VELOCITY ENERGY SPECTRUM.

$L_{w,x}$	$L_{v,x}$	SET	CONFIGURATION.
⊖		1120	SMOOTH + ¼" GRID AT 8.5 M
●		1125	SMOOTH + 32 MESH GRID "
○	□	1012-A/1121	SMOOTH ($\bar{U}_\infty \sim 6$ M/s)
+		1127-A	SMOOTH ($\gamma = .95$ M)
×		1127-B	SMOOTH ($\gamma = -.95$ M)
⊕	⊕	1016-A/1022-A	SMOOTH ($\bar{U}_\infty \sim 2$ M/s)

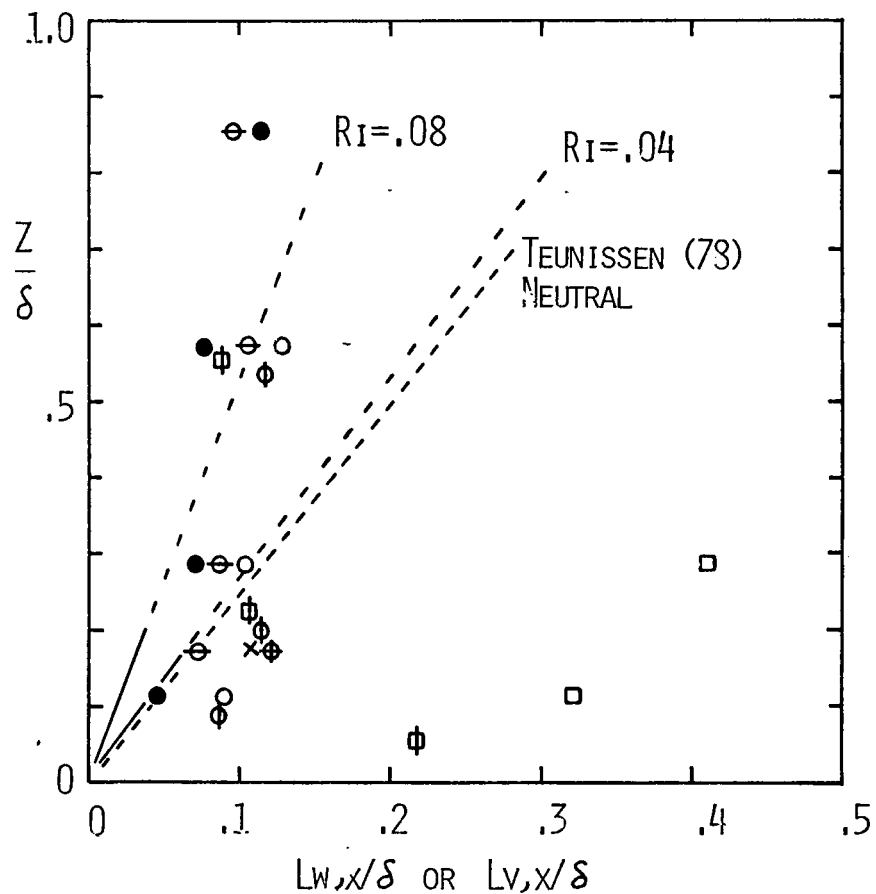


FIGURE 6.24.- STABLE ATMOSPHERE SIMULATION.
VERTICAL AND LATERAL LENGTH SCALES.

The proposed A B L vertical length scales for neutral stability (Teunissen, (78)) and those proposed by Kaimal (33) for the stable atmosphere ($Ri=0.4$ and 0.8) are plotted in Figure 6.24 for comparison . Recall that the Kaimal's values hold up to a height of 22.5 m .

For $z/\delta < 0.3$ the wind tunnel values fall either in the - region of neutral A B L values or in the boundary between neutral and stable ones . For $z/\delta > 0.3$ the simulated $L_{w,x}$ are nearly constant with height and in the range of stable A B L values . Note that these $L_{w,x}$ values are approximately 1/3 smaller than those for the neutral simulation of Figure 6.20 . The cross-stream uniformity of the $L_{w,x}$ is very good as shown by the closeness of the three values taken at $y=.95, 0,$ and $-.95$ m . The difference between them is less than 10 % .

A few values of $L_{v,x}$ were determined , they are shown in Figure 6.24 . The $L_{v,x}$ values for the smooth surface having a free stream velocity of ~ 6 m/s are larger than those for a free stream velocity of ~ 2 m/s . The latter values appear to be decreasing with height ; more values for the former case would be needed to reach a firm conclusion .

The mean velocity profile for smooth surfaces at free stream velocities of ~ 6 m/s and ~ 2 m/s has already been given in Figures 6.1 , 6.2 , and 6.3 as \bar{U}/\bar{U}_{max} vs. z/δ , the Law of the Wall and the Velocity Defect Law, respectively . The power law exponents for the smooth surface + 1/4 in. square grid - screen is $1/\alpha = .143$ and that for smooth surface + 32 mesh grid

screen is $1/\alpha = .111$ (See equation (3.2)) . The evaluation of this stable simulation is given in Table 6.8 .It is concluded that the smooth surface produces a flow comparable to an A B L stability D-E i.e. neutral / slightly stable . The use of a 1/4 in.square grid placed at $x=8.5$ m , does not help to produce more stable flows . The estimated stability for this flow is neutral/slightly stable (D-E) , too . The 32 mesh grid placed at $x=8.5$ m , produces low turbulence intensities typical of an E-F stability . But the peak of the vertical component energy spectrum was not moved towards higher values of "f" . However, the 32 mesh screen was succesful in decreasing the values of $L_{w,x}$.

One more inconsistency with respect to the stable flow behavior is the fact that the value of u_* can not be decreased further by mechanical means . The above noted inconsistencies are serious and therefore , it will not be claimed that stable flows may be produced by using the 32 mesh screen configuration. The flow produced under this configuration has been evaluated as a D-E (neutral/slightly stable) stability category. However, note that it is very close to the E stability category .

Simulation of the Unstable Atmosphere

The unstable atmosphere is characterized by large turbulence intensities and length scales . The effect of a barrier is to produce large scale turbulence in the vertical and lateral directions , however , since the boundary layer height is also increased ,once the length scales are normalized ,the

values in the lower third of the boundary layer are very similar to the normalized values when no barrier is used . The effect of a 3 in. barrier placed well within the working section in producing a sufficiently large scale in order to reproduce unstable atmospheric flows is studied in this section . The working section was covered with sand roughness and the barrier was placed at $X=3.66$, 6.1 , and 8.5 m . As a first approximation only one point at $z=5$ cm ($z/\delta =.119$) for each of the three positions of the barrier was analyzed .

The turbulence intensities referred to the local mean velocity for this experiments, are tabulated in Table 6.5 . The higher turbulence intensities are produced by moving the barrier towards the test section .

TABLE 6.5
TURBULENCE INTENSITIES AS A FUNCTION OF THE
POSITION OF THE 3 in. BARRIER ON THE WORKING SECTION .

SET	3 in.Barrier at X (m)	u'/\bar{U}	v'/\bar{U}	w'/\bar{U}
723-A and 723-B	3.66	.113 (D)	.102 (D-E)	.064 (D)
	6.10	.134 (D)	.132 (C-D)	.096 (C-D)
	8.53	.252	.184 (C)	.153 (C)

The vertical and lateral energy spectra for these runs are plotted in Figures 6.25 and 6.26 . In both energy spectra the maximum occurs at lower values of "f" than for the neutral A B L energy spectra . These energy spectra are also shifted upwards from the A B L neutral ones . This may be due to an underestimation of u_* . Note that u_* is a characteristic of the type of floor and is calculated assuming an equilibrium boundary layer flow using values of mean velocity close to the floor .

The length scales for these runs are given in Figure 6.30. The vertical length scales obtained by placing the 3 in. Barrier at $X=3.66$ and 6.1 m are very similar . The lateral length scale obtained with the 3 in. Barrier at $X=3.66$ m is larger than that obtained by putting the 3 in. Barrier at $X=6.1$ m . According to Pasquill (56) the vertical length scale increases with decreasing stability . Therefore , this measured length scales could be considered representative of unstable atmospheric flows .

It has already been shown that the flow produced by the 3 in. barrier at $X=3.66$ m over sand roughness is nearly an equilibrium flow ,while in the flow produced by putting the barrier at $X=6.1$ m the turbulence intensities decay by about 15 % through the region between $X=9.7$ and 11.6 m . It is expected that this effect would be even greater for the flow produced by the barrier placed at $X=8.5$ m .

Therefore the most attractive configuration for producing

	SET	Z/δ	3" BARRIER AT X (m)
○	723-A	.119	3.66
□	723-A	.119	6.10
△	723-A	.119	8.53

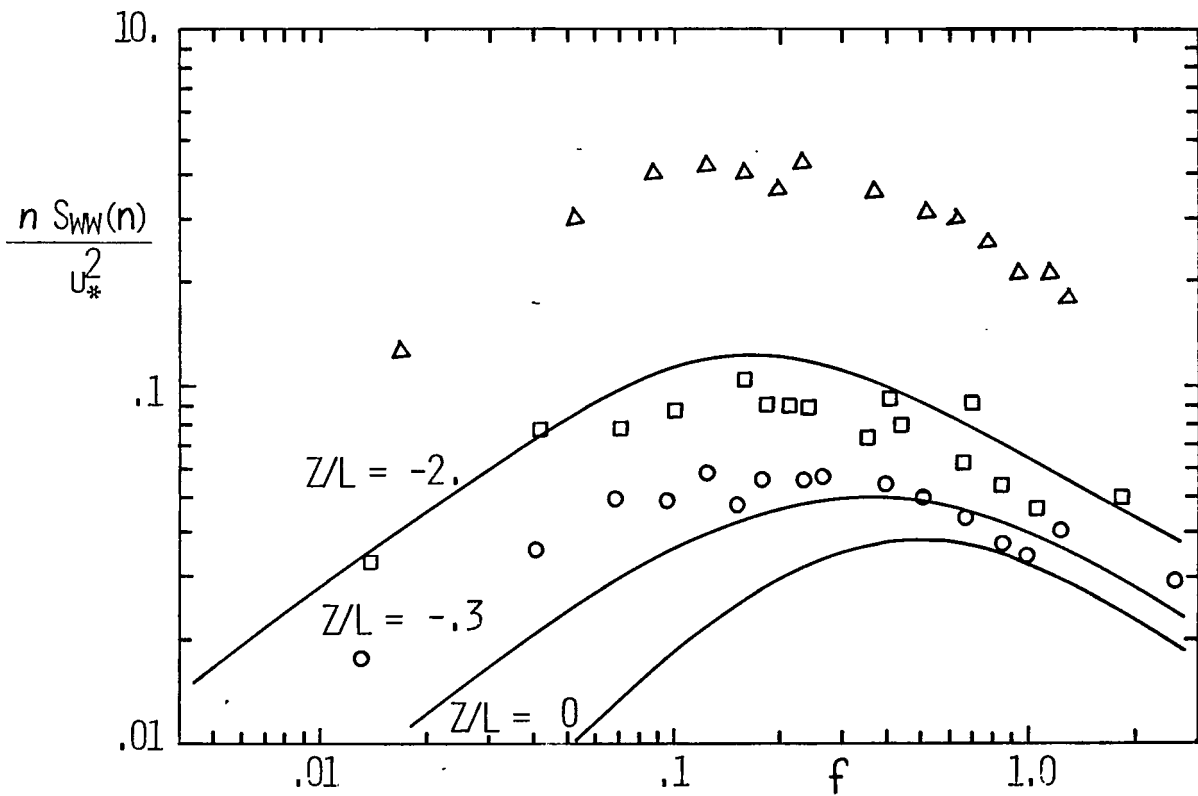


FIGURE 6.25.- EFFECT OF PLACING THE 3" BARRIER AT VARIOUS X (m)
VERTICAL VELOCITY ENERGY SPECTRUM.

	SET	Z/δ	3" BARRIER AT X (M)
○	723-B	.119	3.66
□	723-B	.119	6.10
△	723-B	.119	8.53

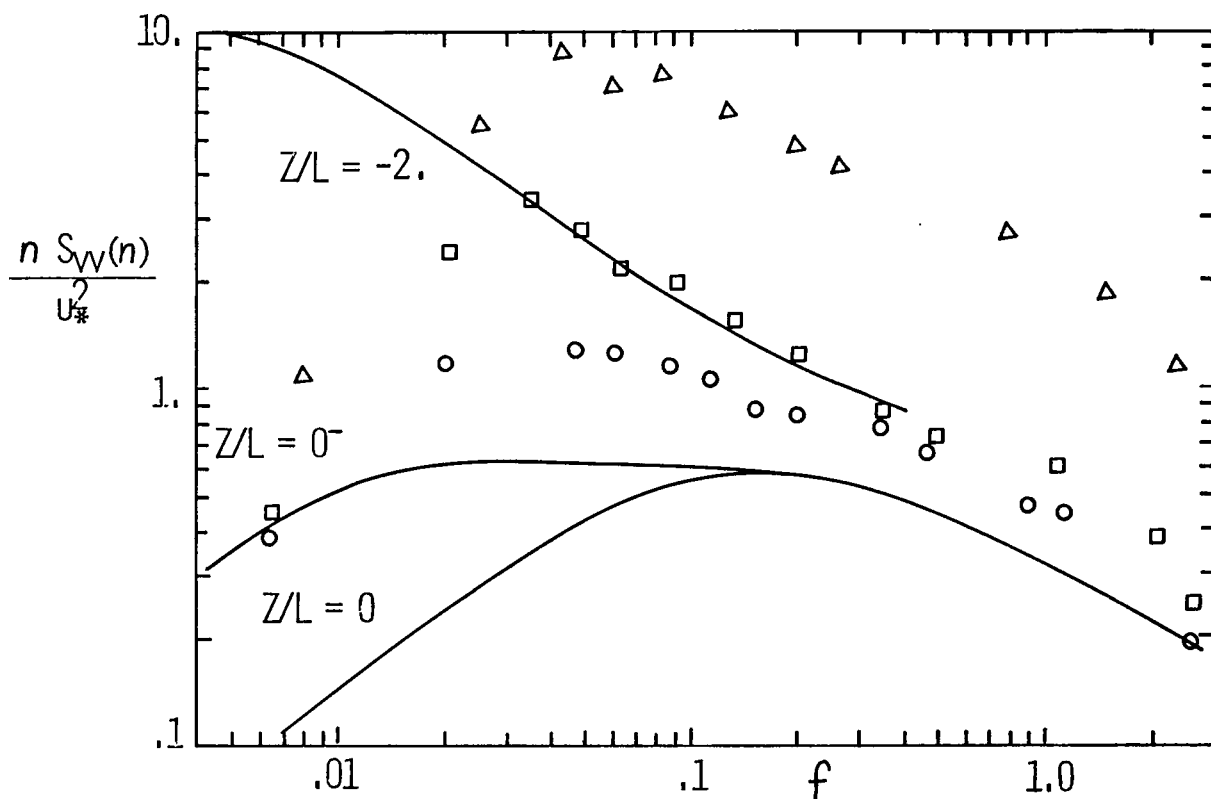


FIGURE 6.26.- EFFECT OF PLACING THE 3" BARRIER AT VARIOUS X (M).
LATERAL VELOCITY ENERGY SPECTRUM.

unstable flows is by putting the 3 in. Barrier at $X=3.66$ m . Very good cross stream homogeneity was obtained by using this configuration as discussed in the previous section .

The turbulence intensities referred to the local mean - velocity for the lower third of the boundary layer for this chosen configuration are plotted in Figure 6.27 and tabulated in Table 6.6 .

TABLE 6.6
TURBULENCE INTENSITIES IN THE LOWER THIRD
OF THE BOUNDARY LAYER.UNSTABLE SIMULATION.

SET	CONFIGURATION	u'/\bar{U}	v'/\bar{U}	w'/\bar{U}
111	S.R.+3"Barrier at	.09-.18	.07-.10	.06-.05
112	X=3.66m. (x=9.7 m)	(D)	(D-E)	(D-E)
203-A	S.R.+3"Barrier at	- - -	.063-.095	.055
205-C	X=3.66m. (x=11.6m)		(D-E)	(D-E)

The vertical turbulence intensity decreases sharply with height up to $z/\delta \sim .05$ and thereafter increases slightly with height . The lateral turbulence intensity decreases with height. Slade (65) proposed that the former increase with height while the latter remain constant for unstable A B L flows .

The longitudinal turbulence intensity is characteristic of neutral stability (D) while the vertical and lateral are characteristic of a D-E stability and do not change appreciably

u'/\bar{U}	w'/\bar{U}	v'/\bar{U}	SET	CONFIGURATION
○	□	△	111/112	3" BARRIER AT X=3.66M
	■	▲	203-A/205-C	3" BARRIER AT X=3.66M

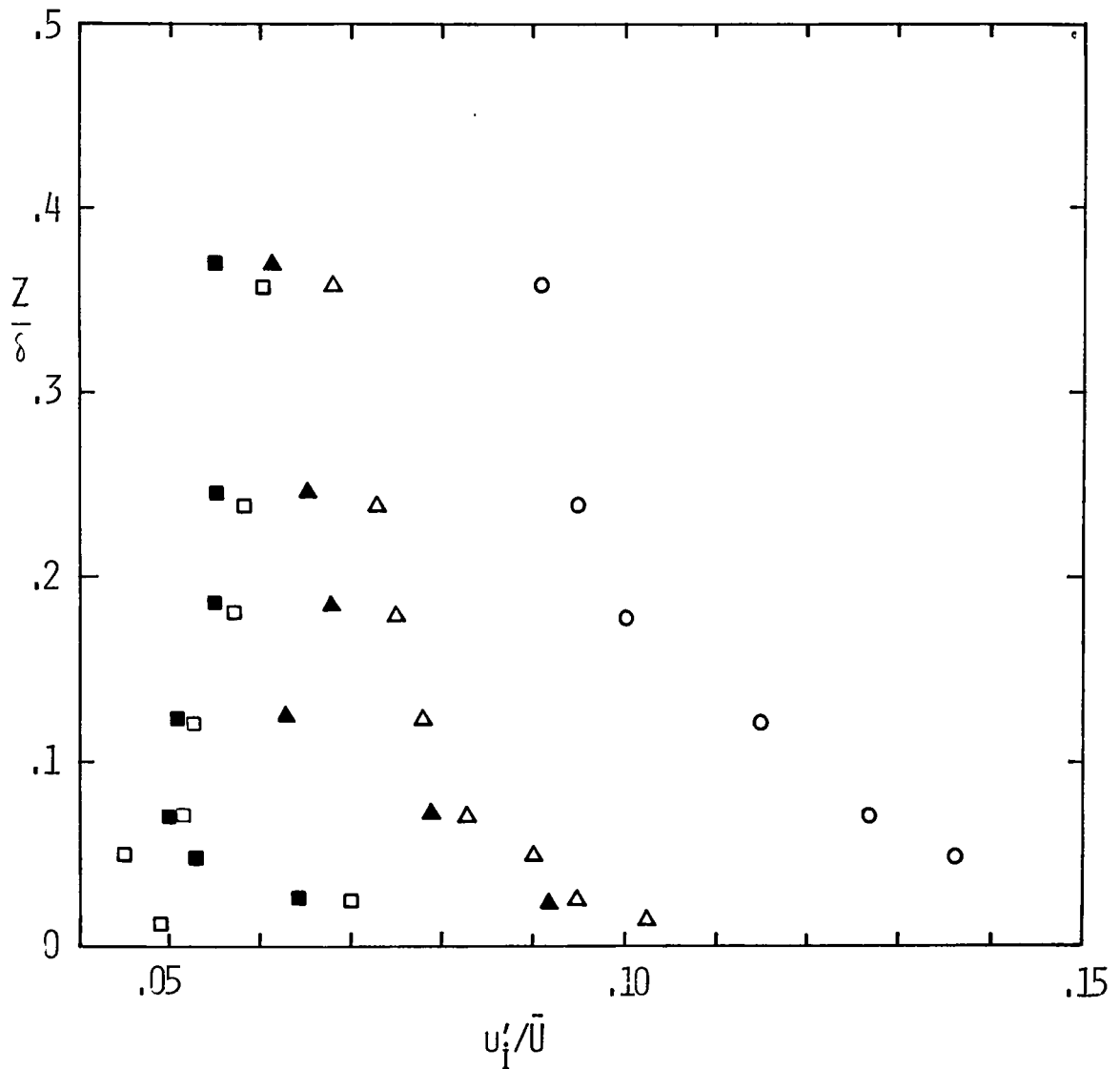


FIGURE 6.27.- UNSTABLE ATMOSPHERE SIMULATION.
TURBULENCE INTENSITIES.

from $x=9.7$ to 11.6 m .

The vertical and lateral energy spectrum obtained from the studied configuration (sand roughness+3 in.Barrier at $X=3.66$ m) are shown in Figure 6.28 and 6.29 .The important feature to be noted is that the peak in both energy spectra is moved towards lower values of "f" and therefore fall in the unstable region of the A B L energy spectra . It will not be intended to evaluate quantitatively the stability from the energy spectrum shape since there is uncertainty about the value of u_* for reasons explained earlier and because there is not an ordered dependence of the lateral spectrum shape on the parameter z/L in the unstable region . The fact that there are some wind tunnel values of the lateral energy spectrum falling in the excluded region will not be discussed here . The cause of this phenomenon in the atmosphere has not been explained.

The vertical and lateral energy spectrum measured at $x=11.6$ m are also shown in these Figures . Note that the shape is a little different from the corresponding energy spectrum measured at $x=9.7$ m , but the peak continues being towards lower frequencies ($f=nz/\bar{U}$) than the neutral energy spectrum peak .

The vertical and lateral length scales for the configuration sand roughness+3 in.Barrier at $X=3.66$ m are shown in Figure 6.30 . In the lower 20 % of the boundary layer , both $L_{w,x}$ and $L_{v,x}$ are larger than those modelling the neutral stability

	SET	x (m)	Z/δ	3" BARRIER AT X (m)
○	111	9.7	.119	3.66
□	203-A	11.6	.123	3.66
●	427	9.7	.119	3.66

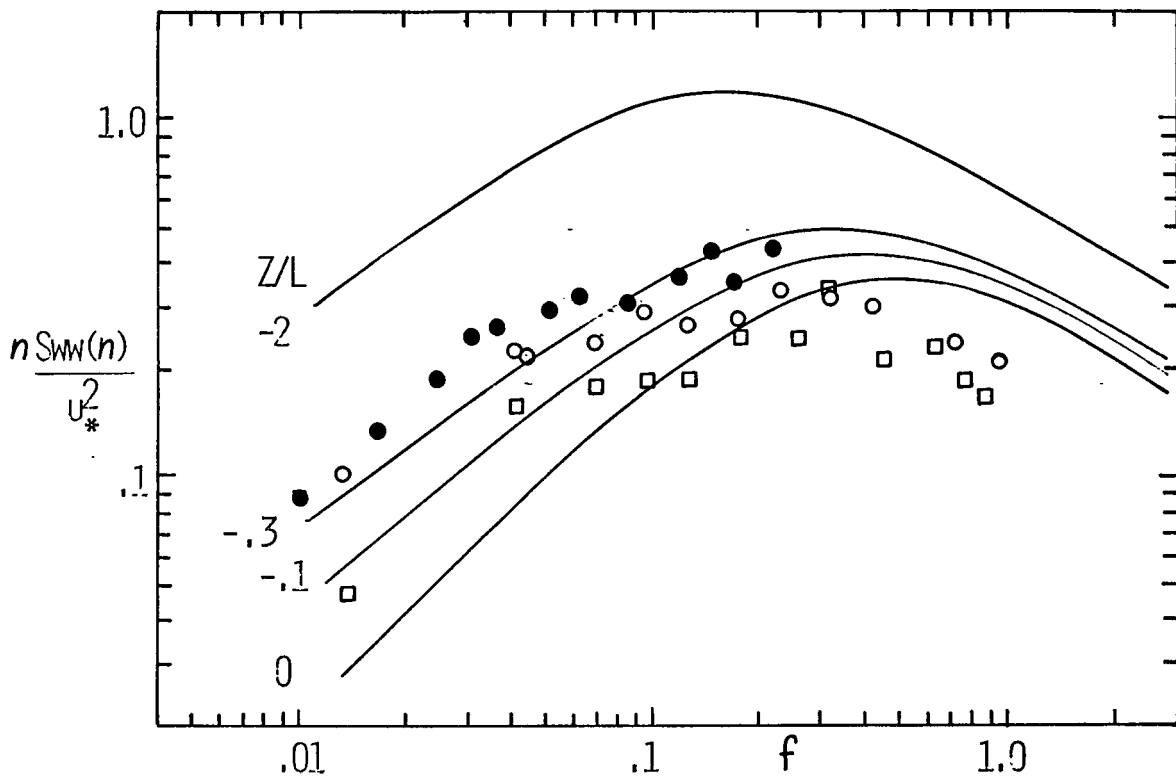


FIGURE 6.28.- UNSTABLE ATMOSPHERE SIMULATION.
VERTICAL VELOCITY ENERGY SPECTRUM.

	SET	x (m)	Z/δ	3" BARRIER AT X (m)
○	112	9.7	.119	3.66
□	205-C	11.6	.123	3.66
●	416	9.7	.119	3.66

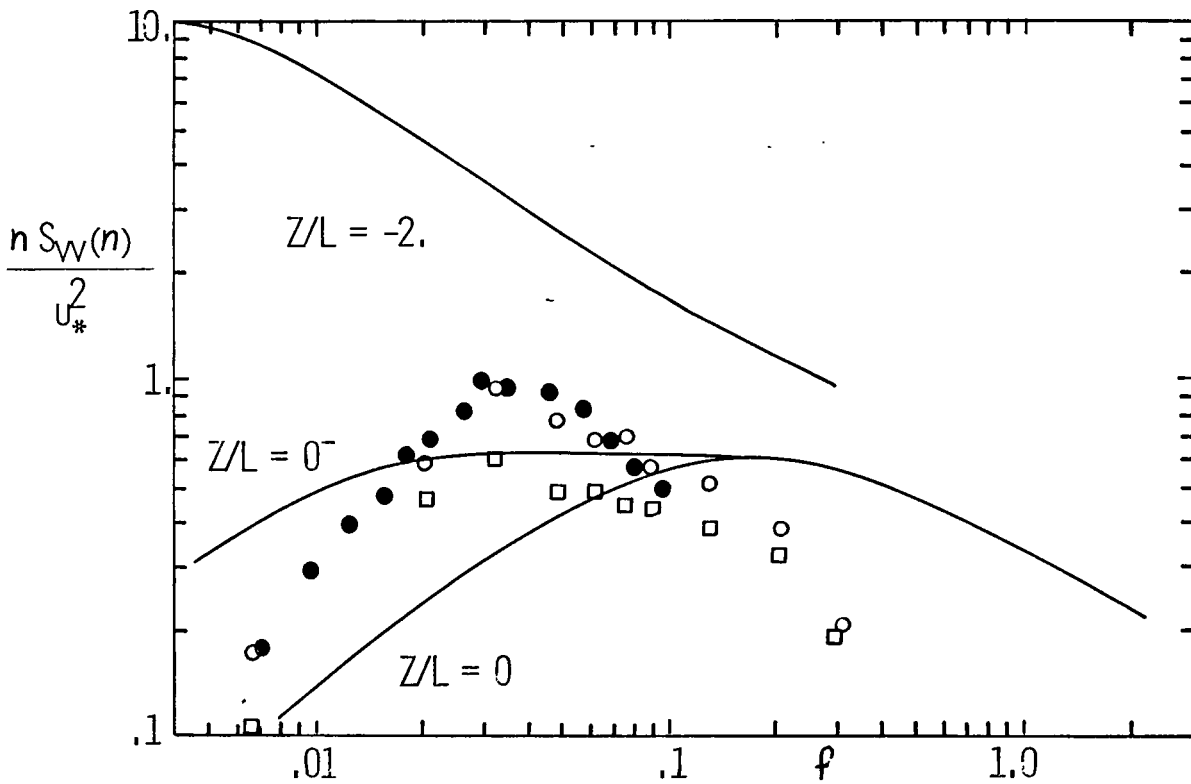


FIGURE 6.29.- UNSTABLE ATMOSPHERE SIMULATION.
LATERAL VELOCITY ENERGY SPECTRUM.

$L_{w,x}$	$L_{v,x}$	SET	x (m)	3" BARRIER AT X (m)
○	□	111/112	9.7	3.66
●	■	203/205-C	11.6	3.66
⊖	⊕	723-A/723-B	10.9	3.66
ϕ	ϕ	723-A/723-B	10.9	6.10

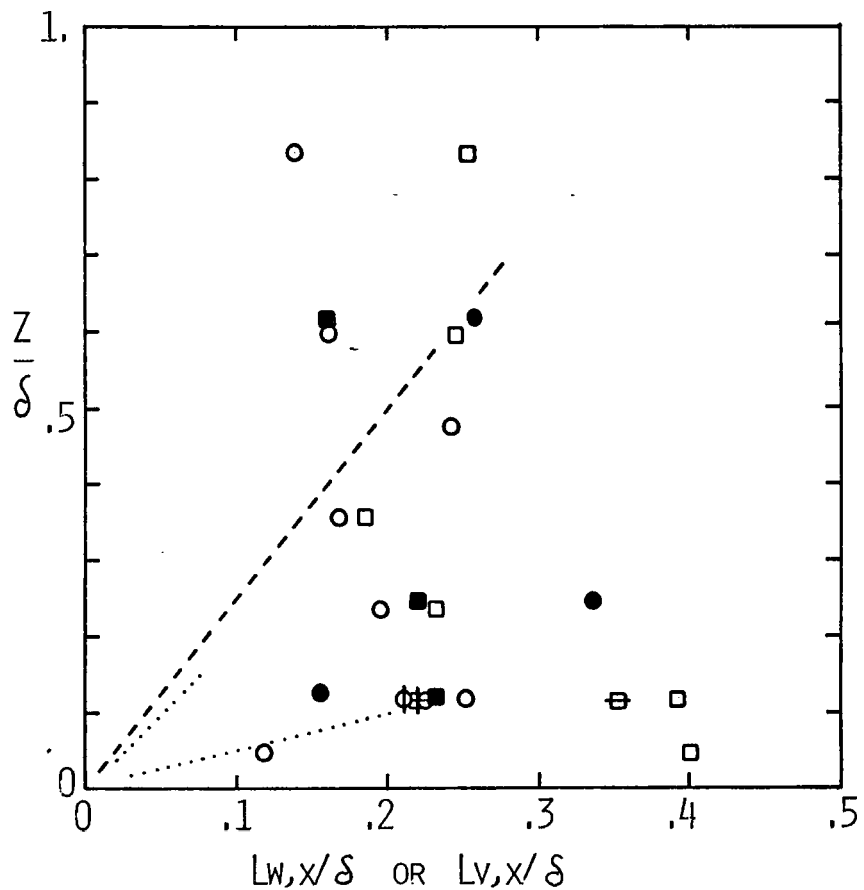


FIGURE 6.30.- UNSTABLE ATMOSPHERE SIMULATION.
VERTICAL AND LATERAL LENGTH SCALES.

and plotted in Figure 6.20 whereas for values of $z/\delta > .2$ the length scales are very similar to values for neutral stability. The values of the vertical length scale for $z/\delta < .2$ are higher than the neutral A B L corresponding values proposed by Teunissen (78) and Pasquill (56) . This is in agreement with Pasquill - (56) who stated that the vertical length scale at a given height should increase with decreasing stability .

Table 6.7 is a comparison between the $L_{w,x}$ and $L_{v,x}$ values for the sand roughness and sand roughness+barrier at 3.66 m configurations .

TABLE 6.7
LENGTH SCALES FOR THE SAND ROUGHNESS AND
SAND ROUGHNESS+3in.BARRIER AT 3.66 m CONFIGURATIONS.

SAND ROUGHNESS		SAND ROUGHNESS+3 in.BARRIER				
x=8.5m $\delta=18$ cm		AT X=3.66 m x=9.7m $\delta=42$ cm				
z (cm)	$L_{w,x}$ (cm)	z (cm)	$L_{v,x}$ (cm)	z (cm)	$L_{w,x}$ (cm)	$L_{v,x}$ (cm)
16.	2.71	10.	3.29	35.	5.88	10.70
8.	2.76	5.	2.65	25.	6.85	10.30
3.	2.40	3.	3.19	20.	10.30	- -
1.	1.35	2.	3.37	15.	7.10	7.81
				10.	8.23	9.83
				5.	10.60	16.60
				2.	5.00	16.80

For a given height , the length scale values are much higher for the sand roughness + 3 in. barrier at $X=3.66$ m . However , the boundary layer height is also increased .

Scaling of the model is done according to the boundary layer height . If a model is scaled to the boundary layer height for the sand roughness configuration and is also subjected to the flow produced by the sand roughness + 3 in. barrier at $X=3.66$ m configuration , the effect will be to simulate very unstable conditions . According to Taylor's equation (2.97) , the dispersion is directly proportional to the magnitude of the length scale . In using this approach, the criterion of reproducing the velocity profile above the model would have to be relaxed . But if the turbulence intensities are typical of unstable flows which would be the most important criterion (in addition to the length scales criterion) , it is believed that a good unstable flow simulation would be reached . This point is further illustrated by the flow visualization results.

Figures 6.31 (a) and (b) show sequences of pictures of the flow visualization tests . For this tests , the stack height was 5 cm and the free stream velocity was ~ 2 m/s . The smoke was produced by the smoke generator described in Chapter V . The reference grid shown in the pictures is formed by 20×10 cm rectangles .

The plume is affected by much larger vertical and lateral length scales using the sand roughness + barrier configuration

Figure 6.31 .- Flow visualization tests.

(Figure 6.31 b) than for the sand roughness configuration . The plume behavior shown in Figures 6.31 a and 6.31 b is typical of neutral and unstable conditions respectively . However , no quantitative evaluation of stability can be done on these grounds or from the length scales reported in Table 6.7. In using this approach, that is to keep constant the scale of the model for all the configurations used regardless of the boundary layer height , the evaluation of flow stability should be done through diffusion experiments in the wind tunnel and the atmosphere .

The velocity profile for the sand roughness + 3 in. Barrier at X=3.66 m configuration has been plotted in Figure 6.7 b . Evaluation of this configuration for the simulation of unstable atmospheric flows is shown in Table 6.8 . It is concluded that the sand roughness + 3 in. Barrier at X=3.66 m produces a flow which is characteristic of a C-D Pasquill stability category, i.e. neutral/slightly unstable .

TABLE 6.8

EVALUATION OF A B L SIMULATION

CONFIGURATION	(cm)	TURBULENCE INTENSITIES			ENERGY SPECTRUM		LENGTH SCALES $L_{w,x}$	EVALUATION
		u'/\bar{U}	w'/\bar{U}	v'/\bar{U}	VERTICAL	LATERAL		
Sand Roughness	18	D	D	D-E	D	D	D	D
Smooth (\bar{U} 6m/s)	17.5	D-E	E	E-F	D	D	D-E	D-E
Mesh Roughness	33	D (Urban)	D (Urban)	- -	D	D	D	D (Urban)
Smooth (\bar{U} 2m/s)	18	D-E	E	E-F	D	D	D-E	D-E
Smooth+1/4"grid	17.5	D-E	E-F	- -	D	- -	D-E	D-E
Smooth+32 mesh grid.	17.5	E	F	- -	D	- -	D-E	D-E
S.R.+3"Barrier at 3.66 m .	42	D	D-E	D-E	Slightly Unstable	Unstable	Slightly Unstable	C-D
S.R.+1.5"Barrier	30	D-E	E	E	D	D	D	D-E

CHAPTER VII

SUMMARY OF RESULTS AND RECOMMENDATIONS

The objective of the present work was the simulation of atmospheric flows under several stabilities by using devices whose interaction with the wind tunnel boundary layer flow would result in the desired flow features . A simulation criteria based on the matching of statistical quantities ,i.e. mean velocity , turbulence intensities , energy spectrum and length scales , was developed and applied to the wind tunnel data for evaluation from a simulation viewpoint . No other simulation in the literature has been analyzed so thoroughly . The results from the present simulation are highly reliable.

The analysis of the effect of the turbulence producing devices , e.g. different roughnesses , barriers , etc., was made in the first section of Chapter VI . It was concluded from this analysis that the smooth surface flows could be used for simulating a stable atmosphere ; that the sand roughness and mesh roughness could be used to simulate the neutral rural and urban atmosphere respectively and that the 3 in. barrier over sand roughness placed at $X=3.66$ m was capable of producing a large scale flow typical of an unstable rural A B L .

The summary of the results of the simulation are given below .

Neutral Atmosphere Simulation

The neutral simulation was very successful . Rural and neutral flows whose characteristics agree entirely with the corresponding atmospheric characteristics were achieved using the sand and mesh roughness configurations . It is believed that if in the sand roughness + 1.5 in. barrier configuration , the sand roughness covered the entire working and test sections - instead of the working section alone , a D stability flow would be obtained .

Stable Atmosphere Simulation

A stable simulation consistent with all the characteristics of the stable atmosphere was not produced . The smooth floor produced a flow which was evaluated as typical of a D-E Pasquill stability category : neutral/slightly stable flow . A mesh screen placed at $x=8.5$ m was successful in reducing the flow length scale . However , the flow produced in this way can not be considered typical of a stable atmosphere .

Unstable Atmosphere Simulation

The configuration using a 3 in. barrier placed at $X=3.66$ m over sand roughness was partially successful in simulating unstable atmospheric flows . The flow produced may be regarded as that of a C-D Pasquill stability category ; neutral/slightly unstable . However , it is believed that the simulation of more unstable flows is possible by using this configuration and keeping the scale of the model consistent with the boundary layer

height produced by the sand roughness flow (neutral simulation) .

Recommendations for Future Work

Wind tunnel diffusion studies on a flat plate should be undertaken in order to verify the proposed simulation configurations and to try to extend the range of stability categories to include the simulation of a more unstable atmosphere .Stability evaluation would be done by comparison against atmospheric diffusion studies .

The 3 in. barrier placed within the working section over the mesh roughness should produce a very unstable flow . Such configuration should be tried in the future .

The simulation of a stable atmosphere will have to be done by imposing a temperature profile on the wind tunnel flow. The capability of producing a temperature profile on the wind tunnel flow will have to be introduced in the future as the modelling techniques improve and become more sophisticated.

BIBLIOGRAPHY

1. Antonia, R.A. and R.E. Luxton, "The Response of a Turbulent Boundary Layer to a Step Change in Surface Roughness. Part 2. Rough to Smooth", *J. of Fluid Mechanics*, 53, p.737, (1972).
2. Armitt, A.J. and J. Counihan, "The Simulation of the Atmospheric Boundary Layer in a Wind Tunnel", *Atmospheric Environment*, 2, p.49, (1968).
3. Arya, S.P.S. and E.J. Plate, "Modelling of the Stable Stratified Atmospheric Boundary Layer", *J. of the Atmospheric Sciences*, 26 No.4, p.656, (1969).
4. Batchelor, G.K., "The Conditions for Dynamic Similarity of Motions of a Frictionless Perfect Gas Atmosphere", *Quart. J. of the Royal Met. Soc.*, 79, p.224, (1953).
5. Busch, N.E. and H.A. Panofsky, "Recent Spectra of Atmospheric Turbulence", *Quart. J. of the Royal Met. Soc.*, 94, p.132, (1968).
6. Busch, N.E., J.A. Frizzola and I.A. Singer, "The Micrometeorology of the Turbulent Flow Field in the Atmospheric Surface Boundary Layer", *Acta Polytechnica Scandinavica, Phys. Inc., Nucleonics Ser.*, 59, (1968).
7. Cermak, J.E., "Lagrangian Similarity Hypothesis Applied to Diffusion in Turbulent Shear Flow", *J. of Fluid Mechanics*, 15, p.49, (1963).
8. Cermak, J.E., "Laboratory Simulation of the Atmospheric - Boundary Layer", Presented at the Session on Fluid Physics of Pollution, AIAA 3rd. Fluid and Plasma Dynamics Conference, (1970).
9. Cermak, J.E., "Laboratory Simulation of the Atmospheric Boundary Layer", *AIIA Journal*, 9, No.9, p.1746, (1971).
10. Cermak, J.E., D.J. Lombardy and R.S. Thompson, "Applications of Physical Modelling to the Investigations of Air Pollution Problems in Urban Areas", Paper presented at the 67 th Annual Meeting of the APCA, (1974).
11. Chaudry, F.H., and R.N. Meroney, "A Laboratory Study of Diffusion in Stably Stratified Flow", *Atmospheric Environment*, 7, p.443, (1973).
12. Clauser, F.H., "The Turbulent Boundary Layer", *Advances in Applied Mechanics*, IV, A.P., (1956).

13. Cook, N.J., "On Simulating the Lower Third of the Urban Adiabatic Boundary Layer in a Wind Tunnel", *Atmospheric Environment*, 7, p.691, (1973).
14. Counihan, J., "An Improved Method of Simulating an Atmospheric Boundary Layer in a Wind Tunnel", *Atmospheric Environment*, 3, p.197 (1969).
15. Counihan, J., "Further Measurements in a Simulated Atmospheric Boundary Layer", *Atmospheric Environment*, 4, p.259 (1970).
16. Counihan, J., "Simulation of an Adiabatic Urban Boundary Layer in a Wind Tunnel", *Atmospheric Environment*, 7, p.673 (1973).
17. Counihan, J., "Adiabatic Atmospheric Boundary Layers: A Review and Analysis of the Data from the Period 1880-1972", *Atmospheric Environment*, 9, p.871 (1975).
18. Davenport, A.G., "The Spectrum of Horizontal Gustiness Near the Ground in High Winds", *Quart. J. of the Royal Met. Soc.*, 87, p.194 (1961).
19. Davenport, A.G., "The Relationship of Wind Structure to Wind Loading", Paper 2, Symposium 16, Proc. of Conf. on "Wind Effects on Buildings and Structures" at NPL, June 1963 HMSO, London (1965).
20. Doebelin, E.O. "Measurement Systems: Applications and Design", Mc Graw Hill (1966).
21. Golden, J. "Scale Model Techniques", M.S. Thesis, College of Engineering, New York University (1961).
22. Hama, F.R. *Soc. Naval Architects Marine Engrs. Trans.*, 62, p.333 (1954).
23. Harris, R.I. "Measurements of Wind Structure at Heights up to 598 ft. Above Ground Level", *Symp. on Wind Effects on Buildings and Structures*, Loughborough Univ. of Tech. (1968).
24. Haugen, D.A., J.C. Kaimal and E.F. Bradley, "An Experimental Study of Reynolds Stress and Heat Flux in the Atmospheric Surface Layer", *Quart. J. of the Royal Met. Soc.*, 97, p.168 (1971).
25. Hay, J.S. and F. Pasquill, "Diffusion from a Continuous Source in Relation to the Spectrum and Scale of Turbulence", *Atmospheric Diffusion and Air Pollution*, ed. F.N. Frenkiel and P.A. Sheppard, *Advances in Geophysics*, 6, p.345 (1959).

26. Hinze, J.O., "Turbulence", 2nd. Ed., Mc Graw Hill (1975).
27. Hoydysh, W.G., Y. Ogawa, and R.A. Griffiths, "A Scale Model Study of the Dispersion of Pollution in Street Canyons", Paper presented at the 67th. Annual Meeting of the APCA (1974).
28. Hunt, J.C.R., and H. Fernholz, "Simulation of the Atmospheric Boundary Layer; a Report on Euromech 50, J. of Fluid Mechanics, p.543 (1975).
29. Izyumov, N., T. Jandali and A.G. Davenport, "Model Studies and the Prediction of Full Scale Levels of Stack Gas Concentration", J. of the Air Pollution Control Association, 26, No.10, p.956 (1976).
30. Izumi, Y., "Kansas 1968 Field Program Data Report", AFCRL-72-0041, Environmental Research Papers, No.379 (1971).
31. Jackson, N.A., "The Propagation of Modified Flow Downstream of a Change in Roughness", Quart. J. of the Royal Met. Soc., 102, p.924 (1976).
32. Jensen, M., "The Model-Law for Phenomena in a Natural Wind", Ingenioren Int. Ed., 2, No.4 (1958).
33. Kaimal, J.C., "Turbulence Spectra, Length Scales and Structure Parameters in the Stable Surface Layer", Boundary Layer Meteorology, 4, p.289 (1973).
34. Kaimal, J.C., and D.A. Haugen, "Characteristics of Vertical Velocity Fluctuations on a 430 m Tower", Quart. J. of the Royal Met. Soc., 93, p.305 (1967).
35. Kaimal, J.C., J.C. Wyngaard, and O.R. Cote, "Spectral Characteristics of Surface Layer Turbulence", Quart. J. of the Royal Met. Soc., 98, p.563 (1972).
36. Kampe de Fariet, M.J., "Les Fonctions Aleatoires Stationnaires et la Theorie Statistique de la Turbulence Homogene", Ann. Soc. Sci. Brux., 59, p.145 (1939).
37. Klebanoff P.S. and Z.W. Diehl, "Some Features of Artificially Thickened Fully Developed Turbulent Boundary Layers with Zero Pressure Gradient", NACA TN 2475 (1951).
38. Lee, N., "Studies on Turbulent Diffusion", Ph.D. Thesis, - Department of Chemical Engineering, University of Houston (1976).

39. Lee, N., and A.E. Dukler, "Lagrangian Simulation of Dispersion in Turbulent Shear Flow with a Hybrid Computer", AICHE Journal, 22 No. 3, p. 449 (1976).
40. Lumley, J.L., and H.A. Panofsky, "The Structure of Atmospheric Turbulence", Interscience Pub. John Wiley and Sons (1964).
41. Luna, R.E., and H.W. Church, "A comparison of Turbulence Intensity and Stability Ratio Measurements to Pasquill Stability Classes", J. of Applied Meteorology, 11, p. 663 (1972).
42. Mc Vehil, G.E., G.R. Ludwig and T.R. Sundaram, "On the Feasibility of Modelling Small Scale Atmospheric Motions", Cornell Aeronautical Lab. Report No. ZB-2328-p-1 (1967).
43. Meroney, R.N., J.E. Cermak and B.T. Yang, "Modelling of Atmospheric Transport and Fumigation at Shoreline Sites", Boundary Layer Meteorology, 9, p. 69 (1975).
44. Mery, P., J.P. Schon and J. Solal, "Comparison of Thermally Neutral and Unstable Shear Flows in the Wind Tunnel and the Atmosphere", Int. Symp. on Turbulent Diffusion in Environmental Pollution, Advances in Geophysics, Ed. by F.N. Frenkiel and R.E. Munn, 18 B, p. 273 (1974).
45. Mickelsen, W.R., "An Experimental Comparison of the Lagrangian and Eulerian Correlation Coefficients in Homogeneous Isotropic Turbulence", NACA Washington, Tech. Note No. 3570 (1955).
46. Monin, A.S., "Smoke Propagation in the Surface Layer of the Atmosphere", Atmospheric Diffusion and Air Pollution, Ed. by F.N. Frenkiel and P.A. Sheppard, Advances in Geophysics, 6, p. 331 (1959).
47. Monin, A.S., and A.M. Yaglom, "Statistical Fluid Mechanics, MIT Press (1971).
48. Nagib, H.M. and J. Tan-atichat, "Wind Tunnel Simulation of the Neutral Atmospheric Surface Layers by the Counter Jet Technique", J. of the Air Pollution Control Association, 26, p. 668 (1976).
49. Nee, V.W., A.A. Szeuczyk, K. Yang, F.B. Cheung and V.K. Liu, "The Simulation of the Atmospheric Surface Layer in the Notre Dame Atmospheric Wind Tunnel", Paper Presented at the - 67th. Annual Meeting of the APCA (1974).

50. Ogawa, Y., "A New Wind Tunnel for the Simulation of Atmospheric Diffusion", Paper presented at the 69th. Annual Meeting of the APCA (1976).
51. Ogawa, Y., R. Griffiths and W. Hoydysh, "A Wind Tunnel Study of Sea Breeze Effects", *Boundary Layer Meteorology*, 8, p.141 (1975).
52. Panofsky, H.A. and B. Prasad, "Similarity Theories and Diffusion", *Int. J. of Water Pollution*, 9, p.419 (1965).
53. Pasquill, F., "The Influence of the Turning of Wind with Height on Cross-wind Diffusion", *Phil. Transactions of the Royal Soc. of London, Ser. A*, 265, p.173 (1969).
54. Pasquill, F., "Wind Structure of the Atmospheric Boundary Layer", *Discuss. on Archit. Aero. Phil. Trans. R. Soc.*, A269, p.321 (1970).
55. Pasquill, F., "Some Aspects on Boundary Layer Description- Presidential Address", *Quart. J. of the Royal Meteorological Society*, 98, p.469 (1972).
56. Pasquill, F., "Atmospheric Diffusion", 2nd. Edition, Halsted Press, (1974).
57. Pasquill, F. and F.B. Smith, "The Physical and Meteorological Basis for the Estimation of Dispersion", *Proc. of the 2nd. Int. Clean Air Congress*, Ed. by H.M. Englund and W.T. Beery, A.P. (1971).
58. Plate, E.J., "Aerodynamic Characteristics of Atmospheric Boundary Layers", U.S. Atomic Energy Commission (1971).
59. Plate, E.J. and C.W. Lin, "Investigations of the Thermally Stratified Boundary Layer", Paper No. 5, *Fluid Mechanics Papers*, Colorado State University (1966).
60. Schon, J.P. and P. Mery, "A Preliminary Study of the Simulation of the Neutral Atmospheric Boundary Layer using Air Injection in a Wind Tunnel", *Atmospheric Environment*, 5, p.299 (1971).
61. Schon, J.P., J. Mathieu, A. Baille, J. Solal and G. Comte-Bellot, "Experimental Study of Diffusion Processes in Unstable Stratified Boundary Layers", *Int. Symposium on Turbulent Diffusion in Environmental Pollution*, Ed. by F.N. Frenkiel and R.E. Munn, *Advances in Geophysics*, 18-B, p.265 (1974).
62. Seinfeld, J.H., "Air Pollution, Physical and Chemical Fundamentals", Mc Graw Hill (1975).

63. Sethuraman, S. and J.E.Cermak, "Mean Temperature and Mean Concentration Distributions over a Physically Modelled Three Dimensional Heat Island for Different Stability Conditions", *Boundary Layer Meteorology*, 9, p.427 (1975).
64. Sharan, V.Kr. and S.Wickerts, "A note on the Spectra of Wind Velocity Components in the Surface Layer", *Quart.J.of the Royal Meteorological Society*, 100, p.365 (1974).
65. Slade, D.H., "Meteorology and Atomic Energy", U.S. Atomic Energy Commission, (1968).
66. Smith, E.G., "The Feasibility of Using Models for Predetermining Natural Ventilation", *Res.Rep.Tex.Eng.Exp.Stn.* 26, (1951).
67. Smith, F.B., "An Analysis of Vertical Wind Fluctuations at Heights between 500 and 1500 feet", *Quart.J.of the Royal Meteorological Society*, 87, p.180 (1961).
68. Smith, F.B. and P.F.Abbott, "Statistics of Lateral Gustiness at 16 metres above ground", *Quart.J.of the Royal Meteorological Society*, 87, p.549 (1961).
69. Smith, M.E. and I.A.Singer, "Proc.Nat.Air Pollution Symposium, 3rd, Pasadena, Calif. (1955).
70. Snyder, W.H., "Similarity Criteria for the Application of Fluid Models to the Study of Air Pollution Meteorology", *Boundary Layer Meteorology*, 3, p.113 (1972).
71. Snyder, W.H. and R.E.Lawson, "Determination of a Necessary Height for a Stack Close to a Building-A Wind Tunnel Study", *Atmospheric Environment*, 10, p.683 (1976).
72. Spiegel, E.A. and G.Veronis, "On the Bousinesq Approximation for a Compressible Fluid", *Astrophysical Journal*, 131, p.442 (1960).
73. Sutton, O.G., "Atmospheric Turbulence", Methuen (1949).
74. Sutton, O.G., "Micrometeorology", Mc Graw-Hill (1953).
75. Taylor, G.I., "Diffusion by Continuous Movements", *Proc. London Mathematical Society*, Ser.2, 20, p.196 (1921).
76. Taylor, R.J., J.Warner and N.E.Bacon, "Scale Length in Atmospheric Turbulence as Measured from an Aircraft", *Quart. J.of the Royal Meteorological Society*, 96, p.750 (1970).

77. Tennekes, H. and Lumley, J.L., "A First Course in Turbulence", MIT Press (1972).
78. Teunissen, H.W., "Characteristics of the Mean Wind and Turbulence in the Planetary Boundary Layer", UTIAS Review No.32 (1970).
79. Teunissen, H.W., "Simulation of the Planetary Boundary Layer in a Multiple Jet Wind Tunnel", UTIAS Report No.182 (1972).
80. Teunissen, H.W., "Simulation of the Planetary Boundary Layer in a Multiple Jet Wind Tunnel", Atmospheric Environment, 9, p.145 (1975).
81. Townsend, A.A., "The Structure of Turbulent Shear Flow", Cambridge University Press (1956).
82. Weber, A.H., J.S. Irwin, J.P. Kahler and W.B. Petersen, "Atmospheric Turbulence Properties in the Lowest 300 Meters", North Carolina State University, EPA-600/4-75-004, Environmental Monitoring Series (1975).
83. Wilson, J.W. Jr., "The Development of a Low Speed Wind Tunnel for Use in the Physical Modelling of the Atmosphere", University of Houston, Department of Chemical Engineering, M.S. Thesis (1975).

APPENDIX A

PRESSURE TRANSDUCER CALIBRATION

The pressure transducer calibration was done in the wind tunnel . The Pitot tube described in Chapter V was used , The calibration was done against a Meriam micromanometer whose - readability was $\pm .001$ iwg . The fluid used a Meriam manometric fluid of density = 1.000 g/cm^3 .

✱ It was found that the pressure transducer output was effectively linear with pressure . The slope of the straight line was $.03433 \text{ in.water/volt}$. The span knob of the Validyne CD-15 carrier demodulator was set at 10.0 , i.e. the gain of the output was set at the maximum .

Tabulation for Calibration :

Δh (iwg)	.053	.025	.0
E (Volts)	1.625	.705	.0

Pitot tube equation .-

The Pitot tube formula based on Bernoulli's Theorem was used .

$$\bar{u} = \sqrt{\frac{2 \Delta P_{man} g_c}{\rho_{air}}} = \sqrt{\frac{2 \Delta h_{man} \rho_{man. fluid} g_c}{\rho_{air}}}$$

For Δh_{man} in inches of water and with the interpolation formula for the density of air as a function of temperature :

$$\rho = .0857 - 1.47 \times 10^{-4} T (^{\circ}F) \quad [=] \quad \text{lb}_m / \text{ft}^3$$

it is obtained

$$\bar{u} = 5.5736 \sqrt{\frac{\Delta h_{man} (\text{iwg})}{.0857 - 1.47 \times 10^{-4} T (^{\circ}F)}} \quad [=] \quad \text{m/s} \quad (\text{A-1})$$

A correction due to viscosity effects at low wind velocities was done according to Doebelin (20) .

$$\Delta P = c \rho \bar{u}^2 / 2$$

$$c = 1 + (4/Re) \quad ; \quad Re = \bar{u} r / \nu$$

Where r is the radius of the Pitot tube (.054 cm) . Equation (A-1) becomes

$$\bar{u} = 5.5736 \sqrt{\frac{1}{C} \sqrt{\frac{\Delta h_{man} (\text{in } \omega g)}{.0857 - 1.47 \times 10^{-4} T (^{\circ}F)}}} \quad [] \quad \text{m/s} \quad (\text{A-2})$$

APPENDIX B

HOT-WIRE ANEMOMETER CALIBRATION

Single Hot-film calibration.-

Usually calibration was done for each set of measurements against the velocity obtained with a Pitot tube and pressure transducer readings through the "Averaging box" . One calibration was done by digitizing the output from the anemometer and from the pressure transducer and taking the average from the digitized values . The results are plotted in Figure B-1 . Calibrations done against Pitot tube/pressure transducer outputs from the "Averaging box" were linear ($\bar{U}_{\text{hot-film}}$ vs. $\bar{U}_{\text{pres.transd.}}$) , showing average percent deviations consistently lower than 1 % .

X hot-film calibration.-

The X hot film-calibrations were always done against the output from the "Averaging box" and are not as accurate as for the single hot-film . Nevertheless , average percent deviations of 2 % or less are typical of these X hot-film calibrations . Usually four points were used , the lowest and higher velocities expected for a particular set of runs and two intermediate velocities . These calibration points were taken for different wind speeds outside the boundary layer .

The effect of using an erroneous value of radius in the correction for viscosity effects (see Appendix A) is also shown in Figure B-1 . Observe that the \bar{U} Pitot tube values are

shifted downwards by a constant (.28 m/s) in the range of velocities 2-6 m/s . The reported runs that were subject to this error were corrected accordingly .

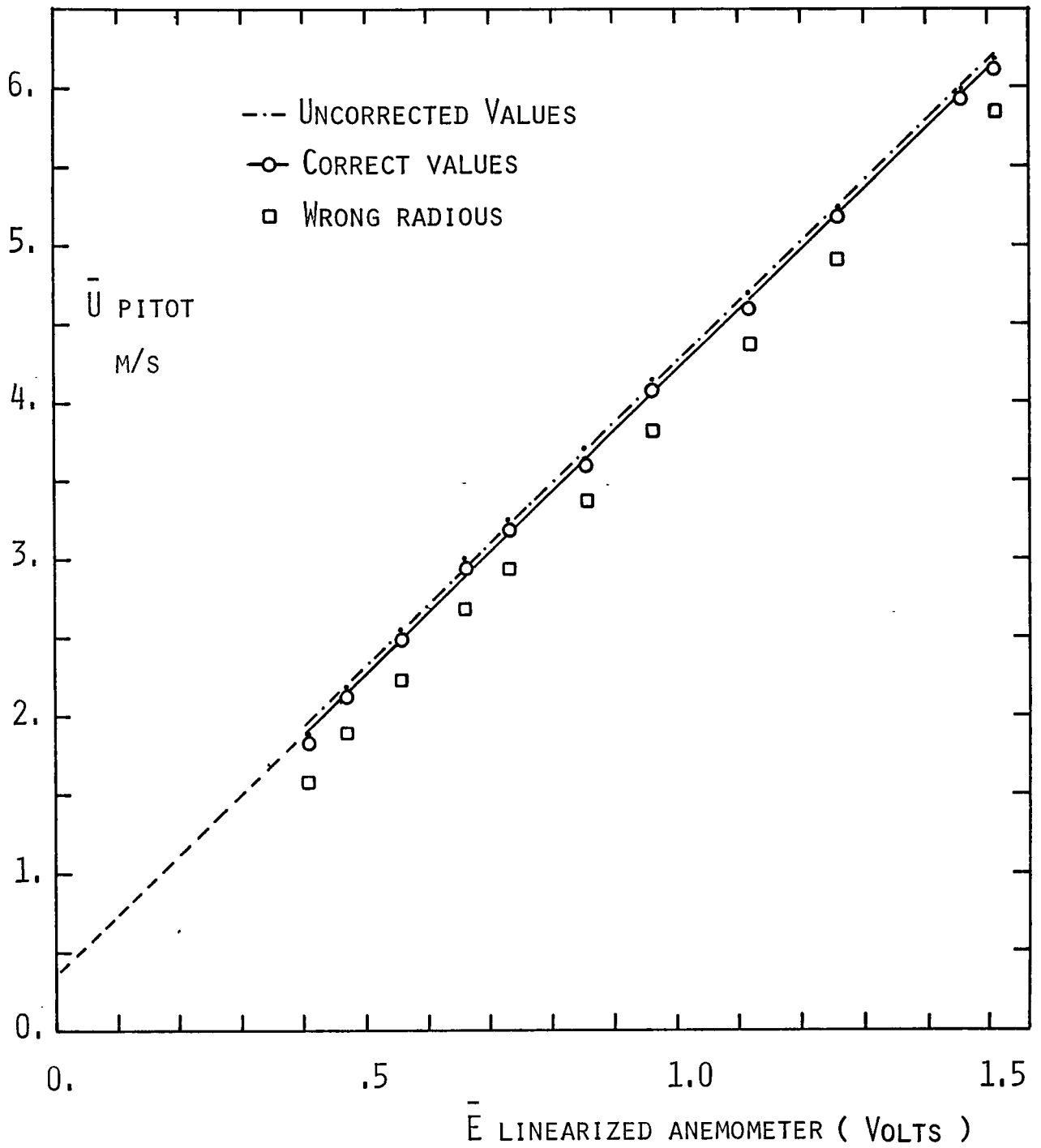


FIGURE B-1 .- SINGLE HOT FILM CALIBRATION .

APPENDIX C

EVALUATION OF DIGITIZATION PROGRAM

Comparison between digitization program values and correlator/
RMS voltmeter values .-

Set 111

Run No.	u'/\bar{U}_{\max} (P)	u'/\bar{U}_{\max} (C)	Percent Deviation	w'/\bar{U}_{\max} (P)	w'/\bar{U}_{\max} (C)	Percent Deviation
1	.0386	.0438	- 13.3	- -	- -	- -
2	.0653	.0653	0.	.0489	.0502	- 2.53
3	.0725	.0754	- 4.08	.0534	.0561	- 5.0
4	.0791	.0791	0.	.0524	.0569	- 8.55
5	.0816	.0791	3.04	.0534	.0581	- 8.75
6	.0826	.0822	.46	.0503	.0539	- 7.21
7	.0841	.0843	- .23	.0480	.0518	- 7.95
8	.0922	.0864	6.31	.0428	.0485	-13.36
9	.0973	.0928	- 4.61	.0380	.0442	-16.6
11	.1020	.1060	- 3.74	- -	- -	- -

Note: Percent deviation = (Program value-correlator value)x100.
÷ program value .

C-2.Comparison of \bar{U}, u', w' and \overline{uw} taken at different sampling frequencies .-

Set 709

Run No.	$\bar{U}_{500}/\bar{U}_{50}$	u'_{500}/u'_{50}	w'_{500}/w'_{50}	$\overline{uw}_{500}/\overline{uw}_{50}$
3	1.005	1.011	1.092	.976
5	.989	.996	1.122	.814
8	1.007	1.085	1.111	.937
9	.982	1.097	1.064	1.235
10	1.018	1.095	1.058	1.278
11	1.001	1.112	.918	.973

Note:The time period of sampling is the necessary for collection of 8192 data points in the digitization program .

C-3 . Estimation of the error for mean velocity values measured with single hot-wire anemometer , using Pitot tube values as a reference .

Set 107

\bar{U}_s	$\bar{U}_{Pit.}$	$\frac{\bar{U}_s - \bar{U}_{Pit.}}{\bar{U}_{Pit.}}$
m/s	m/s	%
6.24	6.24	0.
6.18	6.19	- .162
6.10	6.12	- .327
5.95	5.98	- .502
5.73	5.80	-1.210
5.50	5.54	- .722
5.16	5.23	-1.34
4.85	4.92	-1.42
4.52	4.58	-1.31
4.26	4.32	-1.39
3.81	3.82	- .262
3.38	3.37	.297

Average % Dev.=.75

Set 108

\bar{U}_s	$\bar{U}_{Pit.}$	$\frac{\bar{U}_s - \bar{U}_{Pit.}}{\bar{U}_{Pit.}}$
m/s	m/s	%
6.19	6.21	- .322
6.15	6.16	- .162
6.03	6.05	- .331
5.79	5.83	- .686
5.54	5.61	-1.25
5.22	5.31	-1.70
4.87	4.93	-1.22
4.50	4.58	-1.75
3.75	3.85	-2.60
3.33	3.34	- .30

Average % Dev.=1.03

Estimation of the error on mean velocity values measured with an X hot-wire anemometer , using Pitot tube values as a reference.-

Set 1012-A

\bar{U}_s	$\bar{U}_{Pit.}$	$\frac{\bar{U}_s - \bar{U}_{Pit.}}{\bar{U}_{Pit.}}$
m/s	m/s	%
6.02	6.04	- .331
6.02	5.90	2.034
5.94	5.88	1.02
5.72	5.68	.704
5.59	5.48	2.007
5.30	5.23	1.338
4.90	4.95	-1.070
4.83	4.79	.835
4.65	4.61	.868
4.42	4.37	1.144
Average % Dev.=1.05		

Set 1012-B

\bar{U}_s	$\bar{U}_{Pit.}$	$\frac{\bar{U}_s - \bar{U}_{Pit.}}{\bar{U}_{Pit.}}$
m/s	m/s	%
6.05	6.06	- .165
6.00	6.01	- .166
5.89	5.88	.170
5.73	5.69	.703
5.36	5.45	-1.650
5.04	5.07	- .592
4.86	4.90	- .816
4.69	4.72	- .636
4.45	4.48	- .670
4.11	4.08	- .735
Average % Dev.= .63		

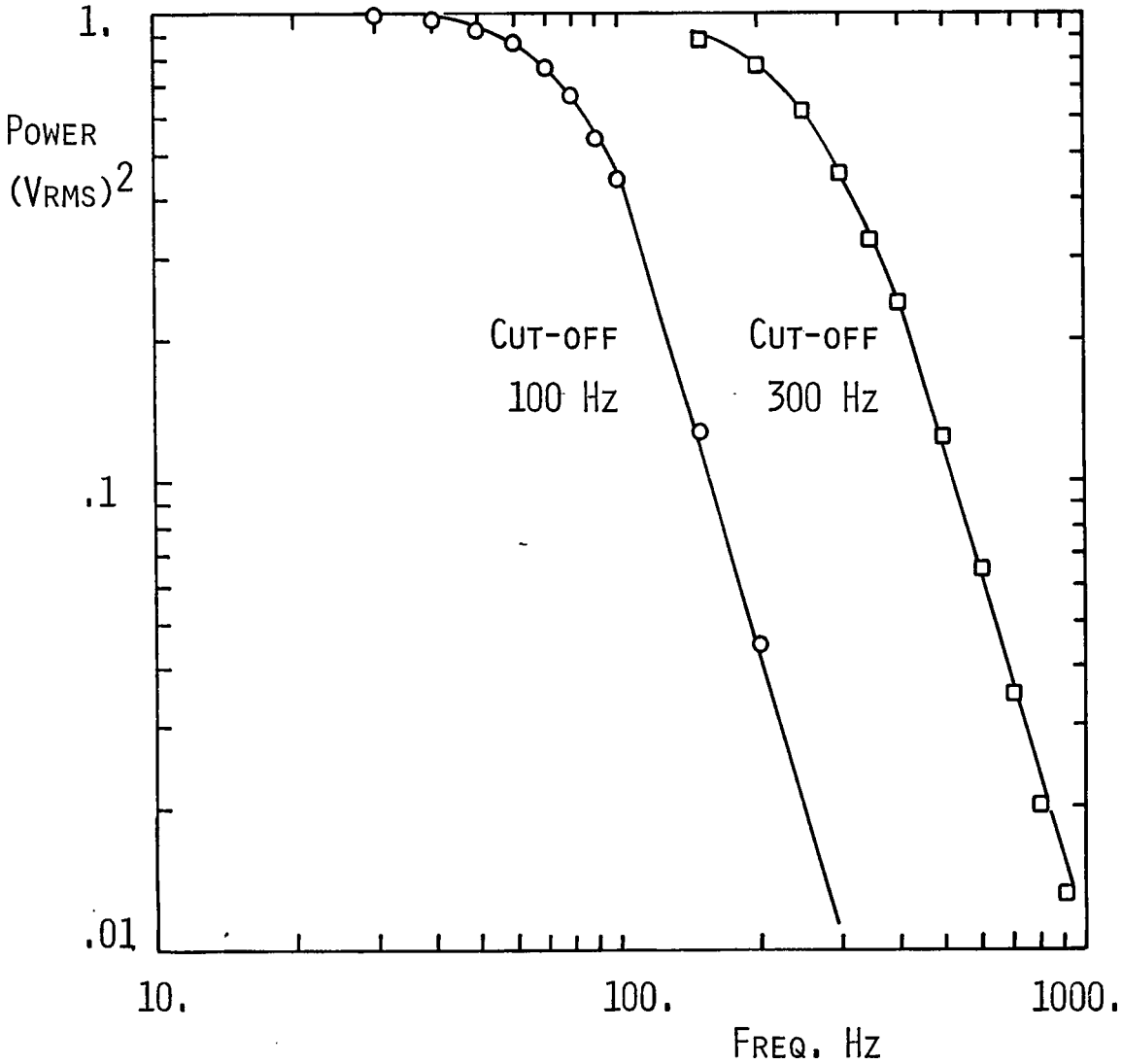
Estimation of the error on mean velocity values measured with an X hot-wire anemometer , using Pitot tube values as a reference . (Continued) .

Set 1016-A

\bar{U}_s	$\bar{U}_{\text{Pit.}}$	$\frac{\bar{U}_s - \bar{U}_{\text{Pit.}}}{\bar{U}_{\text{Pit.}}}$
m/s	m/s	%
2.06	2.05	.488
2.04	2.04	.0
1.99	2.01	-.995
1.95	1.96	-.510
1.88	1.90	-1.053
1.79	1.81	-1.105
1.68	1.71	-1.754
1.59	1.61	-1.242
1.52	1.55	-1.935
1.47	1.48	-.676
1.37	1.41	-2.837
1.27	1.25	1.600

Average % Dev.= 1.18

APPENDIX D



HEWLETT-PACKARD 5489-A
LOW-PASS FILTER PERFORMANCE .

APPENDIX E

COMPUTER PROGRAM INPUT AND CONTROL DATA

Digitizing two signals and writing on tape program .

T SAMPLING PERIOD
N NUMBER OF DATA POINTS = 8192
VI CALIBRATION VOLTAGE
IND INDEX=1
IHW CODE FOR HOT WIRE CALIBRATION
0=NO CALIB 1=CALIB
NCL NUMBER OF RUNS TO BE DIGITIZED
VPITOT VELOCITY MEASURED BY A PITOT TUBE (m/s)
EMINA VOLTAGE USED TO ZERO SUPPRESS SIGNAL A
EMINB VOLTAGE USED TO ZERO SUPPRESS SIGNAL B
RCOLD COLD RESISTANCE
OVHR OVERHEAT RATIO = 1.5
COPR CONSTANT OF PROPORTIONALITY = .0014
TENV TEMPERATURE OF FLUID AT CALIBRATION (°F)
TENVO TEMPERATURE OF FLUID AT RUN (°F)
M NUMBER OF DATA POINTS FOR CURVE FIT
MU DEGREE OF CURVE FIT POLYNOMIAL
NSEQ NUMBER OF SEQUENCE
XSF X SCALE FACTOR
YSF Y SCALE FACTOR
EPS CUT-OFF VALUE FOR CALC.OF MEAN DEVIATION
A1,A2 CALIBRATION CONSTANTS SIGNAL A
B1,B2 CALIBRATION CONSTANTS SIGNAL B

E-2 . PROGRAM FOR AUTO/CROSS SPECTRUM AND CORRELATION

MM NUMBER OF ITERATION FOR SMOOTHING
K NUMBER OF SUBINTERVAL =7
L NUMBER OF SAMPLES/SUBINTERVAL = 2048
NRUNS NUMBER OF RUNS TO BE ANALYZED
DT TIME INTERVAL

NPOC INDEX 1=CROSS 0=AUTO

INDXDT 1=PLOT CORRELATION COEFFICIENT AT
 INCREMENTS OF DT

 0=PLOT CORRELATION COEFFICIENT AT
 INCREMENTS OF 5 DT

NSKIP NUMBER OF SKIP IN READING TAPE

MMT NO.OF ITERATION FOR SMOOTHING IN TAPE

NSM NO.OF ITERATIONS FOR AVERAGING IN
 FREQUENCY DOMAIN = 3

ICRIT -1=AUTO OF FIRST SIGNAL
 0= AUTO OF SECOND SIGNAL
 1=CROSS SPECTRUM AND CORRELATION

NPRIN 0=PRINTOUT AUTO AND CROSS
 1=PRINT CROSS ONLY

APPENDIX F

REPORTED RUNS MAIN PARAMETERS

SET	x m	y m	δ cm	\bar{U}_{\max} m/s	u_{*} m/s
222	10.9	0.	38.0	3.08	- -
307-D	10.9	0.	22.4	3.18	- -
321-A	10.9	0.	33.0	3.21	- -
628	8.5	0.	18.0	6.16	.272
703-B	10.9	0.	30.0	6.04	.176
711-A	10.9	0.	22.5	6.14	.176
711-B	10.9	0.	37.0	5.97	- -
712-A	10.9	0.	22.5	6.19	- -
712-B	10.9	0.	30.0	6.09	.219
712-C	10.9	0.	37.0	6.19	.219
718-A	10.9	0.	22.5	6.28	.231
723-A	10.9	0.	42.0	6.11	.200
723-B	10.9	0.	42.0	6.11	.205
803	10.9	0.	38.0	6.20	- -
804-A	10.9	0.	38.0	6.20	- -
804-B	10.9	0.	38.0	6.08	.159
812-A	8.6	0.	33.0	6.27	.466
814	8.6	0.	33.0	6.35	.472
815-B	8.6	0.	33.3	6.12	.454
819	7.2	0.	31.4	6.06	.384
823-A	8.6	0.	44.5	6.11	- -
1012-A	10.9	0.	17.5	6.02	.235
1012-B	8.5	0.	15.0	6.06	- -
1016-A	10.9	0.	18.0	2.05	.081
1016-B	10.9	0.	12.0	.71	.0527
1018-A	10.9	0.	17.5	6.21	.242
1019-A	10.9	0.	18.0	2.10	.0825
1019-B	10.9	0.	12.0	.58	.0305

Appendix F (Continued)

SET	x m	y m	δ cm	\bar{U}_{max} m/s	u_* m/s
1022-A	10.9	0.	18.0	2.03	.080
1022-B	10.9	0.	12.0	.61	.0321
1024	10.9	0.	12.0	.61	.0350
1120	10.9	0.	17.5	5.25	.206
1121	10.9	0.	17.5	6.12	.241
1125	10.9	0.	17.5	4.45	.194
1127-A	10.9	.95	17.5	6.11	- -
1127-B	10.9	-.95	17.5	6.11	- -
107	9.7	0.	20.0	6.24	- -
108	8.5	0.	17.5	6.21	.277
109	9.7	0.	42.0	6.24	- -
111	9.7	0.	42.0	6.03	.247
112	9.7	0.	42.0	6.02	.247
115	8.5	0.	17.5	6.04	.270
203-A	11.6	0.	40.5	6.06	.274
203-B	11.6	0.	40.5	6.13	- -
204	9.7	0.	35.5	6.11	- -
205-A	9.7	0.	35.5	6.16	- -
205-B	11.6	0.	40.5	6.10	- -
205-C	11.6	0.	40.5	6.01	.271
207	9.7	0.	35.5	6.28	- -
215-A	8.5	-.95	17.5	6.07	- -
215-B	8.5	.95	17.5	6.07	- -
215-C	9.7	.95	42.0	6.13	- -
215-D	9.7	-.95	42.0	6.13	- -
416	9.7	0.	42.0	6.03	.247
427	9.7	0.	42.0	6.03	.247

APPENDIX G
NOMENCLATURE

b	Batchelor's constant (.4)
c_p	Specific heat at constant pressure, cal/g °C
c_v	Specific heat at constant volume
C	Concentration, g/cm ³
C_R	Reference concentration
C'	Dimensionless concentration
D	Molecular mass diffusivity, cm ² /s
E	Internal energy
f	Dimensionless frequency ($n z / \bar{U}$)
Fr	Froude number
$F_{u_i u_j}^{(k)}$	Energy spectrum as a function of wave number
g	Acceleration due to gravity, m/s ²
H	Heat flux, cal/cm ² s
H	Shape factor
i	$\sqrt{-1}$
k	von Karman constant (0.4)
k	Thermal conductivity, cal s ⁻¹ cm ⁻¹ °K ⁻¹
K_x, K_y, K_z	Eddy diffusivity in x , y or z directions
K_M	Momentum eddy diffusivity
K_T	Heat eddy diffusivity
L	Monin-Obukhov length
L_R	Reference length
L_{u_i, r_i}	Integral length scale in r_i direction, cm

M_a	Molecular mass of air
n	Frequency, 1/s
p	Fluctuating pressure, N/m^2
P	Total pressure
\bar{P}	Mean pressure
P_R	Reference pressure
P'	Dimensionless pressure
Pe	Peclet number
Pr	Prandtl number
Q	Heat from a source
$R_{u_i, u_j}(\tau)$	Time correlation coefficient
$R_{u_i, u_j}(\underline{r})$	Space correlation coefficient
R	Gas law constant
Rf	Flux Richardson number
Ri	Richardson number
Re	Reynolds number
Ro	Rossby number
S_E	Eulerian energy spectrum, m^2/s
S_L	Lagrangian energy spectrum
$S_{u_i, u_j}(n)$	Eulerian energy spectrum for velocities u_i, u_j
$S_{ij}(n)$	Rate of strain tensor, 1/s
Sc	Schmidt number
t	time, s
t'	dimensionless time
t_L	Lagrangian integral time scale
T_{u_i, r_i}	Integral time scale in r_i direction

T	Temperature, °C
U_i	Total instantaneous velocity in "i" direction, m/s
\bar{U}_i	Mean velocity in "i" direction
u_i	Eulerian fluctuating velocity in "i" direction
u, v, w	Longitudinal, lateral and vertical fluctuating velocities
\bar{U}	Mean free stream velocity
U_R	Reference velocity
U'	Dimensionless velocity
u_i'	Root mean square velocity in "i" direction
u_*	Friction velocity (τ_o/ρ)
\overline{uw}	Reynolds stresses (turbulence shear stress)
v_i	Fluctuating Lagrangian velocity in "i" direction
\bar{V}	Mean velocity in the y direction
\bar{W}	Mean velocity in the z direction
x_i	Rectangular coordinate in "i" direction, m
x	Rectangular coordinate in longitudinal direction
\bar{X}	Longitudinal average displacement
y	Rectangular coordinate in lateral direction
z	Rectangular coordinate in vertical direction
z_o	Roughness length
\bar{Z}	Vertical average displacement

Greek symbols .-

α	Thermal diffusivity, cm^2/s
β	Lagrangian-Eulerian relationship

δ	Boundary layer thickness, cm
δ_*	Displacement thickness
Δ	Normalized boundary layer thickness
δ_{ij}	Kronecker delta
ε	Roughness height, cm
ε_{ijk}	Alternating tensor
Φ	Viscous dissipation
Φ_ε	Dimensionless viscous dissipation
γ	Specific heats ratio (c_p/c_v)
Γ	Adiabatic lapse rate (1 °C/100 m)
η	Dimensionless height (z / Δ)
Λ	Lapse rate , °C/m
μ	Viscosity, g/cm s
ν	kinematic viscosity, cm ² /s
Ω	Angular velocity
Ω_R	Reference angular velocity
Ω'	Dimensionless angular velocity
Π	Pressure gradient parameter
ρ	density, g/cm ³
ρ_R	Reference density
ρ'	Dimensionless density
Θ	Potential temperature
θ_M	Momentum thickness
θ	Fluctuating potential temperature
τ	Time delay
τ_0	Wall shear stress
χ	Dimensionless length